

ANNI KASIKOV

Evolution and variability of
yellow hypergiant stars



ANNI KASIKOV

Evolution and variability of
yellow hypergiant stars



UNIVERSITY OF TARTU
Press

This study was carried out at Tartu Observatory, University of Tartu, Estonia.

The dissertation was admitted on April 8th, 2026, in partial fulfillment of the requirements for the degree of Doctor of Philosophy (PhD) in Physics (astrophysics), and allowed for defence by the Council of the Institute of Physics, University of Tartu.

Supervisors

Dr Indrek Kolka
Tartu Observatory, University of Tartu
Tõravere, Estonia

Dr Anna Aret
Tartu Observatory, University of Tartu
Tõravere, Estonia

Opponent

Dr Erkki Kankare
Tuorla Observatory, University of Turku
Turku, Finland

The public defence will take place on June 3rd, 2026 at Tartu Observatory, University of Tartu.

Copyright © 2026 by Anni Kasikov

ISSN 1406-0302 (print)
ISBN 978-9908-57-193-5 (print)
ISSN 2806-2132 (pdf)
ISBN 978-9908-57-194-2 (pdf)

University of Tartu Press
<http://www.tyk.ee/>

'In our world,' said Eustace, 'a star is a huge ball of flaming gas.'
'Even in your world, my son, that is not what a star is
but only what it is made of...'

– C. S. Lewis, *The Voyage of the 'Dawn Treader'*

CONTENTS

List of original publications	9
1. Introduction	11
2. Evolution of massive stars	13
2.1. Yellow supergiants	15
2.2. Red supergiants	16
2.2.1. Mass loss in cool stars	16
2.2.2. Observable indicators of atmospheric convection	19
2.2.3. Eruptive mass loss	20
2.2.4. The ‘red supergiant problem’	21
2.3. Yellow hypergiants	22
2.3.1. A little bit of history	22
2.3.2. The single-star post-red-supergiant evolution	23
2.3.3. The ‘yellow evolutionary void’	23
2.3.4. Extreme mass loss eruptions	26
2.3.5. Quiescent variability	27
2.3.6. Circumstellar environments	30
2.4. Binarity among massive stars	31
2.5. Future beyond yellow hypergiant stage	32
2.5.1. Luminous blue variable	32
2.5.2. B[e] supergiant	33
2.5.3. Supernova	34
2.5.4. Failed supernova	35
2.6. Motivation for the thesis	36
3. The family of yellow super- and hypergiants	38
3.1. Sample selection	38
3.2. Distances based on stellar group identification	39
3.3. Kinematic distances from the Galactic H I map	43
3.4. Comparison of distance results	46
3.5. Radius and luminosity	49
3.6. Discussion	52
3.6.1. Spatial distribution	52
3.6.2. Runaway stars	54
3.6.3. Comments on binarity	55
3.7. Summary of results	56

4. V509 Cas – 25 years of stability in the ‘yellow void’	57
4.1. History of variability	57
4.2. Observations and methods	59
4.2.1. Photometry	59
4.2.2. Smoothing photometric observations	61
4.2.3. Spectroscopy	62
4.2.4. Temperature determination	63
4.3. Results	65
4.3.1. $B - V$ colour index	65
4.3.2. Period analysis	65
4.3.3. Effective temperature	66
4.3.4. Radial velocity	68
4.3.5. Disc-like circumstellar structure	71
4.4. Summary of results	74
5. The ‘Great Dimming’ of RW Cep	75
5.1. History and the Great Dimming	75
5.2. Observations and methods	77
5.2.1. Spectroscopic data	77
5.2.2. Spectroscopic measurements	78
5.2.3. Photometry	79
5.3. Results	80
5.3.1. Light curve	80
5.3.2. Following $H\alpha$ through the dimming	82
5.3.3. Radial velocity variability	83
5.3.4. Variability in spectral line profiles	87
5.3.5. Variability in depths of spectral lines	89
5.3.6. The velocity gradient and systemic velocity	90
5.3.7. Emission in resonance lines	92
5.4. Summary of results	95
6. Conclusions	97
References	98
Sisukokkuvõte	114
Acknowledgements	117
Attached original publications	119
Curriculum Vitae	185
Elulookirjeldus	190

LIST OF ORIGINAL PUBLICATIONS

Publications included in the thesis

- I **A. Kasikov**, A. Mehner, I. Kolka, and A. Aret (2026). *Painting a family portrait of the yellow super- and hypergiants in the Milky Way I. Constraining the distances and luminosities*. *Astronomy & Astrophysics* 708, A78.
- II **A. Kasikov**, I. Kolka, A. Aret, T. Eenmäe, and V. Checha (2024). *Yellow hypergiant V509 Cas: Stable in the ‘yellow void’*. *Astronomy & Astrophysics* 686, A270.
- III **A. Kasikov**, I. Kolka, A. Aret, T. Eenmäe, S. P. D. Borthakur, V. Checha, V. Mitrokhina, and S. Yang (2025). *Atmospheric dynamics of the hypergiant RW Cep during the Great Dimming*. *Astronomy & Astrophysics* 694, A153.

Related conference proceedings

A. Kasikov, I. Kolka, and A. Aret (2022). *Following V509 Cas into the Void with FIES*. In proceedings of *NOT – A Telescope For the Future*.

A. Kasikov, A. Mehner, I. Kolka, and A. Aret (2025). *Yellow hypergiants and where to find them*. In proceedings of the IAU Symposium 402: *Massive Stars Across Redshifts in the Era of JWST and Large-Scale Surveys*. Ed. by A. Wofford, N. St-Louis, M. Garcia, and S. Simón-Díaz. Cambridge University Press.

Author’s contribution to the publications

The Author has made considerable contributions to the following original publications. The following list gives details on the author’s work in each of the papers. The Roman numerals correspond to those in the list of publications.

Publication I. The author queried the data from the *Gaia* catalogue, analysed the data, prepared the figures, and wrote the manuscript.

Publication II. The author obtained part of the spectroscopic observations, reduced the spectroscopic data, did the analysis, prepared the figures, and wrote the manuscript.

Publication III. The author obtained part of the spectroscopic observations, reduced most of the spectroscopic data, did the analysis, prepared the figures, and wrote the manuscript.

LIST OF ABBREVIATIONS

Acronyms

AGB	asymptotic giant branch
BH	black hole
BSG	blue supergiant star
CS	circumstellar
ESO	European Southern Observatory
HD limit	Humphreys-Davidson luminosity limit
HR diagram	Hertzsprung-Russell diagram
IMF	initial mass function
LBV	luminous blue variable star
LMC	Large Magellanic Cloud
MS	main sequence
MW	Milky Way
NOT	Nordic Optical Telescope
RSG	red supergiant star
SED	spectral energy distribution
SG	supergiant star
SMC	Small Magellanic Cloud
SN	supernova
TO	Tartu Observatory
YEV	yellow evolutionary void
YHG	yellow hypergiant star
YSG	yellow supergiant star
YSO	young stellar object
ZAMS	zero-age main sequence

Nomenclature

L_{\odot}	Solar luminosity
M_{ZAMS}	Initial mass on the Zero-Age Main Sequence
M_{\odot}	Solar mass
R_{\odot}	Solar radius
T_{eff}	Effective temperature
v_{rad}	Radial velocity

1. INTRODUCTION

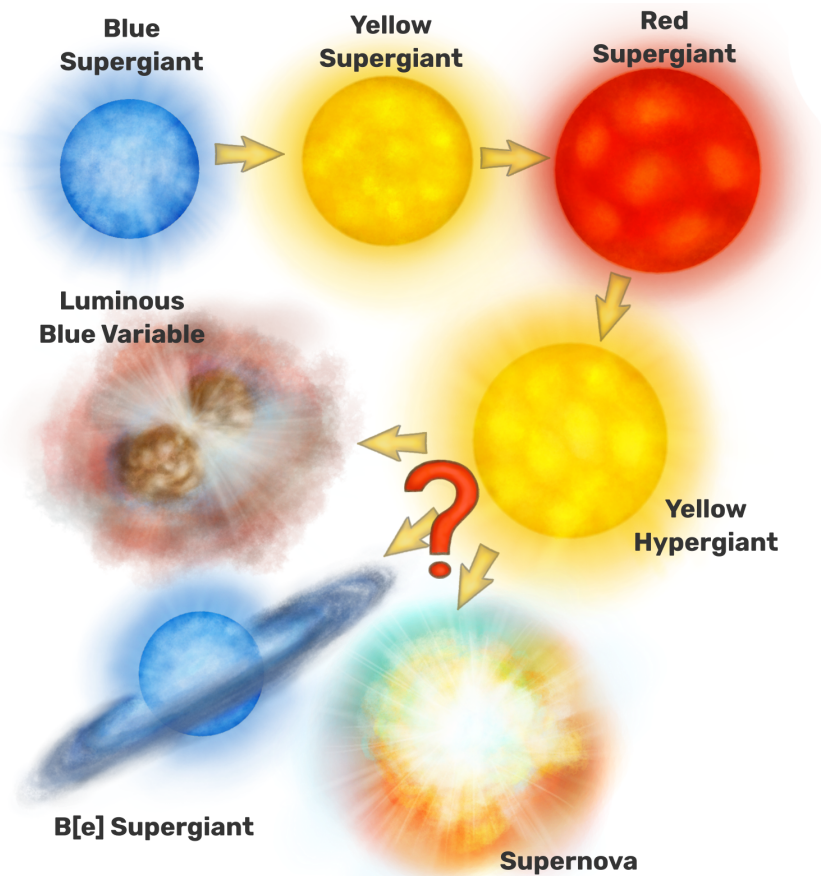


Figure 1.1: Illustration of the post-main-sequence evolution of a single massive star that evolves through the yellow hypergiant phase.

Massive stars are rare, unstable, and short-lived. There are only 2–3 massive stars ($M > 8 M_{\odot}$) per a thousand Sun-like stars. Their lifetimes measure in mere millions of years, while the Sun has lived for billions. Despite their short lifetimes, they leave a strong imprint on their surrounding environments and their home galaxy as a whole. Their winds influence the surrounding interstellar medium by depositing kinetic energy, ionising radiation, and even quenching star formation in nearby regions. Matter ejected from massive stars during and at the end of their lives enriches the environment with heavier elements that affect the chemical evolution of the galaxy.

During their short but turbulent lives, the massive stars go through different evolutionary stages. Some evolutionary changes can happen quickly on cosmic timescales – in tens of thousands of years – but the timescales are still far too

long to be observed in human lifetimes. And thus, we try to piece together the stars' life stories by reading the chemical and physical imprints preserved in stellar atmospheres and their surrounding environments, and comparing stars at different stages of their lives. Reconciling the observations with evolutionary and atmospheric models allows us to connect the different types of massive stars. Further difficulty comes from prevalence of binarity among massive stars – more than 70% are born in binary systems (Sana et al., 2012). Companion interactions and mergers can drastically alter the evolutionary scenarios and open up new possibilities.

Observed stellar populations provide a benchmark for evaluating evolutionary models, and stars in extreme or transitional stages often prove to be the hardest to reproduce. The yellow supergiant (YSG) stars are one of such transitioning stages. A star may become a YSG multiple times in its life – before becoming a red supergiant (RSG), and in some cases, also afterwards on a post-RSG evolutionary path. At that point, the most massive and luminous YSGs are called the yellow hypergiants (YHGs). Two prominent figures in massive star evolution P. Massey and A. Maeder often quote Kippenhahn & Weigert (1990): “[The yellow supergiant] phase is a sort of magnifying glass, also revealing relentlessly the faults of calculations of earlier phases.” Indeed, small changes in the star's mass loss, convective and mixing processes can greatly affect how it evolves. The YSG and YHG phases last only about ten thousand years, a mere 0.1% of the star's lifetime, but their short duration makes understanding these transition phases even more critical to understanding the whole picture of their evolution.

It can be challenging to piece together the life history of a star, but it is even more so to try to predict its future. After passing through the RSG phase, the luminous and unstable YHG continues to lose mass in recurring eruptions. Its future remains unknown. It might continue to evolve to become a luminous blue variable or a B[e]-type hot blue supergiant (e.g. Muñoz-Sanchez et al., 2026). The YHG stage might also be a terminal stage, and the star could explode in a core-collapse supernova (or it might go out without a bang at all; De et al., 2026). Figure 1.1 gives an illustrated look at the past, present, and possible futures of a YHG, as we currently understand it from a single-star evolutionary perspective.

This doctoral thesis aims to bring new observational insights into the YSGs and YHGs in the Milky Way. A study of stellar neighbourhoods of Galactic YHGs and luminous YSGs determines their memberships in clusters and OB associations and provides improved distances and luminosities. Detailed studies showcase two hypergiants at the opposite ends of the YHG evolutionary path. V509 Cas, a well-studied YHG, has entered an atypically stable high-temperature state that may signal future evolution toward the blue supergiant phase. At the other extreme lies RW Cep, a cooler hypergiant that recently underwent a mass-loss outburst, making it an excellent candidate to connect the red and yellow hypergiant evolutionary phases.

2. EVOLUTION OF MASSIVE STARS

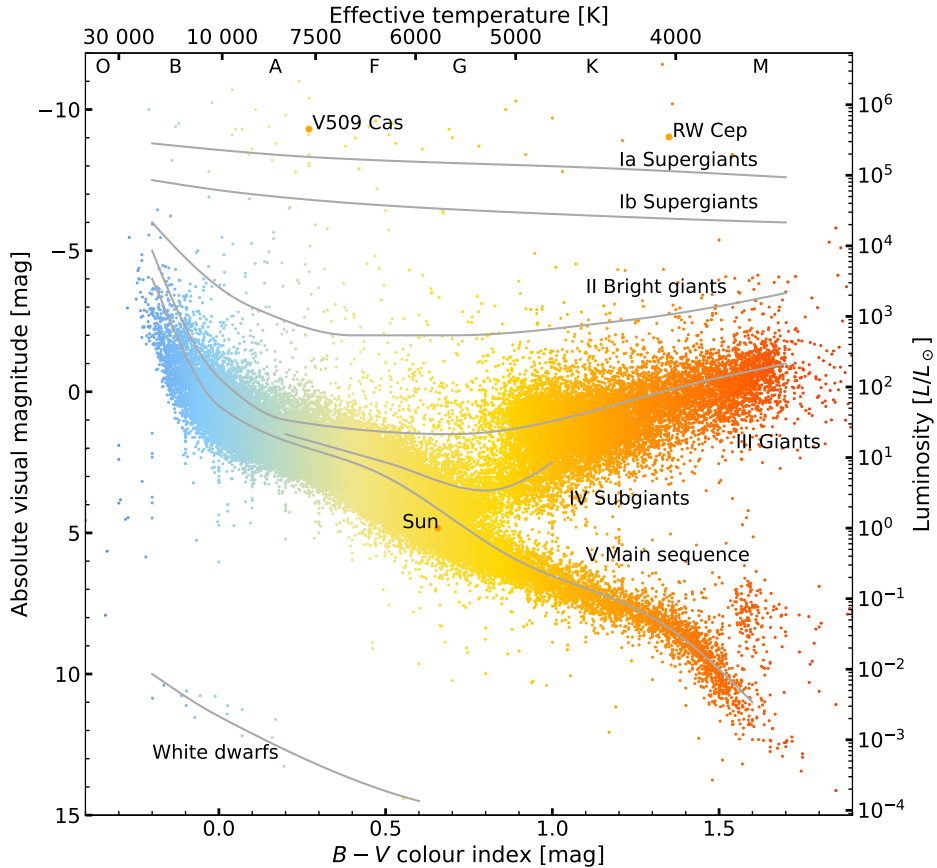


Figure 2.1: The Hertzsprung-Russell diagram. Grey lines mark luminosity classes. The locations of RW Cep and V509 Cas are marked based on Paper I. Data from Anderson & Francis (2012) and Humphreys et al. (2019).

A central goal in the study of massive stars is to understand how they reach the end of their lives. The different stellar evolutionary stages are commonly visualised in the Hertzsprung-Russell (HR) diagram (Fig. 2.1). A young star burning hydrogen in its core is located on the main sequence (MS). As it evolves, its internal structure and surface properties change, and its position on the HR diagram shifts accordingly. High-mass stars begin their lives as O-type main-sequence stars at the very top of the HR diagram, characterised by high luminosities ($\log(L/L_{\odot}) > 4.7$) and effective temperatures ($T_{\text{eff}} > 30\,000$ K). Stellar evolutionary models follow a star's progression through the increasingly advanced stages of evolution up until the star's final moments before a supernova (SN) explosion.

A star's evolutionary path is determined primarily by its initial mass M_{ZAMS} on the zero-age main sequence (ZAMS) in the HR diagram. Conti (1975) proposed a

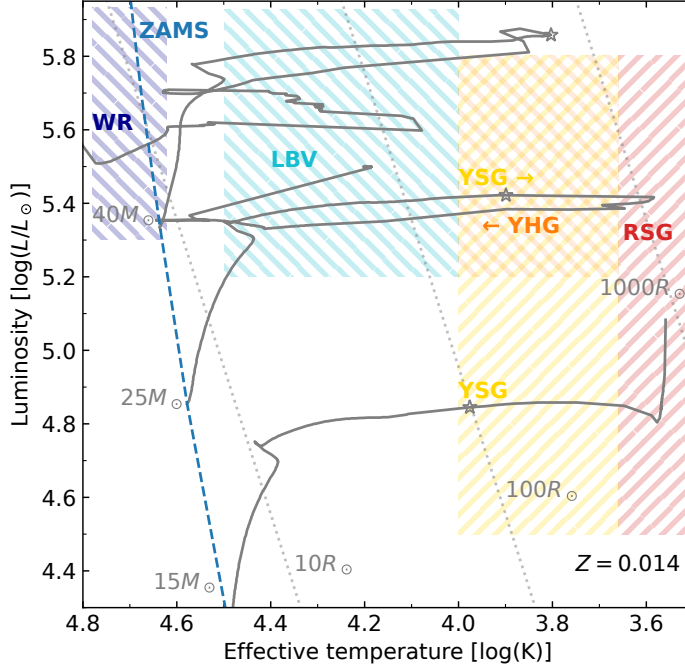


Figure 2.2: HR diagram depicting evolutionary tracks of massive stars. The approximate areas where different types of stars are located are marked with dashed blocks in different colours: WR – Wolf-Rayet, LBV – luminous blue variable, YHG – yellow hypergiant, YSG – yellow supergiant, RSG – red supergiant. ZAMS is marked with a blue dashed line at the origin points of the tracks. The star symbol on the track marks helium ignition in the core. The grey diagonal dotted lines represent lines of constant radius. The tracks are from Ekström et al. (2012) at solar metallicity considering stellar rotation.

sequence of different evolutionary stages connecting luminous O-type stars with evolved Wolf-Rayet stars. Chiosi & Maeder (1986) extended the scheme further, and it became known as the Conti scenario. A slightly updated version from Ekström & Georgy (2025) is as follows:

- $M \gtrsim 60 M_{\odot}$: O \rightarrow Of/WNL \rightarrow LBV \rightarrow WNL \rightarrow WC \rightarrow WO
- $M \simeq 40 - 60 M_{\odot}$: O \rightarrow BSG \rightarrow LBV \rightarrow WNL \rightarrow (WNE) \rightarrow WC \rightarrow (WO)
- $M \simeq 30 - 40 M_{\odot}$: O \rightarrow BSG \rightarrow RSG \rightarrow WNE \rightarrow WCE
- $M \simeq 25 - 30 M_{\odot}$: O \rightarrow (BSG) \rightarrow RSG \rightarrow (YHG? LBV?)
- $M \simeq 10 - 25 M_{\odot}$: O/B \rightarrow RSG \rightarrow (Cepheid loop for $M \lesssim 15 M_{\odot}$) \rightarrow RSG

The abbreviations are: BSG – blue supergiant, LBV – luminous blue variable, RSG – red supergiant, YHG – yellow hypergiant, and WNL/WNE/WCE/WC/WO are nitrogen/carbon/oxygen rich Wolf-Rayet stars in progressively advanced stages of envelope stripping and nuclear processing.

A massive star on the ZAMS with mass $M_{\text{ZAMS}} \lesssim 25 M_{\odot}$ evolves across the HR diagram and ends its life as a RSG (Fig. 2.2). A star with $25 M_{\odot} \lesssim M_{\text{ZAMS}} \lesssim 40 M_{\odot}$

evolves to a RSG, but loses enough mass to bring about further evolution back to the blue, transition through the YHG stage and become an evolved blue supergiant. Stars with $M_{\text{ZAMS}} \gtrsim 40 M_{\odot}$ never evolve to become RSGs and evolve through different hot supergiant stages. The mass ranges for different evolutionary sequences depend strongly on model assumptions – mixing in the core, stellar rotation, metallicity, and mass loss. Additionally, significantly different evolutionary scenarios can arise from interactions in multiple star systems. In the context of this work, we focus on the single-star evolution of massive stars with $20 M_{\odot} < M_{\text{ZAMS}} < 40 M_{\odot}$, as this is the mass range expected for YHG progenitors in Geneva evolutionary models (Ekström et al., 2012).

An O-type star on the MS with a mass of $20 M_{\odot} < M_{\text{ZAMS}} < 40 M_{\odot}$ and a radius of around $10 R_{\odot}$ burns hydrogen in the core for approximately 5–10 Myr. The timescale is dependent on model assumptions of the star’s rotation and convective processes. Increasing the convective or rotational mixing can bring more hydrogen fuel to the core and extend the main sequence lifetime. When hydrogen is exhausted in the core, it contracts and the star’s envelope expands (also known as the mirror effect). The star leaves the main sequence, sustained by the hydrogen-burning shell surrounding the previously hydrogen-burning core. Its envelope continues to expand, and its surface temperature decreases as it evolves across the HR diagram and becomes a yellow supergiant (Ekström et al., 2012; Ekström & Georgy, 2025).

2.1. Yellow supergiants

Stars with $M_{\text{ZAMS}} > 20 M_{\odot}$ cross the HR diagram very quickly, within few tens of thousands of years (Meynet et al., 2015). Thus, the YSGs represent a very short period in post-MS evolution. The timescale depends on the properties of the hydrogen burning shell: efficiency of convection, temperature, metallicity, and chemical gradient. The star’s crossing is slowed if the hydrogen shell is strong: there is a deep and active intermediate convective zone, the temperature is high, and it generates large amounts of energy (Ekström & Georgy, 2025).

Core contraction during the post-MS evolution leads to increase in core temperature. When it reaches $\sim 10^8$ K, helium starts burning in the core (marked with a star in Fig. 2.2). For stars with $M_{\text{ZAMS}} > 12 M_{\odot}$, helium ignites already before star becomes a RSG. Thus, YSGs are helium-burning stars (Ekström & Georgy, 2025).

The YSGs are very rare due to the short duration of the phase. Determining the YSG content in a galaxy can help improve the stellar evolution models and constrain the initial mass function (IMF). Drout et al. (2012) and Neugent et al. (2012) conducted studies of YSGs in the Magellanic Clouds and M33. They found that the Geneva evolutionary models (Ekström et al., 2012) characterise well the relative number and expected lifetimes of YSGs in these galaxies. The Ekström et al. (2012) models predict the duration of the YSG stage between 30 000 and 80 000 years for stars with M_{ZAMS} between $20 M_{\odot}$ and $40 M_{\odot}$. Based on the ratio of YSGs and OB-type massive stars in the LMC, Neugent et al. (2012) estimated a

duration of $\sim 17\,000$ yr. However, a previous study with a similar comparison in M31 (Drout et al., 2009) estimated the YSG phase to last only for ~ 3000 years.

There are few studies on the variability of YSGs. The stars display small-amplitude stochastic variations (~ 0.1 mag) in their light curves, any may have variable H α emission (Dorn-Wallenstein et al., 2019; Kourniotis et al., 2017). The variability may be due to (radial or non-radial) pulsations (Kienzle et al., 1998; Lovy et al., 1984), the mechanisms are described in Sect. 2.3.5.

2.2. Red supergiants

Following the crossing of the HR diagram, the star spends the next few hundred thousand years of its life as a red supergiant. Here, its further evolution is determined by how much and how quickly the star loses mass. The precise mechanisms for RSG mass loss through the combination of winds, pulsations, convection, or eruptions are still debated.

The mass-loss rate determines the time spent as a RSG and whether the star has a future as a post-red supergiant or ends its life in a supernova (SN) explosion (Georgy, 2012; Meynet et al., 2015). Increased mass-loss rate reduces the time a star spends as a RSG. Based on the non-rotating Geneva evolutionary model, a $20M_{\odot}$ star with the model standard mass-loss rate spends ~ 0.55 Myr as a RSG, but increasing the rate by a factor of 10 reduces that time to ~ 0.18 Myr (Meynet et al., 2015).

2.2.1. Mass loss in cool stars

In hot stars, the main driver of mass loss is the line-driven stellar wind (radiation pressure on spectral lines), but this process is not efficient in the cool SG atmospheres. Unlike the hot stars, the mass-loss of RSGs does not seem to depend on metallicity (Antoniadis et al., 2024; Kee et al., 2021). The mechanisms of mass loss in cool SGs (including both yellow and red supergiants) are not fully established and a number of different theories have been proposed (overview by Levesque, 2017, and references therein):

- *Dust-driven winds.* For RSGs and the asymptotic giant branch (AGB) stars, the model of dust-driven winds is the most commonly used mechanism. In this model, the dust condenses in a thin shell close to the star, causing the photons emitted by the star to scatter and transfer part of their momentum to the dust.
- *Pulsations.* Radial pulsations may trigger dust-driven winds through expansion and contraction, and also induce shock waves and eject matter from the outer layers of the star.
- *Convective motions.* Convective motions may produce turbulent pressure that decreases effective gravity and facilitates mass loss.

- *Molecular-line-driven winds.* An analogous theory to the line-driven winds in hot stars has been proposed. Winds are driven by radiation pressure on molecular lines, instead of atomic ones.
- *Magnetic fields.* Alfvén waves caused by perturbations in the magnetic field could transfer momentum to circumstellar gas and accelerate the wind.

Each of these theories has caveats: the pulsations drive mass loss in Mira-type AGB stars, but may not be strong enough in RSGs; the condensed dust appears to be too far from the stellar surface for efficient winds; other processes may not be efficient enough in RSGs to explain the observed mass-loss rates. Fig. 2.3 gives an illustrative overview of the different processes.

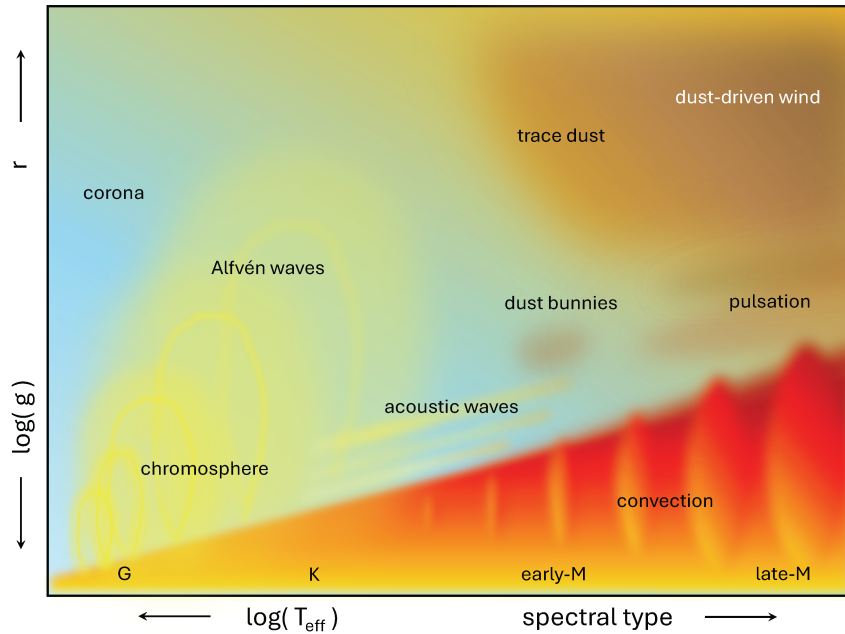


Figure 2.3: Illustration of different drivers of mass loss in RSGs. K and early-M type stars also have chromospheres, but it has been separated from the dust for clarity. Figure adapted from van Loon (2025).

In evolutionary models, the mass loss in cool stars ($T_{\text{eff}} < 10$ kK) is described using observation-based empirical prescriptions. The first such relation between the mass-loss rate and stellar parameters was proposed by Reimers (1975):

$$\dot{M} = 5.5 \times 10^{-13} LR/M,$$

where luminosity L , radius R , mass M are in solar units.

A commonly used mass-loss prescription for cool stars was published by de Jager et al. (1988). It defines mass-loss rate as a function of effective temperature T_{eff} and luminosity L . It is an empirical fit to mass-loss rates of 274 stars covering spectral and luminosity classes from dwarfs to supergiants without considering the type of mass-loss driving mechanism. The mass loss increases with increasing L and decreases with increasing T_{eff} . Linearised de Jager et al. (1988) mass-loss

estimates are plotted in Fig. 2.4. An important result of the analysis of de Jager et al. (1988) is determination of an area of instability on the HR diagram near the Humphreys-Davidson (HD) luminosity limit (Humphreys & Davidson, 1979) in a broad range near $T_{\text{eff}} \approx 10000$ K and $\log(L/L_{\odot}) = 6$. The implications of this region are discussed in Sect. 2.3.3. In recent years, many more empirical mass-loss prescriptions have been published.

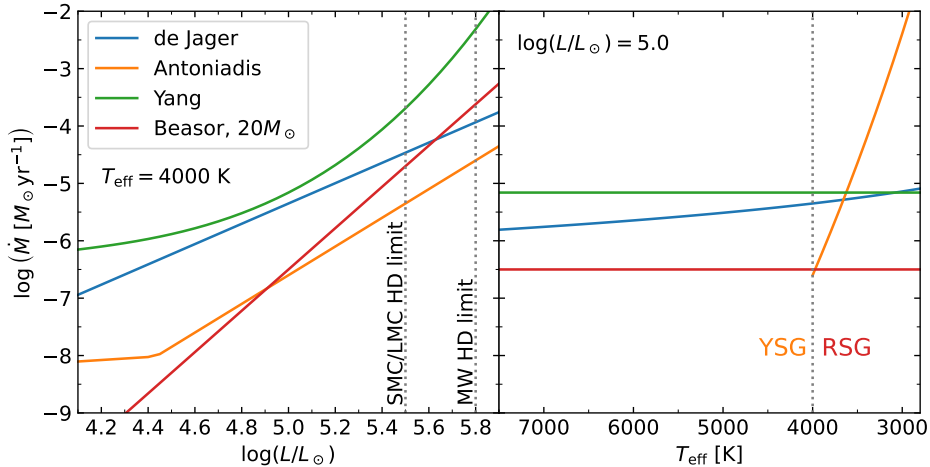


Figure 2.4: Comparison of mass-loss prescriptions from Antoniadis et al. (2024), Beasor et al. (2020), de Jager et al. (1988), and Yang et al. (2023). On the left panel T_{eff} is fixed at 4000 K, HD luminosity limits in the Milky Way (Humphreys & Davidson, 1979) and SMC/LMC (Davies et al., 2018) are marked with dotted lines. On the right panel, luminosity is fixed at $\log(L/L_{\odot}) = 5.0$. Yang et al. (2023) and Beasor et al. (2020) prescriptions are not dependent on T_{eff} , but Beasor et al. (2020) is dependent on M_{ZAMS} , which is set to $20M_{\odot}$.

Several mass-loss studies have been done for RSGs in the Magellanic Clouds. Yang et al. (2023) and Antoniadis et al. (2024) used samples of over 2000 RSGs to study their mass loss through stellar winds. They both found enhanced mass loss for RSGs with luminosities above $\log(L/L_{\odot}) \approx 4.4 - 4.6$, but depending on model assumptions, the mass-loss rates vary by 2–3 orders of magnitude. Other studies estimate much lower mass-loss rates. Beasor et al. (2020, 2023) studied the mass loss of RSGs in Galactic open clusters. They predict that through stellar winds, a RSG can lose a maximum of $\sim 1 M_{\odot}$ of mass, which is not enough to strip the star and trigger blueward evolution. For example, the Geneva stellar evolution models predict mass-loss rate during the RSG phase greater by a factor of 20 compared to the results of Beasor et al. (2020) – a total mass lost for a $M_{\text{ZAMS}} = 20 M_{\odot}$ star would be $\sim 9 M_{\odot}$ in Geneva models compared to $0.79 M_{\odot}$ found by Beasor et al. (2020).

So far, the only analytical prescription for RSG mass loss was published by Kee et al. (2021). Their model uses turbulent pressure for mass ejection (triggered by hydrogen recombination in the convective cells, see Sect. 2.2.2). They found

increased mass-loss at higher luminosities, making it possible for the most luminous RSGs to evolve blueward. Thus, the selection of a RSG mass-loss prescription has important implications for the post-RSG evolutionary pathways.

There is no mass-loss prescription specifically for YSGs and YHG, except for the one provided by de Jager et al. (1988) for the entire HR Diagram. Thus, for calculating mass loss in stellar evolutionary models either a RSG prescription can be extrapolated to higher temperatures, or a combination of de Jager et al. (1988) and one of the RSG mass loss prescriptions can be used.

2.2.2. Observable indicators of atmospheric convection

The structure of RSGs is shaped by convection. The outer convection zone reaches into 99% of the stellar radius and includes 60-70% of the star's total mass (Ekström & Georgy, 2025). The convective motion creates deep mixing within the star and dredges up products of the CNO cycle, enriching the surface with nitrogen and depleting carbon and oxygen (Davies et al., 2009; Iben, 1964). However, the vast atmosphere of a RSG contains only around a dozen of giant convective cells (Josselin & Plez, 2007; Schwarzschild, 1975).

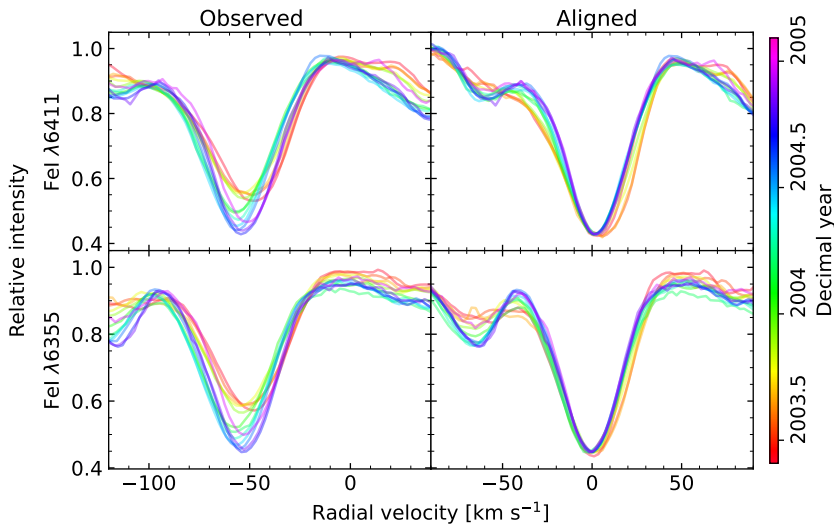


Figure 2.5: Spectral line variability as a result of the movement of giant convective cells in RW Cep. Left: observed spectral line profiles of two Fe I lines over two years; right: same profiles shifted and scaled together. The velocity variation in the spectral lines reflects the rise of the giant cells to the surface of the star. Spectra are from the ELODIE spectrograph, observations described in Sect. 5.2.

Interferometry of surfaces of RSGs reveals a large-scale structure of convection cells as well as smaller-scale granules (e.g. Montargès et al., 2017; Norris et al., 2021). The larger features vary on timescales of several years, while the small-scale features change on timescales of a few months (Kravchenko et al., 2019; Norris et al., 2021). In spectral lines, the movement of large-scale convective cells

results in varying intensity and radial velocity, while keeping the general shape of the line profile (Fig. 2.5; Gray, 2021). The mean T_{eff} of the stellar surface varies in conjunction with the star’s visible magnitude due to the movement of the cells. However, the photometric and T_{eff} variability follow the radial velocity with a phase lag of few tens of days. The phase lag could be due to the turnover of material in the stellar atmosphere, where the rising plume creates brighter and hotter areas on the stellar surface (Gray, 2008) or due to acoustic waves originating from the disturbances in the convective flow propagating through the photosphere (Kravchenko et al., 2019). Additionally, atmospheric tomography of RSGs Betelgeuse and μ Cep revealed a velocity gradient in spectral lines formed at different optical depths (Kravchenko et al., 2019, 2021). In Paper III, we observed a similar velocity gradient in the atmosphere of RW Cep, the results are detailed in Chapter 5.

2.2.3. Eruptive mass loss

Eruptive episodes in RSGs received wider attention from the public and scientific community during the ‘Great Dimming’ of Betelgeuse in 2019 and early 2020. The media reports of an imminent SN explosion were greatly exaggerated. The leading explanation to the rapid decline in brightness became the condensation of ejected matter into a dusty shell shielding the starlight (Montargès et al., 2021). Since then, such mass-loss eruptions have been observed in several Galactic and extragalactic luminous RSGs: RW Cep (Anugu et al., 2023, 2024b; Paper III), in the historic light curve of VY Cma (Humphreys et al., 2021), in [W60] B90 in the LMC (Munoz-Sanchez et al., 2024), and in M51 galaxy RSG M51-DS1 (Jencson et al., 2022).

Based on numerous multi-wavelength observations of the Betelgeuse event, the trigger for dimming events seems to be a combination of convective motions and shocks propagating through the photosphere (Dupree & Montargès, 2025, and references therein). A hot plume rising through the interior of the star breaks out of the photosphere in a surface mass ejection event, which affects the whole stellar surface (López Ariste et al., 2023) and causes temporary change in the pulsation period of the star (MacLeod et al., 2025). Indication of gaseous outflows during the dimming of RW Cep was given by the blue-shifted $H\alpha$ emission (Paper III). The cooling of the photosphere by a few hundred degrees and the condensation of ejected matter into dust cause the decrease in brightness (Montargès et al., 2021). The formation and time evolution of a fainter region on the surface of a star was observed with interferometry both for Betelgeuse (Montargès et al., 2021) and for RW Cep (Anugu et al., 2023, 2024b), reinforcing the dust cloud hypothesis.

The dust cloud in front of the star can reduce its visual brightness by 1–2 mag, and variability also appears in the mid-infrared light curve at a smaller scale (Munoz-Sanchez et al., 2024) and at sub-millimeter wavelengths (Dharmawardena et al., 2020). The dimming of starlight during such mass-loss eruptions can last

from a few hundred days to several years, the duration can depend on the size of the star or the size, geometry, and opacity of the dust clump (Anugu et al., 2024b; Humphreys et al., 2021). Such events may reoccur on timescales of decades, and may be common in RSGs (Anugu et al., 2024b; Munoz-Sanchez et al., 2024). Indeed, in the case of VY CMa, traces of mass loss eruption events reach back a thousand years (Humphreys et al., 2021; Smith et al., 2001). Such localised eruptive events create an asymmetric nebula with filaments and arc-like structures around the star (Smith et al., 2001). It remains unclear, how significant the contribution of such events is to the total amount of mass lost during the RSG stage, or how many such events have remained undetected due to the ejected dust cloud not aligning with our line of sight.

The Geneva evolutionary models (Ekström et al., 2012) simulate enhanced mass loss for stars more massive than $M_{ZAMS} = 15 M_{\odot}$. When the star evolves through the RSG stage, in the outer layers of the stellar envelope the luminosity may locally exceed Eddington luminosity $L_{Edd} = 4\pi cGM/\kappa$ (where κ is the opacity) due to the increase in opacity from variation in hydrogen ionisation levels. In such cases, the mass-loss rate of the star is tripled to simulate ‘enhanced’ mass loss during this instability. When such supra-Eddington layer disappears, normal mass-loss rate is restored. With the Geneva code mass-loss estimates, rotating stars with M_{ZAMS} between $20M_{\odot}$ and $32M_{\odot}$ lose a large amount of mass as RSGs, enabling them to evolve back towards hotter temperatures on a post-RSG evolutionary track. A similar process of Eddington-limit induced mass loss has been successfully used in the stellar evolution code MESA to reproduce the observed populations of cool evolved massive stars in the Magellanic Clouds (Pauli et al., 2026). Thus, the expected effects of enhanced mass loss are approximated by temporarily increasing the mass-loss rate defined by an empirical prescription by a pre-defined factor. The single-star post-RSG evolutionary pathway remains an open prospect. Zapartas et al. (2025) compared different mass-loss prescriptions for RSGs and found that depending on the prescription chosen, the expected ratio of YHG to YSG varies between <1% (Beasor et al., 2020) and 23% (Kee et al., 2021).

2.2.4. The ‘red supergiant problem’

Majority of single massive stars end their lives as RSGs exploding in type II-P supernovae – core-collapse SNe from stars with extensive hydrogen envelopes. A statistical analysis type II-P SN progenitors revealed that they have initial masses in the range $8.5 M_{\odot} \lesssim M \lesssim 18 M_{\odot}$ with an upper luminosity limit of $\log(L_{bol}/L_{\odot}) \simeq 5.1$ (Smartt et al., 2009). However, the most massive RSGs in the Local Group have initial masses of around $25 M_{\odot}$, corresponding to a much higher luminosity of $\log L/L_{\odot} \simeq 5.5$ (Davies & Beasor, 2018). This mass discrepancy in lack of high-mass SN progenitors became known as the ‘red supergiant problem’ (Smartt et al., 2009). Other independent studies have found similar upper progenitor mass limits (e.g. Dwarkadas, 2014; Fang et al., 2025; Rodríguez, 2022), but the

statistical significance of this result has been questioned, and the progenitor masses might be systematically underestimated due to model assumptions, measurement uncertainties, or circumstellar extinction (Beasor et al., 2025; Davies & Beasor, 2018; Walmswell & Eldridge, 2012).

Various physical explanations to the RSG problem have been proposed. Core-collapse simulations reveal that RSGs above $M \gtrsim 20M_{\odot}$ do not produce SN explosions, but rather collapse directly into black holes (BHs; Smartt, 2015, and references therein). However, so far very few candidates have been identified (see Sect. 2.5.4). In the context of YHGs, perhaps the most relevant and attractive theory is explaining the RSG problem through post-RSG evolution. Stellar evolution models predict post-RSG blueward evolutionary tracks for stars with $M_{\text{ZAMS}} \gtrsim 20 M_{\odot}$ (Ekström et al., 2012; Zapartas et al., 2025). Thus, at the end of their lives the higher mass stars would explode as different types of SNe, explaining the ‘missing’ luminous type II-P SN progenitors.

2.3. Yellow hypergiants

The number of confirmed YHGs in the Milky Way is around 10, with a few more promising candidates (e.g. Clark et al., 2014; Kourniotis et al., 2025). The first confirmed extragalactic YHG was Var A in M33 thanks to the direct observations of the star’s 50-year-long mass-loss episode (Humphreys et al., 1987). Since then, a few more candidates have been identified in M33 (Kourniotis et al., 2017) and in the LMC (Dorn-Wallenstein et al., 2025; Kourniotis et al., 2022).

2.3.1. A little bit of history

In the 1950s, five extremely luminous ‘super-supergiants’ were observed in the Magellanic Clouds with spectral classes between F8 and G5 and all of them associated with nebulae (Feast & Thackeray, 1956). Seven stars with similar luminosities and evidence of atmospheric instabilities were also known in the Milky Way (de Jager, 1980): ρ Cas, HR 4773 (=HD 96918), HR 8752 (=V509 Cas), HR 5171, HD 160529, ζ^1 Sco, and HD 80077, first four of them yellow with spectral classes F8–G8 and the last three bluer B1–A2 stars.

In 1971, Keenan specified the term ‘super-supergiants’ to refer to stars of the highest luminosity class of 0 with extended atmospheres, relatively high mass-loss rate and showing one or more broad emission components in $H\alpha$. A few years later, a criterion of broad absorption lines was added as an indicator of large-scale motions in the atmosphere (de Jager, 1998). In 1980, de Jager coined the term ‘hypergiants’ in his book *The Brightest Stars*, replacing the rather clunky ‘super-super’ prefix. These stars were designated the Ia0 or Ia+ luminosity class. Most of the hypergiant stars are yellow hypergiants, though some blue (e.g. three of them listed above) and red hypergiants also exist. One of the red hypergiants, RW Cep, is the subject of Chapter 5.

In 1998, de Jager suggested that ‘yellow hypergiants’ are a post-RSG evolutionary state. Various criteria have been proposed to identify post-RSG supergiants. Including, but not limited to: abundance anomalies and Na excess due to dredge-up of nuclear reaction products (Boyarchuk et al., 1988b; Takeda & Takada-Hidai, 1994), lower mass due to the advanced evolutionary state (de Jager, 1998), dusty and gaseous envelopes ejected following the RSG phase (Kastner & Weintraub, 1995), $^{12}\text{C}/^{13}\text{C}$ ratio below 5–10 indicating ^{13}C enrichment (Oksala et al., 2013), or pulsation periods shorter than 1 day (Dorn-Wallenstein et al., 2020). Following these criteria, different stars have been included or excluded from the list of YHG candidates. At its core, the group includes stars in an advanced post-RSG evolutionary stage with unstable atmospheres and eruptive mass-loss episodes.

2.3.2. The single-star post-red-supergiant evolution

In a single-star evolutionary scenario, if a RSG loses enough mass to significantly reduce its hydrogen envelope, it moves onto on a blueward evolutionary track. Thus, such an evolutionary track is very sensitive to the mass-loss estimates of RSGs. The evolution to the blue begins when the star has lost between 40% and 60% of its initial mass in the RSG stage, and the mass fraction of the He core comprises 60–70% of the total mass of the star (Meynet et al., 2015).

The duration of the YHG phase also strongly depends on model assumptions. Using the Geneva evolutionary models, Meynet et al. (2015) determined that depending on the mass loss rate, the second crossing of the HR diagram as a YHG would last between 30 000 and 300 000 years. Interestingly, their YHG phase has a longer duration than the YSG phase, implying that most yellow massive stars are post-RSGs. Stothers & Chin (1996) proposed a dynamic instability for massive stars ($\sim 35 M_{\odot}$ in their models) in the final stage of their RSG phase, causing very rapid transition ~ 1000 yrs across the HR diagram to the blue. Nieuwenhuijzen et al. (2012) expect the YHG stage to last around 10 000 yr, or slightly more.

2.3.3. The ‘yellow evolutionary void’

On the HR diagram, a luminous blueward evolving star encounters an area of enhanced atmospheric instability that has become known as the ‘yellow evolutionary void’ (YEV) due to the relative lack of stars in this region (de Jager & Nieuwenhuijzen, 1997; Nieuwenhuijzen & de Jager, 1995). This area of instability affects stars with luminosities around $\log(L/L_{\odot}) \gtrsim 5.6$ and $T_{\text{eff}} \simeq 8300\text{--}10\,000$ K (Fig. 2.6; Nieuwenhuijzen & de Jager, 1995). The area of the region depends on the evolutionary models used and underlying assumptions. The border of the YEV has also been called the ‘white wall’ (Oudmaijer & Wit, 2013). Stothers & Chin (2001) connected the YEV to the low-luminosity end of the luminous blue variable (LBV) instability region, set the lower temperature limit to ~ 7000 K, and suggested that after mass loss in the YHG phase, the stars can pass through the YEV and appear on the other side among the LBVs.

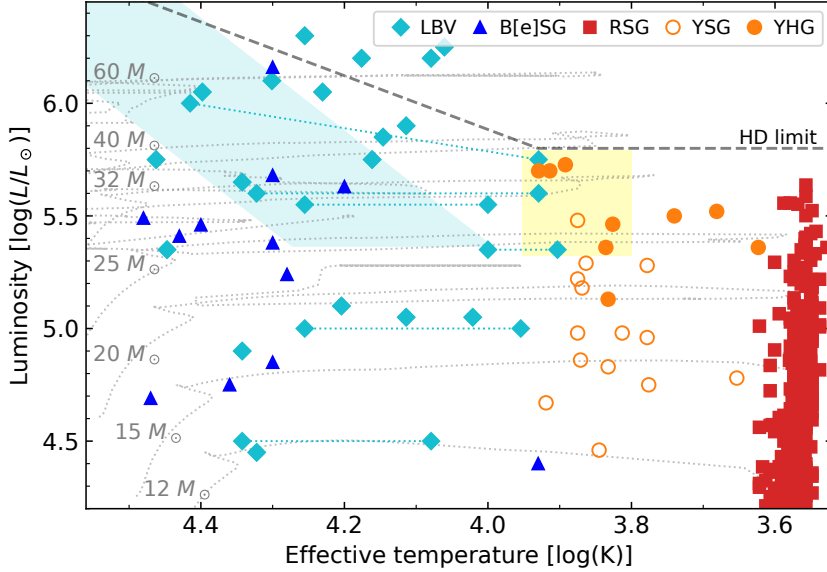


Figure 2.6: The upper HR diagram of the Milky Way. Different colours and symbols mark different types of evolved massive stars. Dashed line marks the Humphreys-Davidson (HD) luminosity limit (Humphreys & Davidson, 1979). Evolutionary tracks for stars with different M_{ZAMS} are drawn at solar metallicity (grey dotted lines; Ekström et al., 2012). Two instability regions are marked: YEV (yellow; Nieuwenhuijzen et al., 2012) and LBV instability strip (blue; Humphreys & Davidson, 1994). Literature data for Galactic RSGs (red squares; Healy et al. 2024), LBVs (cyan diamonds; Smith et al. 2019), and B[e] supergiant stars (blue triangles; Miroshnichenko et al. 2025) are shown for comparison. Figure adapted from Paper I.

A number of YHGs are seen clustering at the low-temperature side of the YEV, which suggests an evolutionary explanation for their observed instabilities (Nieuwenhuijzen & de Jager, 1995). These stars include: IRC +10420 (Koumpia et al., 2022; Oudmaijer & Wit, 2013), V509 Cas (Nieuwenhuijzen et al., 2012; Paper II), IRAS 17163-3907 (Koumpia et al., 2020). No stars have been observed to pass through it on a post-RSG evolutionary track, though LBVs occasionally enter the YEV region during their eruptive outburst episodes.

The occurrence of the YEV has been explained through a number of instability properties in the atmospheres of YHGs (listed here as in de Jager, 1998).

1. When calculating the values of effective gravity (g_{eff}) across the upper HR diagram, Nieuwenhuijzen & de Jager (1995) found that for blueward evolving stars in the YEV region their models did not converge and $g_{\text{eff}} < 0.1 \text{ cm s}^{-2}$. The small $g_{\text{eff}} \simeq 0$ values indicate that the atmosphere becomes detached from the star's gravitational attraction.

2. In parts of the upper photosphere, negative density gradient occurs due to the increasing ionisation of hydrogen with increasing temperature from 7000 K to about 13 000 K (de Jager & Nieuwenhuijzen, 1997).

3. Inside the YEV, the sonic point is located within the star’s atmosphere, causing the stellar wind to achieve near-supersonic velocity. This contributes to periods of enhanced mass loss during the pulsational cycle (Nieuwenhuijzen & de Jager, 1995). Lobel et al. (1998) offered two scenarios explaining the variable wind: the wind velocity is affected by the variable T_{eff} and opacity during the stellar pulsations, and the wind is accelerated at higher T_{eff} values; alternatively, the atmospheric pulsations may transfer momentum at the base of the wind, thereby causing variable wind velocities and mass-loss rate through mechanical means.

4. Inside the YEV, the first adiabatic exponent Γ_1 decreases below $\frac{4}{3}$ (Lobel et al., 1992). This property has been debated in the literature and warrants a longer explanation.

Γ_1 is connected to dynamic instabilities in the stellar atmosphere (Eq. 2.1). For monatomic gas, $\Gamma_1 = \frac{5}{3}$ and for photon gas $\Gamma_1 = \frac{4}{3}$. The value of Γ_1 is sensitive to ionisation of hydrogen, and in ionisation zones its value may decrease, $\Gamma_1 < \frac{4}{3}$. There is overlap in the areas of the YEV and the region on the HR diagram, where $\Gamma_1 < \frac{4}{3}$ (de Jager & Nieuwenhuijzen, 1997). Lobel (2001) noted, that by itself, the low values of Γ_1 do not cause dynamical instabilities, but combined with pulsations and strong convective motions, it may contribute to episodic mass loss ejections.

$$\Gamma_1 \equiv \left(\frac{\partial \ln P}{\partial \ln \rho} \right)_s = \frac{C_p}{C_v} \chi_\rho, \quad (2.1)$$

where P – pressure, ρ – density, C_p and C_v are specific heats for constant pressure and volume, and the density exponent $\chi_\rho = 1$ for monatomic gas. Lobel (2001) and Lobel et al. (1992) calculated the variation of Γ_1 in Kurucz model atmospheres at different effective temperatures. They determined that for Kurucz models with low gravitational acceleration, there exist areas on the HR diagram, where the stellar atmospheres are unstable to atmospheric instabilities. At $T_{\text{eff}} \sim 6500\text{--}7500$ K, the hydrogen ionisation region is located in the outer parts of the star’s atmosphere, where Γ_1 decreases below $\frac{4}{3}$. Further increase in T_{eff} results in hydrogen being fully ionised and Γ_1 increases. A second such region on the HR diagram is located at around $T_{\text{eff}} \sim 13\,000$ K, where helium becomes singly ionised. Above 16 000 K both hydrogen and helium are completely ionised. Nieuwenhuijzen et al. (2012) established two subregions of the YEV: $T_{\text{eff}} \sim 6300\text{--}8900$ K, where hydrogen ionisation causes low atmospheric stability (marked on Fig. 2.6), and $T_{\text{eff}} \sim 11\,200\text{--}12\,500$ K, where ionisation of helium begins to play a role.

However, recently Glatzel & Kraus (2024) stated that because of the short thermal time scales in the envelopes of YHGs, the analysis of atmospheric stability through the use of adiabatic approximation is not valid. Additionally, even with using the adiabatic approximation in their models, Γ_1 never decreased below $\frac{4}{3}$. Their interpretation uses strange-mode instabilities manifesting through infinitesimal radial perturbations in the stellar atmosphere. Strange modes occur for stars with luminosity-to-mass ratio (in solar units) above 10^4 . Such instabilities occur for luminous stars at all temperatures and might cause pulsationally driven mass-loss.

2.3.4. Extreme mass loss eruptions

Observational indications of instabilities in YHGs have been evident for decades but the cause of eruptive outbursts remains unclear. The prevailing scenario connects the long-term evolution and the eruptive mass loss episodes with the YEV (Nieuwenhuijzen et al., 2012). As the YHG evolves bluewards and its T_{eff} increases, it encounters the YEV region. There, its atmosphere becomes increasingly unstable, which triggers an eruptive episode. The ejected matter creates a cooler pseudo-photosphere around the star, decreasing the observed T_{eff} and the star moves to cooler part of the HR diagram. As the pseudo-photosphere disperses, the T_{eff} appears to increase again until another mass-loss episode occurs, and the cycle begins anew.

These eruptions occur on timescales of years to decades and they have become known as ‘bouncing against the yellow void’. It is unknown, how many times the eruptions can reoccur. It is possible, that the resulting zig-zag motion on the HR diagram only affects the outer atmospheric layers of the star, while its underlying evolution continues normally (de Jager, 1998). Though it has also been suggested, that the corresponding T_{eff} changes of 3000–4000 K reflect evolutionary changes within the stellar interior. The recurring eruptions might continue until the atmosphere of the star stabilises and the star continues on its blueward evolutionary path or explodes as a type II SN (Israelian et al., 1999).

One of the most well-studied YHGs with recurring eruptions is the bright, visually 4th magnitude star ρ Cas. Its major eruption in 1946–47 and the subsequent formation of a cooler circumstellar shell provided the first clear evidence for sporadic and extensive mass ejection events (Sargent, 1961). ρ Cas has a long timeline of strong outbursts with six eruptions recorded in the last 138 years (van Genderen et al., 2025). The most well-known are the 1945–47 event (Sargent, 1961), the 1985–86 event (Boyarchuk et al., 1988a), the ‘millennium outburst’ in 2000–01 (Lobel et al., 2003b), and the most recent smaller-scale event in 2013¹ (Aret et al., 2017b). Similar episodes have been observed in other famous YHGs: IRC +10420 (Oudmaijer et al., 1996), HR 5171 (Chesneau et al., 2014), Var A in M33 (Humphreys et al., 1987), and V509 Cas (de Jager & Nieuwenhuijzen, 1997). Chapter 4 focuses on the history and current variability of V509 Cas.

During the mass-loss outburst, the optical brightness of the star can decrease by more than a magnitude and T_{eff} can decrease by around 3000 K within a few months (Lobel et al., 2003a; Nieuwenhuijzen et al., 2012). During the outburst minimum, TiO bands can appear in the spectrum due to the rapid expansion and cooling of the atmosphere. These are usually seen in much cooler, M-type stars. In 1946, 1986, and 2000 outbursts of ρ Cas, the TiO bands appeared during brightness decline and disappeared within a few months following the brightness minimum. For the ‘millennium outburst’ of ρ Cas Lobel et al. (2003a) measured a lower limit

¹ Author’s note: 13 years have passed since the last outburst, which makes it tempting to hope for another episode soon. At the time of writing this thesis (Feb 2026), ρ Cas shows normal activity.

for mass-loss rate of $\dot{M} = 5.4 \times 10^{-2} M_{\odot} \text{ yr}^{-1}$, over 500 times greater than during quiescent pulsations and of the same order of magnitude as the giant eruptions in LBV η Car.

Different explanations have been proposed for this outburst behaviour.

Hydrogen ionisation instability. This model was proposed by Lobel et al. (2003a). Before the outburst, there is a period of very weak stellar winds, which contributes to build up of momentum in the atmosphere. A release of this energy results first in rapid decompression and then contraction of the atmosphere. During the contraction, the T_{eff} increases to ~ 8000 K. This temperature regime corresponds to the hydrogen ionisation zone and low values of Γ_1 mean that the atmosphere is unstable. The subsequent expansion and cooling triggers an avalanche of hydrogen recombination, release of energy, and accelerating stellar wind. The T_{eff} decreases to ~ 4000 K with the expansion of the atmosphere.

‘Geyser model’. Nieuwenhuijzen et al. (2012) propose that for the YHG applies the ‘Geyser model’ by Maeder (1992). If the thermal timescale in the atmosphere is shorter than the dynamical timescale, a minor thermal instability due to ionisation or supra-Eddington luminosity in some atmospheric layers produces a density inversion in the atmosphere. Thus, the ionisation front can move inwards and any mass ejection beginning in the upper atmospheric layers can rapidly involve matter from the deeper layers, resulting in an eruptive outburst.

Line-driven mass loss. Koumpia et al. (2020) propose that for hotter YHGs located near the high temperature border of the YEV (‘white wall’), line-driven mass loss could provide an explanation. Stellar winds driven by radiation pressure on spectral lines is the main mechanism for mass loss in hot stars. Changes in ionisation balance of Fe create wind bi-stability jumps, where small decrease in T_{eff} cause Fe recombination from Fe IV to Fe II at $\sim 25\,000$ K (Vink et al., 1999) and Fe III to Fe II at ~ 8800 K (Petrov et al., 2016). This increases the stellar wind density and mass-loss rate. The temperature corresponding to the second bi-stability jump is comparable to the location of the ‘white wall’ on the HR diagram.

2.3.5. Quiescent variability

All luminous supergiants are somewhat variable, but the extent of variability depends on the stellar properties and the physical mechanisms. The light curves of YHGs display variability on timescales from days and months to several years. Additionally, they can be variable in colour on timescales from years to decades (de Jager, 1980). A common property of all YHGs is their variable spectral type. During periods of eruptive outbursts, this is pushed to the extreme – ρ Cas changed from K-type star before 1930 to M-type during the outburst in 1946–47 and returned to its ‘normal’ F8 spectral class by 1950 (Sargent, 1961). Significant changes in spectral type can also occur over multi-decade continuous evolution, e.g. IRC +10420 from F8 (Humphreys et al., 1973) to late-A in 20 years (Oudmaijer

et al., 1996). Minor changes in spectral class arise from quiescent low-amplitude variability.

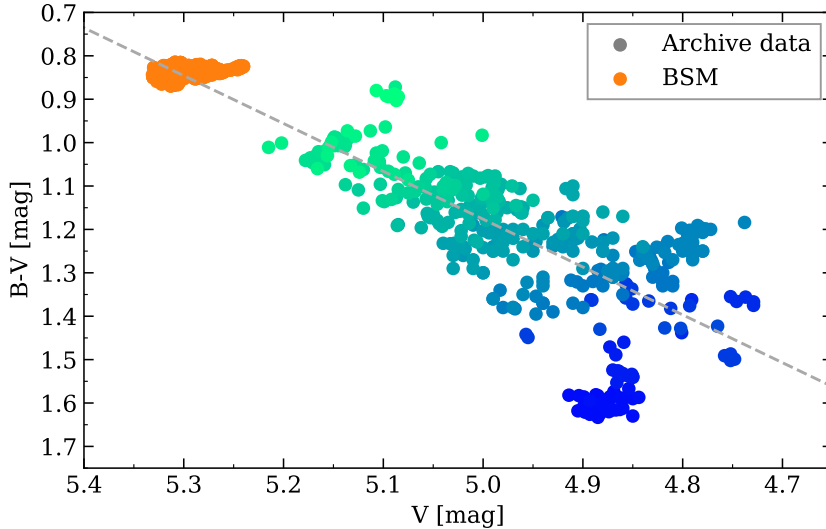


Figure 2.7: Long-term colour change of V509 Cas. The archival data are from Nieuwenhuijzen et al. (2012) and cover the years 1976–1993. The blue-green colour gradient indicates the date of measurements: the oldest points from 1976 are dark blue and the most recent points are light green. Orange data are from Bright Star Monitoring program (PI: T. Eennmäe) covering years 2019-2022. Figure adapted from Paper II.

On timescales of decades, the YHGs undergo changes in colour and spectral class as a result of the T_{eff} changing by several thousand degrees. This has been connected to the recurring mass-loss outbursts and gradual evolution through the YEV (van Genderen et al., 2019). The T_{eff} gradually increases and the colour gets bluer, as the YHG approaches the cool boundary of the YEV. van Genderen et al. (2025) studied three such excursions in ρ Cas preceding the 1986, 2000, and 2013 mass-loss outbursts, when the star was ‘bouncing against the yellow void’. They noted that with each cycle, the star went further into the YEV region and the average T_{eff} of the star increased by ~ 500 K. Nieuwenhuijzen et al. (2012) and Paper II studied the long-term evolution of V509 Cas, and determined that the star has become gradually hotter and bluer from 1976 to 1993 (Fig. 2.7) and is currently situated at the high temperature border of the YEV. The evolution of V509 Cas is further discussed in Chapter 4.

During quiescence, YHGs exhibit quasi-periodic pulsational variability with amplitudes between 0.2 mag and 0.5 mag and periods of several hundred days. Each pulsation cycle is unique. Comparison of four YHGs (ρ Cas, V509 Cas, HD 179821, HR 5171) revealed that the periods and amplitudes are dependent on the T_{eff} – when the T_{eff} is higher, periods and amplitudes are smaller (van Genderen et al., 2019). During quiescent pulsations, T_{eff} can vary by a few hundred degrees (Paper II) and the radial velocity (v_{rad}) variability amplitude is of the order of

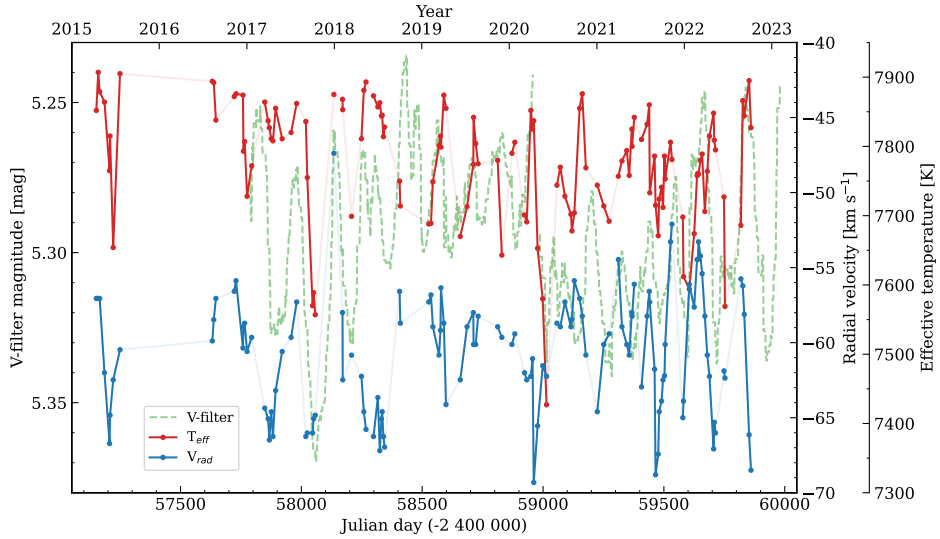


Figure 2.8: Variability of V509 Cas in T_{eff} (red), V-filter magnitude (green), and v_{rad} (blue) during quiescent pulsations. T_{eff} and V magnitude vary in phase and there is a phase shift of around 1/4 of a period between the v_{rad} and T_{eff} curves. The lag duration is approximately 30-80 days. Its length is not constant in time and varies with each pulsation period. Connections have been drawn only between observations taken at intervals of less than 30 days to have a better visual overview of the data. Figure adapted from Paper II.

10 km s^{-1} (Paper II; Klochkova, 2019). In addition, velocity stratification has been detected in some stars (e.g. RW Cep and ρ Cas) where spectral lines formed at different depths in the photosphere show different radial velocities (de Jager, 1980; Klochkova, 2019, Paper II). Observations show that the star’s visual brightness follows the radial velocity curve with an offset of about a quarter of a period in ρ Cas (Lobel et al., 2003a) and V509 Cas (Fig. 2.8; Paper II).

In addition to variability in T_{eff} , colour, and radial velocity, the YHGs also show variations in spectral line profiles. Klochkova (2019) noted variability in spectral absorption lines due to pulsations in ρ Cas, V509 Cas, IRC +10420, and HD 179821 over several years. The variability can occur due to mass loss (e.g. emission components in $\text{H}\alpha$ in ρ Cas; Klochkova, 2019), variable stellar wind (e.g. V509 Cas; Klochkova, 2019), or shocks propagating through the atmosphere (ρ Cas; de Jager et al., 1997). The atmospheric shocks are caused by pressure waves generated by turbulent motions in the convective regions of the star, and they appear as microturbulent broadening of spectral lines (de Jager et al., 1991).

Quiescent YHGs lose mass through stellar winds. The wind has been measured to be supersonic in the case of ρ Cas, causing variable absorption in the violet wings of the spectral lines. The strength of the wind varies depending on T_{eff} during the star’s pulsational cycle (Lobel et al., 1998). Many YHGs are too hot for the dust driven winds of RSGs to be effective, their wind dynamics might depend on pulsations in the photosphere (Gorlova et al., 2006). The quiescent mass loss is

around 10^{-5} – $10^{-6} M_{\odot} \text{ yr}^{-1}$ (Israeli et al., 1999; Lobel et al., 1998), but can be an order of magnitude higher for the dusty YHGs IRC +10420 and IRAS 17163-3907 (Oudmaijer et al., 1996; Wallström et al., 2017).

YHGs are non-radial pulsators, as they display slow and irregular pulsational motions in their extensive atmospheres (de Jager, 1980). The driving mechanism of YHG pulsations remains unclear, below is a brief overview of two possible explanations that are not mutually exclusive.

κ -mechanism. It has been proposed that the driver of pulsations in YHGs is the κ -mechanism in helium ionisation zones (Fadeyev, 2011). κ -mechanism is the main driver of pulsations in stars with T_{eff} below ~ 6300 K, where the ionisation zone is located so that pulsations are excited instead of dampened. The mechanism depends on cyclically variable opacity due to the ionisation and recombination of helium. Compression ionises the helium, increasing the opacity and temperature. This causes expansion, cooling, and recombination of helium, releasing energy. The shell contracts and the cycle repeats. This process drives radial pulsations in cepheids (Kippenhahn & Weigert, 1990). However, YHGs are considered non-radial pulsators (Lobel et al., 1994). When the hydrogen and helium ionisation zones are located too close to the stellar surface they cannot excite radial pulsations, but they can drive non-radial modes. Lobel (2001) determined that for low effective gravity stars on the extended cepheid instability strip, stable non-radial pulsations can be excited by partial non-local thermodynamic equilibrium (NLTE) ionisation of hydrogen in the optically thin part of the atmosphere. The low values of Γ_1 create suitable conditions for stable non-radial pulsations in YHGs. Pulsations combined with strong convective motions can excite unstable modes with very fast growth rates, resulting in eruptive mass loss.

Gravity waves. For YHGs hotter than the granulation boundary (G0-5 spectral class, $T_{\text{eff}} \gtrsim 5100$ K), the drivers of pulsations are proposed to be internal gravity waves. For cooler stars the large-scale motions are dominated by (subsurface) convection. Gravity waves arise in regions above the convective zone due to the rising convective plume penetrating (overshooting) into the stable upper photospheric layers (de Jager et al., 1991). This can happen in the YHG photospheres above optical depth $\tau_{\text{Ross}} \sim 0.5$ – 0.3 where the supergiant atmosphere is stable against convection. The light and velocity variations in YHGs are similar to the Brunt-Väisälä frequencies. Brunt-Väisälä frequency describes the oscillation of a parcel of fluid when displaced into a stable layer. High-mode gravity waves (with long wavelengths comparable to a fraction of stellar radius) may be the cause for quasi-periodic variability in YHGs and manifest as macroturbulence in spectral line profiles (de Jager et al., 1991).

2.3.6. Circumstellar environments

Clear indication of previous mass-loss events in the form of circumstellar nebulae has been found for a few Galactic YHGs: IRAS 17163-3907 (also known as

the Fried Egg Nebula; Koumpia et al., 2020; Lagadec et al., 2011), HD 179821, IRC +10420 (Oudmaijer et al., 2009), which may indicate an exceptional evolutionary path for these objects (Castro-Carrizo et al., 2007). At large scales, the recurring mass-loss episodes have formed spherical shells around the stars. However, smaller scale clumps and asymmetries in the morphology of these shells indicate asymmetric mass loss activity (Castro-Carrizo et al., 2007; Koumpia et al., 2020). For example, the nebula surrounding IRAS 17163-3907 has three separate shells, each formed in a mass-loss outburst within the last 100 years (Koumpia et al., 2020).

Three other YHGs, ρ Cas, V509 Cas, and HR 5171 have had multiple eruptive mass-loss events within the last century, but show no indication of large-scale nebulae (Schuster et al., 2006). For YHGs without significant nebulosity, evidence of circumstellar matter can be found through circumstellar emission lines. Narrow central emission components in resonance lines of Ba II and Ca I originate from a cooler circumstellar shell around ρ Cas (Lobel et al., 1998) and RW Cep (Paper III). In ρ Cas, Shenoy et al. (2016) found evidence of the 1946 mass-loss outburst as a thin dust shell visible in infrared $> 10 \mu\text{m}$, but no indication of the more recent outbursts in 1986 (Boyarchuk et al., 1988a), 2000 (Lobel et al., 2003a) or the smaller one in 2013 (Kraus et al., 2019).

Forbidden emission lines can give information on unique morphology of the circumstellar environments. [Ca II] and [O I] emission lines are connected to disc-like circumstellar structures (Aret et al., 2012), and have been found in ρ Cas (Lobel et al., 1998), V509 Cas (Aret et al., 2017a,c), IRC +10420 (Aret et al., 2017a,c). Rather unexpected [N II] emission features originating from a circumstellar shell with temperature higher than the stellar photosphere are present in two stars: HR 5171 (Warren, 1973) and V509 Cas (Sheffer & Lambert, 1992). The [N II] emission could form in a low-density high-temperature envelope, excited by the hot companions of these stars (Sheffer & Lambert, 1992).

Variable emission lines of other neutral and ionised atomic spectral lines are visible in the YHGs as well. Some examples would be the Fe II and Sc II emissions in V509 Cas (Paper II; Kasikov et al., 2022) discussed in Chapter 4, and Ca II emission in ρ Cas (Gorlova et al., 2006). Na I near-infrared doublet emission lines indicate the presence of a high-temperature low-density shell surrounding the star, where the line formation region is shielded from the stellar radiation (Oudmaijer & Wit, 2013). This emission has been detected in HR 5171 (Wittkowski et al., 2017), in HD 179821 (Kraus et al., 2023), and in ρ Cas (Gorlova et al., 2006).

2.4. Binarity among massive stars

It has been estimated that around 70–90% of O-type stars in the Milky Way are in binary systems (Sana et al., 2012, 2014). But for RSGs, the observed binary fraction is only around 15–30% (Dai et al., 2025; Dorda & Patrick, 2021; Neugent et al., 2020; Patrick et al., 2019). Due to the significant increase in stellar radius as

the star crosses the HR Diagram, binaries with orbital periods shorter than 1500 days are expected to interact with their companions (Patrick et al., 2020). The binary interactions can lead the primary star to become a stripped star and find its end in a SN explosion (Podsiadlowski et al., 1992). The secondary star would continue to evolve to a RSG with a compact companion or if the binary system is disrupted by the SN, become an unbound ‘walkaway star’ (Renzo et al., 2019).

A significant contribution to the low observed binary fraction in cool massive stars may be the difficulty of detection, especially in the cases where the companion is a low-mass and much less luminous young stellar object (YSO). For example, the efforts to detect the low-mass companion of Betelgeuse required photometric and radial velocity measurements over many decades to constrain its ~ 2100 -day orbital period and stellar properties (e.g. Goldberg et al., 2024; MacLeod et al., 2025; O’Grady et al., 2025). Over a hundred years after the companion’s existence on a 2100-day orbit was first postulated (Bottlinger, 1911), its successful detection using speckle interferometry was possible (Howell et al., 2025).

The binary fraction of YSGs and YHGs is not well constrained. In the LMC and SMC, O’Grady et al. (2024) reported a binary fraction between 20–60% ($\sim 44\%$ in SMC and $\sim 37\%$ in LMC) based on UV excess, while Patrick et al. (2025) reported the binary fraction in the SMC for AF-type supergiants at around 8% with a maximum of 15%. In the Milky Way YSG and YHG 35-star sample (Paper I), we reported a minimum binary fraction of 22% based on confirmed binary systems, with an expected binary fraction near 50%, if including possible binaries proposed in the literature and based on RUWE index values from *Gaia* (metric used for detecting unresolved binaries; Castro-Ginard et al., 2024). Interestingly, most YHGs had possible binary companions.

2.5. Future beyond yellow hypergiant stage

The future of YHGs remains unclear. To date, no YHG has been observed to pass through the yellow void instability region (de Jager, 1998). Single-star evolution models predict evolution past the YHG stage (Ekström et al., 2012), leading the star to become a hot post-RSG supergiant, such as an LBV (de Jager, 1998) or a B[e]SG (Aret et al., 2017a,c). Further complexity arises from possible binary evolution. Binary interactions can strip the YHG/YSG of its outer envelope and lead to a core-collapse supernova explosion (Filippenko, 1997). However, the most massive RSGs and YHGs might collapse directly into black holes (Smartt et al., 2009). The following sections give an overview of the possible future scenarios.

2.5.1. Luminous blue variable

The classical LBVs are rare evolved luminous ($\log(L/L_{\odot}) > 5.4$) hot supergiants. Two luminosity classes are distinguished – above and below $\log(L/L_{\odot}) \sim 5.8$. The higher luminosity LBVs are an unstable evolutionary state for stars more massive than $M_{ZAMS} = 50 M_{\odot}$. The less luminous LBVs are suggested to be in a

post-RSG evolutionary state, and thus, successors of YHG (Lamers et al., 1983; Stothers & Chin, 1996). They have lost most of their initial mass during the RSG stage, and continue to heavily lose mass (rates $\sim 10^{-6} - 10^{-4} M_{\odot}/\text{yr}$) in strong radiatively-driven stellar winds and mass-loss outbursts (Humphreys & Davidson, 1994). The outbursts (also known as S Dor cycles after a star of the same name in the LMC) are the main criterion for LBV classification. The outbursts last years to decades and the star brightens by 1-2 mag, reddens, and appears as a cooler AF-type supergiant. Quiescent LBVs are difficult to identify as they share many spectral characteristics with other evolved massive stars in the same region of the HR diagram. Many LBVs are surrounded by extensive nebulae as a result of the star’s mass-loss history, which may be highly asymmetric with bipolar outflows or ring-like structures (e.g. Weis, 2003). A few of the most luminous LBVs undergo giant eruptions, η Car is one of the most famous of them (also depicted in Fig. 1.1 as an illustrative example of the LBV class).

A commonly suggested future for a YHG is to pass through the YEV and come out on the other side as an LBV (de Jager, 1998). This sequence also arises from stellar evolutionary models (e.g. Meynet et al., 2015). YHG have been even proposed as the ‘missing LBVs’. Smith et al. (2004) found a lack of LBVs with luminosities $\log(L/L_{\odot}) = 5.7$ and suggested that dense stellar winds may create a pseudo-photosphere that makes the B-type star appear as a cooler AF-type supergiant, such as a YHG on the HR diagram. Qualitatively, there are similarities in the variability and outburst behaviours of YHG and LBVs.

Just as for YHG, the making of an LBV in stellar evolution models depends on the model assumptions and mass-loss rate in the RSG stage. Mass loss during the LBV phase can evolve the star into a low-luminosity WC-type Wolf-Rayet star (Meynet et al., 2015). However, the low-luminosity LBVs have also been observed as SN progenitors, and Geneva rotating stellar models with 20–25 M_{\odot} predict type IIb SNe with LBV progenitors (Groh et al., 2013; Meynet et al., 2015). As an alternative origin scenario, Smith (2019) and Smith & Tombleson (2015) propose that LBV phenomenon arises from interactions in a binary or multiple system. LBVs could be former mass gainers from companion’s Roche-lobe overflow that have received a kick in the SN explosion. Or alternatively, they could be stars rejuvenated in a merger. Binary origin for YHG and YSG remains under question as well (Patrick et al., 2025) and as the origin and future of LBVs is not well established, it is not possible to make a robust evolutionary continuity between the YHG and LBVs.

2.5.2. B[e] supergiant

B[e] stars are B-type stars with allowed and forbidden spectral emission lines (e.g. $H\alpha$, Fe II, [Fe II], He I, [O I], and [Ca II]) and strong infrared excess from hot circumstellar dust (Allen & Swings, 1976). The B[e] stars consist of a wide array of stars in various evolutionary stages from young pre-MS stars to evolved

and massive objects, that are all grouped together under the ‘B[e] phenomenon’ label (Lamers et al., 1998). The spectral emission lines arise from a keplerian disc around the star. In the context of YHG evolution, we consider the connection to blue supergiant B[e] stars (B[e]SGs).

The B[e]SGs are located in the HR diagram at luminosities ($\log(L/L_{\odot}) \sim 5.0$ – 5.9) and effective temperatures similar to the less luminous LBVs, and can be easily confused with LBV candidates (Humphreys et al., 2017). Some of the B[e]SGs are also surrounded by extended nebulae (e.g. Liimets et al., 2022). Their keplerian discs may be decretion discs formed from matter ejected from the star (Lee et al., 1991) or formed as a result of binary interactions (Miroschnichenko, 2007). The K-band spectra of many B[e]SGs show CO emission lines formed in the disc, indicating its composition of processed matter ejected from the stellar surface. Based on $^{12}\text{CO}/^{13}\text{CO}$ ratio measured from infrared CO lines, Oksala et al. (2013) found that B[e]SGs are likely in post-MS pre-RSG evolutionary state. However, the expected isotope ratio in a specific evolutionary phase depends on the evolutionary model assumptions and is strongly dependent on stellar rotation (Kraus, 2019). Additionally, the CO emission lines are not present in all B[e]SGs. For some objects, CO may appear in absorption (Kourniotis et al., 2018), but for others it is a transient phenomenon, appearing or disappearing over years or decades (e.g. Oksala et al., 2012).

Evolutionary models by (Stothers & Chin, 1996) predict B[e]SGs to be directly post-MS and also post-RSG objects, discerning their H-rich and H-poor phases. Possible evolutionary link between LBVs and B[e]SGs has also been proposed based on similarities in spectroscopic features, spectral variability, equatorial outflows, and in some cases, bipolar nebulae (Marston & McCollum, 2008; Morris et al., 1997; Oksala et al., 2012). Similar reasoning based on similarities in circumstellar environments (CO bands, axisymmetric outflows, forbidden emission lines [O I] and [Ca II] indicating disc-like structures) has motivated the connections between B[e]SGs and YHGs as well (Aret et al., 2017a,c; Davies et al., 2007). It is possible, that if the YHGs pass through the YEV, they continue to display B[e] qualities.

2.5.3. Supernova

The increase in available archival data allows for identification of supernova progenitors. In some cases, the pre-explosion images have revealed luminous yellow massive stars (e.g., Niu et al., 2024; Reguitti et al., 2025; Yamanaka et al., 2025). Based on the light curves, the core-collapse SNe with possible yellow progenitors have been classified type Ib (Kilpatrick et al., 2021), IIb (e.g., Aldering et al., 1994; Maund et al., 2011), II-P (Elias-Rosa et al., 2009), and II-L (Elias-Rosa et al., 2010).

The different types are indicative of the mass-loss history of the progenitors (see reviews by Filippenko, 1997, 2005): SNe type Ib originate from stars stripped

of their hydrogen envelopes; the type II-P had hydrogen-rich progenitors, mostly RSGs; Type II-L progenitors had less massive hydrogen envelopes, but some circumstellar gas. Between these types are the SNe type IIb, which show hydrogen lines early in their evolution, but after a few months begin to resemble type Ib SNe, so their precursor could have been a (mostly) stripped star (Woosley et al., 1987). The loss of a star’s hydrogen envelope could occur due to stripping through binary interactions or enhanced mass-loss activity in the progenitor (Filippenko, 1997). The HR diagram positions of luminous yellow progenitor candidates are not compatible with the classical evolutionary tracks from single-star models (Georgy, 2012).

Identifying the possible progenitors to SNe is not unambiguous. A blend of a RSG and a BSG or stars in a compact cluster could produce the observed yellow colour (Elias-Rosa et al., 2009; Maund et al., 2015). Several type IIb SNe (e.g. Aldering et al., 1994; Maund et al., 2011; Niu et al., 2024; Reguitti et al., 2025) have been connected to yellow progenitors with luminosities in the range of $\log(L/L_{\odot}) = 4.9 - 5.1$, which is higher than the luminosities of normal type II SN progenitors (Reguitti et al., 2025). The SN may originate from binary or single-star evolution. Long et al. (2022) considered binary stellar evolution models with Roche-lobe overflow and determined that the occurrence of type IIb SNe depends on the orbital period of the binary system: binaries with orbital periods between 50 and 300 days explode as YSGs. Systems with shorter or longer periods explode in other evolutionary stages as different types of SNe. Georgy (2012) considered the single-star scenario for SN precursors in the effective temperature range of $3.6 \lesssim \log(T_{\text{eff}}) \lesssim 3.8$. Increasing the mass-loss rates in the RSG stage by factors of 3, 5, and 10, they were able to reproduce the positions of post-RSG yellow SN progenitors in the HR diagram, and also the expected type III/Ib SNe. Thus, luminous yellow massive stars in post-RSG evolutionary stage may end their lives as supernovae following enhanced mass loss as RSGs.

2.5.4. Failed supernova

It is possible, that a massive star does not end its life in a SN, but collapses directly into a black hole. The collapse depends on metallicity and mass-loss estimates (O’Connor & Ott, 2011). It is possible, that the star simply disappears (Kochanek et al., 2008) or appears as a dimmer red nova for about a year (Antoni & Quataert, 2023; Lovegrove & Woosley, 2013). The failed SN scenario has been proposed as an explanation to the RSG problem (Smartt et al., 2009). As of February 2026, at the time of writing this thesis, five candidates have been identified, three of which involve luminous yellow stars.

NGC 6946-BH1. This candidate in the NGC 6946 galaxy was detected in the Large Binocular Telescope survey for failed SNe (Gerke et al., 2015). The star brightened by 3.5 mag in optical for a few months before disappearance. A dusty YHG progenitor has been proposed with T_{eff} around 5000 K (Gerke et al., 2015;

Humphreys, 2019). The star disappeared in optical (S. M. Adams et al., 2017), but its luminosity persists at mid-infrared wavelengths (Beasor et al., 2024). An alternative stellar merger scenario has been proposed, and the collapse is disputed (S. M. Adams et al., 2017; Beasor et al., 2024; Kochanek et al., 2024, and references therein).

M31 2014-DSI. De et al. (2026) observed an increase in brightness in infrared over a two-year period before the disappearance. The progenitor’s SED fits a dusty post-RSG star with $T_{\text{eff}}=4500$ K and a high mass-loss rate $\sim 10^{-4} M_{\odot} \text{ yr}^{-1}$. Again, an alternative explanation could be a stellar merger (Beasor et al., 2026).

NGC 3021-OC1. Reynolds et al. (2015) identified a luminous yellow F8 supergiant in NGC 3021, which dimmed by about 1.5 mag within a year. Another epoch a year later revealed it still at similar brightness. Without further follow-up observations, it remains unclear if this is a possible failed SN, or it has a more ordinary cause for the dimming.

2.6. Motivation for the thesis

The physical processes that govern stellar evolution in the advanced post-RSG phases remain poorly understood. Addressing these gaps relies on combining detailed single-star analyses with population-level studies that link different classes of evolved massive stars. Given their instabilities, the YHGs serve as an ideal population for exploring late-stage evolution and processes in stellar atmospheres.

The YHGs of the Milky Way are a heterogeneous family. Some of them are surrounded by dense nebulae of matter ejected in the last few thousand years (e.g. IRC +10420; Shenoy et al., 2016). Others show only a small amount of infrared excess, but have evidence of major atmospheric instabilities and eruptions (ρ Cas; Shenoy et al., 2016, V509 Cas; Nieuwenhuijzen et al., 2012). It remains unclear, whether this variety in circumstellar qualities signals different stages of evolutionary journey through the YHG phase, or if the different circumstellar environments imply fundamentally different evolutionary histories. Some similarities in circumstellar environments can also be found with the LBVs and B[e]SGs, which are possible future states of the YHGs.

Information on the evolutionary histories of YSGs and YHGs can be indirectly revealed by the wider context in which they are found. Memberships in stellar clusters can help determine their ages, and affiliation in an OB association places them among other young massive stars (e.g. Rate et al., 2020). Conversely, an unexpectedly high space motion and distance from other young and massive stars could imply a history of interactions and dynamical ejections (e.g. Smith & Tombleson, 2015; Martin et al., 2025, and references therein). This motivated us to study the stellar populations where the Galactic YHGs and YSGs are located, a first step on a project to provide a homogeneous characterisation of their (extra-) Galactic populations.

The short duration of the YHG phase results in changes that appear as if stellar evolution is happening in a human lifetime. On timescales of decades, the YHGs may increase in T_{eff} by several thousand degrees (IRC +10420; Koumpia et al., 2022), or undergo multiple eruptive mass ejections (ρ Cas; van Genderen et al., 2019). Several YHGs are located on the HR diagram near the high-temperature border of the YEV, prompting close monitoring. One such object is V509 Cas, a star that seems to have left behind a period of recurring eruptions and has now reached a more stable evolutionary phase (Nieuwenhuijzen et al., 2012). Is the star truly stabilising and nearing the end of the YHG phase? If so, could we predict what type of star it would become based on similarities in spectral and circumstellar features?

The origin of YHGs is as obscured as their future. Depending on the mass-loss prescription and the convective processes assumed in the single-star evolution models, the YHGs may or may not appear. Additionally, the physical processes behind the pulsations and eruptive mass loss remain open for debate. From observational perspective, one of the best candidates for a future as a YHG is the Galactic red hypergiant RW Cep. It is hotter than other red hypergiants, located between the red and yellow massive stars in the HR diagram. RW Cep gained significant attention due to its mass-loss eruption and the Great Dimming in 2020–2024, which provided a unique chance to closely monitor the star’s recovery.

3. THE FAMILY OF YELLOW SUPER- AND HYPERGIANTS

This Chapter is based on Paper I: *Painting a Family Portrait of the Yellow Super- and Hypergiants in the Milky Way I. Constraining the Distances and Luminosities* A. Kasikov, A. Mehner, I. Kolka, and A. Aret, 2026, A&A 708, A78.

Stellar population studies of young star clusters have revealed numerous massive stars in transitional evolutionary phases (recently, e.g. Maíz Apellániz & Negueruela, 2025; Marco et al., 2025). Knowledge of the surrounding stellar population and environment provides context for understanding the evolution of massive stars. Homogeneously determined observational parameters of YHGs and YSGs provide a basis for comparison with stellar evolutionary models, improving our overall understanding of evolutionary pathways of luminous yellow massive stars and their role as supernova progenitors (e.g. Aldering et al., 1994; Crockett et al., 2008; Kilpatrick et al., 2017; Maund et al., 2011; Niu et al., 2024; Reguitti et al., 2025; Tartaglia et al., 2017).

Studies of YSGs and YHGs in the Milky Way have been hampered by uncertain distances and high extinction in the Galactic plane. In the era of *Gaia* and due to the efforts by Bailer-Jones et al. (2021), the distance estimates for many stars have improved significantly. For objects that lack reliable *Gaia* parallaxes, other indirect methods can be used to estimate distances. We combined and compared the results of two complementary methods. The first method is based on an analysis of nearby stars: since many YHGs and YSGs are known or suspected members of stellar clusters or OB associations, confirming these memberships and combining the parallaxes of nearby stars (e.g. Campillay et al., 2019) can help refine their distance estimates. The second method compares the stellar radial velocities with the Galactic H I kinematics. Agreement between these independent methods increases confidence in the derived distances.

3.1. Sample selection

We queried Simbad for YSGs and F and G spectral class stars with luminosity class Ia or Iab with infrared excess ($V - K > 3$ mag). From the resulting list, we excluded objects that are identified in the literature as luminous post-asymptotic giant branch (post-AGB) stars. We also excluded stars with reliable *Gaia* DR3 parallaxes that place them closer than expected for luminous YSGs. We added additional luminous YSGs from the literature (de Jager, 1998; Kovtuykh et al., 2012; Mantegazza, 1992) and included stars that have been proposed as YHG candidates: IRAS 18357-0604 (Clark et al., 2014) and HD 144812 (Kourniotis et al., 2025). The resulting 25 stars form our sample of YSGs.

We also included the well-known YHGs in the Milky Way: V509 Cas, ρ Cas, IRC +10420, HR 5171, 6 Cas, HD 96918, and the yellow-red hypergiant RW Cep

(de Jager, 1998), IRAS 17163-3907 (Lagadec et al., 2011), HD 179821 (Hawkins et al., 1995), and [FMR2006] 15 (Figer et al., 2006). When we mention YHGs, we refer to the ten stars in this list.

We did not aim for a complete census, but rather for a representative sample of the most luminous YSGs and YHGs. The final sample of 35 objects is presented in Table 1.

3.2. Distances based on stellar group identification

Gaia Data Release 3 (DR3; Gaia Collaboration et al. 2016, 2023) has provided proper motion and parallax measurements for ~ 1.3 billion sources, enabling improved determinations of distances and cluster memberships. However, *Gaia* parallaxes are subject to systematics and biases. For YHGs and YSGs, the parallax values can have large uncertainties ($>20\%$) and, in some cases, they are even negative. A major source of error is their brightness; approximately half of our sample is brighter than $G = 6$ mag. Another source of astrometric error for cool massive stars is caused by photocentric variability due to surface convection (El-Badry, 2025; Chiavassa et al., 2011; Pasquato et al., 2011). Additionally, some stars have high values of the renormalised unit weight error (RUWE), indicating poor astrometric fits, which may result from an unresolved binary companion (e.g. Castro-Ginard et al., 2024) or circumstellar structure (Fitton et al., 2022).

Bailer-Jones et al. (2021) provided probabilistic distance estimates that take the Galactic structure into account and mitigate the limitations of the simple $1/\text{parallax}$ distance estimate. Although generally more reliable, these distance estimates still require careful interpretation. In several cases, the Bailer-Jones et al. (2021) distances disagree with the values commonly adopted in the literature (see Table 1). For stars with $\text{RUWE} < 1.4$ and parallax uncertainties better than 20% , the Bailer-Jones et al. (2021) distances are likely to be reliable.

To improve the distances for YHGs and YSGs with poor *Gaia* parallaxes, we explored their kinematics based on proper motions in the context of their surrounding stellar environments, that is, nearby star clusters, OB associations, and regions hosting young stellar objects (YSOs). We cross-matched several catalogues of open clusters and OB associations with *Gaia* data. Membership in these co-moving groups implies a common distance.

To determine possible open cluster memberships, we queried the catalogue of Hunt & Reffert (2024). We counted a YHG or YSG as a member of a cluster when its projected on-sky position was within the cluster boundaries and its proper motion was within 3σ of the cluster mean proper motion. When reliable parallaxes were available, we also used them to confirm membership. We verified whether the stars are members of any known OB associations listed by Mel'nik & Dambis (2017). We compared the proper motions of the YHGs and YSGs with members of the OB associations in the catalogue by Chemel et al. (2022) to infer a possible affiliation. OB associations extend farther than clusters in the area projected on sky

and are less tightly connected in proper motion space. We counted a YHG or YSG as affiliated with an OB association when at least two association members were located within a radius of 1 deg on the sky and within a radius of 0.5 mas yr^{-1} in proper motion space. In most cases, significantly more stars had a similar proper motion in the same sky region. We list possible cluster and OB association memberships in the column “Ident. cluster/assoc.” of Table 1.

To estimate the group-based distance for each target, we identified stars with high-quality astrometric data belonging to the same population. Proper motions and positions are not enough to distinguish between stellar populations, and another criterion is therefore needed (e.g. colour index was used by Negueruela et al., 2022). We used the effective temperature T_{eff} from *Gaia* GSP-Phot as an additional criterion. Since we searched for co-located and co-moving populations associated with young clusters or OB associations, we limited our search to B-type and early A-type stars with effective temperatures $8700 \text{ K} < T_{\text{eff}} < 18000 \text{ K}$. This approach assumes that YSGs or YHGs are still physically associated with their birth environments. When the star has migrated or has been ejected from its birth environment, we might not be able to identify a co-moving group, and this method becomes unreliable. We followed the method given by Campillay et al. (2019) and Maíz Apellániz et al. (2021a,b).

1. We selected from *Gaia* DR3 stars within a $10'$ on-sky radius based on following criteria:

- hot stars ($8700\text{K} < T_{\text{eff}} < 18000\text{K}$)
- good astrometry ($\text{RUWE} < 1.4$)
- bright sources ($G < 18 \text{ mag}$)
- reliable parallaxes ($\text{parallax/error} > 5$)
- five-parameter astrometric solution ($\text{ASTROMETRIC_PARAMS_SOLVED}=31$)

2. We corrected the *Gaia* proper motions for known biases affecting bright targets following the method of Cantat-Gaudin & Brandt (2021). This affects stars brighter than $G \lesssim 13 \text{ mag}$ due to the different mode of observations used for bright targets. The proper motion bias depends on the magnitude of the target and reaches $80 \mu\text{as yr}^{-1}$ for targets with $10 < G < 13 \text{ mag}$. The range of the proper motion cut is flexible and depends on the stellar environment of each YSG in our sample. By exploring the scatter of proper motions of stars recognised as members of a single cluster in the catalogue of Hunt & Reffert (2024), we found that cluster stars typically have a dispersion in proper motion of $\sim 0.2\text{--}0.3 \text{ mas yr}^{-1}$. In contrast, stars in OB associations in the catalogues of Chemel et al. (2022) and Mel’nik & Dambis (2017) are less strongly bound, showing a proper motion dispersion of $\sim 1\text{--}2 \text{ mas yr}^{-1}$. Thus, depending on the stellar environments surrounding each target, the cut radius varied from 0.1 to 1.5 mas yr^{-1} .

3. We corrected the parallaxes of the final sample for the *Gaia* zero-point offset (Lindgren et al., 2021a)¹. The parallax bias (zero point) is a function depending

¹ Using the Python code https://gitlab.com/icc-ub/public/gaiadr3_zeropoint

on magnitude, colour, and ecliptic latitude and must be subtracted from the parallax given in *Gaia* DR3 catalogue:

$$\bar{\varpi}_{\text{corr}} = \bar{\varpi} - Z(G, \nu_{\text{eff}}, \beta), \quad (3.1)$$

where G is the G -filter magnitude, ν_{eff} is the effective wave number from *Gaia* photometric pipeline, β is the ecliptic latitude. These offsets are small (~ 0.02 – 0.04 mas).

4. For each parallax, we calculated the ‘true’ or ‘external’ uncertainty. The parallax uncertainties given in the *Gaia* catalogue are underestimated and do not take into account systematic uncertainty (Fabricius et al., 2021).

$$\sigma_{\text{ext}} = \sqrt{k^2 \sigma_{\text{int}}^2 + \sigma_s^2}, \quad (3.2)$$

where k is a constant defined below, σ_{int} is the parallax uncertainty given in the *Gaia* catalogue, and σ_s is the systematic uncertainty, measured as $10.3 \mu\text{as}$ (Maíz Apellániz et al., 2021b). The systematic parallax uncertainty gives a minimum distance uncertainty of $\sim d\%$ for a star at d kpc (Maíz Apellániz et al., 2021b).

The value of the multiplicative constant k depends on G magnitude and describes underestimation of random uncertainties. It is given with the following equation (Maíz Apellániz et al., 2021b):

$$k = \begin{cases} 1.1 & G \leq 11 \\ 1.1 + 0.6(G - 11) & 11 < G \leq 12 \\ 1.7 - 0.1(G - 12) & 12 < G \leq 18 \\ 1.1 & 18 < G \end{cases} \quad (3.3)$$

5. We combined the parallaxes following the recipe of Maíz Apellániz et al. (2021b) and Campillay et al. (2019). Combining parallax information of stars at small separations requires taking into account correlated uncertainties. The combined group parallax is:

$$\bar{\varpi}_{\text{g}} = \sum_{i=1}^n w_i \bar{\varpi}_{\text{corr},i}, \quad (3.4)$$

Where w are the weights depending on external uncertainties:

$$w_i = \frac{1/\sigma_{\text{ext},i}^2}{\sum_{i=1}^n 1/\sigma_{\text{ext},i}^2}. \quad (3.5)$$

The group parallax uncertainty is:

$$\sigma_{\text{g}}^2 = \sum_{i=1}^n w_i^2 \sigma_{\text{ext},i}^2 + 2 \sum_{i=1}^{n-1} \sum_{j=1}^n w_i w_j V_{\bar{\varpi}}(\theta_{ij}), \quad (3.6)$$

where the first term describes uncertainties of individual stars and the second term describes correlated uncertainties. $V_{\varpi}(\theta_{ij})$ is the angular covariance function from Lindegren et al. (2021b):

$$V_{\varpi}(\theta) \simeq (142 \mu\text{as}^2) \times \exp(-\theta/16^\circ), \quad (3.7)$$

where θ is the angular separation of the stars.

6. We converted the group parallax into a geometric distance using the generalized gamma distribution (GGD) prior of Bailer-Jones et al. (2021)².

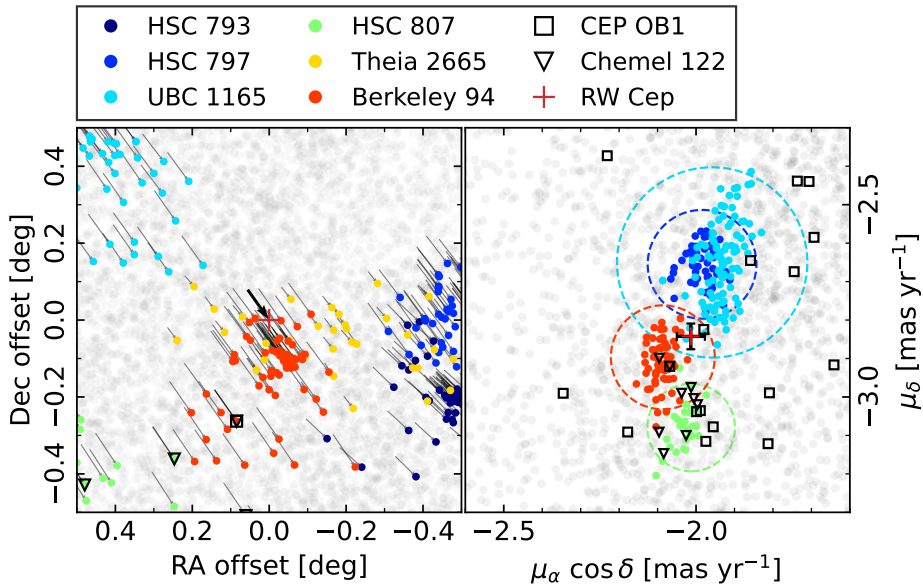


Figure 3.1: Sky region around RW Cep (red cross). Left panel: Projected offsets on sky. Right panel: Proper motions. Field stars from *Gaia* are marked in grey (one in ten is plotted), open clusters from Hunt & Reffert (2024) are marked in coloured points, members of the OB associations Cep OB1 from Mel’nik & Dambis (2017) and no. 122 (Chemel et al., 2022) are marked with open symbols (some members overlap between the two catalogues). The arrows in the left panel indicate the motion of cluster and OB association stars over the past 0.1 Myr based on their proper motions. The coloured circles on the right panel indicate 3σ limits of proper motion scatter of each cluster.

We use RW Cep as an illustrative example of the method. RW Cep has previously been identified as a member of open cluster Berkeley 94 (Delgado et al., 2013) or a member of the Cep OB1 association (Humphreys, 1978). However, the distance in from *Gaia* DR3 parallax is 6666_{-1006}^{+1561} pc with $\varpi/\sigma_\varpi = 3.33$. We find, that the proper motion of RW Cep is within the 3σ limit of Berkeley 94 (Fig. 3.1), located at a distance of 4000 ± 40 pc (Hunt & Reffert, 2024). The other cluster in the same sky region, Theia 2665, is located in the foreground and has a very different proper

² Using the interactive Jupyter Notebook based tool <https://github.com/ElisaHaas25/Interactive-Distance-Estimation>

motion. The members of association no. 122 (Chemel et al., 2022) have proper motions similar to clusters Berkeley 94 and HSC 807, which is located nearby in the sky at the same distance (3900 ± 60 pc; Hunt & Reffert, 2024). Following the criteria listed above, we selected stars with proper motions similar to that of RW Cep within 0.1 mas yr^{-1} , resulting in a sample of 21 stars. We discarded any obvious outliers and stars whose parallaxes deviated by more than 1σ from the sample mean value, resulting in a final selection of 15 stars. The resulting mean parallax for the stars surrounding RW Cep is $\varpi = 0.2558 \pm 0.0103$, which gives a geometric distance of 3921_{-157}^{+168} pc, where the errors correspond to the 68% confidence interval. Given the similarity in proper motion and spatial proximity to Cep OB 1, located at a distance of 3470 pc (Humphreys, 1978), RW Cep might be a member of this association. For the same reasons, RW Cep might belong to the same region as association no. 122 identified by Chemel et al. (2022) at a distance of 3876 pc.

A YHG or YSG might still belong to a stellar group even when no nearby co-moving stars are identified in our search. We estimated the limiting distance at which hot stars would still fall within our criteria. As a representative case, we considered a B3 main-sequence star with $T_{\text{eff}} = 17000$ K and an absolute G -band magnitude $M_G = -1.19$ mag.³ We adopted an average visual extinction in the Galactic disc of $A_G \sim 1 \text{ mag kpc}^{-1}$. The extinction value varies strongly with direction and the local extinction law: in the solar neighbourhood, $A_V \sim 1 \text{ mag kpc}^{-1}$ and $0.80 \leq A_G/A_V \leq 0.89$ for $2 \leq R_V \leq 4$ (Gontcharov et al., 2023). The average extinction of open clusters in the Galactic disc is $A_V = 0.70 \text{ mag kpc}^{-1}$ (Froebrich et al., 2010), but the extinction can be as low as $A_V = 0.37 \text{ mag kpc}^{-1}$ in diffuse regions (Wang et al., 2017) or higher in specific directions, for example $A_V = 1.45 \text{ mag kpc}^{-1}$ for open cluster King 7 (Straizys et al., 2021). We adopted an upper magnitude limit of $G = 18$ mag because fainter stars are unlikely to have reliable parallaxes. From the absolute magnitude equation $G = M_G + 5 \log d - 5 + A_G$, where d is distance in parsecs, we find that a B3 star has an apparent G -band magnitude of 9.8 mag at 1000 pc, 14.2 mag at 3000 pc, and 15.8 mag at 4000 pc. At the cooler end of our hot-star selection, an A2 main-sequence star with $T_{\text{eff}} = 8800$ K and absolute magnitude $M_G = 1.35$ mag would appear at G -band magnitudes of 12.3 mag at 1000 pc, 16.7 mag at 3000 pc, and 18.4 mag at 4000 pc. Because the hotter end of the temperature range contains fewer stars, this method is generally able to detect stellar populations out to distances of 3000–4000 pc.

3.3. Kinematic distances from the Galactic H I map

To independently verify the group-based distances derived in Sect. 3.2, we compared the stellar radial velocities of our targets with the kinematics of H I gas in the Milky Way. The H I gas traces the small- and large-scale structures in the

³ http://www.pas.rochester.edu/~emamajek/EEM_dwarf_UBVIJHK_colors_Teff.txt

Galaxy (McClure-Griffiths et al., 2023, and references therein). When a star is affiliated with a cluster or an OB association, which generally move together with the Galactic rotation and the surrounding interstellar medium (e.g. Castro-Ginard et al., 2021), its group-based distance should be consistent with the distance inferred from the kinematics of the surrounding H I gas. The radial velocities of supergiants and stars younger than 10^8 yr are correlated with the H I gas velocity (Fletcher, 1963; Humphreys, 1970).

We used the spatially coherent 3D kinematic map of the H I gas in the Milky Way by Söding et al. (2025), based on 21 cm emission measurements from the HI4PI survey (Bekhti et al., 2016). The format of the map was the Hierarchical Equal Area isoLatitude Pixelation of a sphere (HEALPix). It includes eight posterior samples for each point in the Sun-centred HEALPix-times-distance grid. We used the auxiliary fields data product by Söding et al. (2024), which includes the three components of the Galactic velocity field in each grid point. The velocity field was heliocentric and corrected for the peculiar motion of the Sun. The bin size increased from ~ 30 pc at a distance of 2000 pc to a distance of ~ 100 pc at 5000 pc.

For each star in our sample, we extracted the line-of-sight radial velocity of the H I gas within a radius of ~ 0.5 deg and plotted its value as a function of distance. We compared these gas velocity profiles with the stellar systemic radial velocity to determine the distance at which the two values were equal. We used systemic radial velocities from monitoring studies or mean radial velocities and variability amplitudes from *Gaia* DR3, where the former were not available. The adopted stellar radial velocities are listed in App. E of the Paper I. The radial velocity variability of YHGs makes it difficult to determine accurate systemic velocities, and the gas velocity map provides accuracy at scales of hundreds of parsecs (Söding et al., 2025). Therefore, the resulting distances have uncertainties of ~ 500 pc. The gas velocity profiles and v_{rad} for three YHGs are shown in Fig. 3.2.

HR 5171. The radial velocity of HR 5171 has been extensively monitored, with mean values of -40 km s $^{-1}$ (Humphreys et al., 1971) and -38 km s $^{-1}$ with a variability amplitude of 3.5 km s $^{-1}$ (Balona, 1982). This velocity corresponds to H I gas at a distance of 3500 pc, similar to the group-based distance of 2953^{+92}_{-96} pc within errors. The H I-based distance is also consistent with the established distance of 3600 pc (Chesneau et al., 2014; Humphreys et al., 1971) and with the distance from the *Gaia* parallax of 3601^{+649}_{-539} pc (Bailer-Jones et al., 2021), and it does not support the 1500 ± 500 pc distance suggested by van Genderen et al. (2019). For HR 5171, a more distant distance solution at ~ 6000 pc is also possible. Such a distance ambiguity is possible for objects located in the inner Galaxy inside the solar orbit (Nakanishi & Sofue, 2003). In these cases, the alternative solution is generally very small (< 1000 pc) or very large (> 5000 pc) and unlikely for most targets. We do not list them in Table 1. Our results confirm the distance of HR 5171 at 2900–3500 pc.

IRC +10420. The radial velocity measured from emission lines in IRC +10420 is between 60 and 68 km s $^{-1}$ (Humphreys et al., 2002; Klochkova et al., 1997),

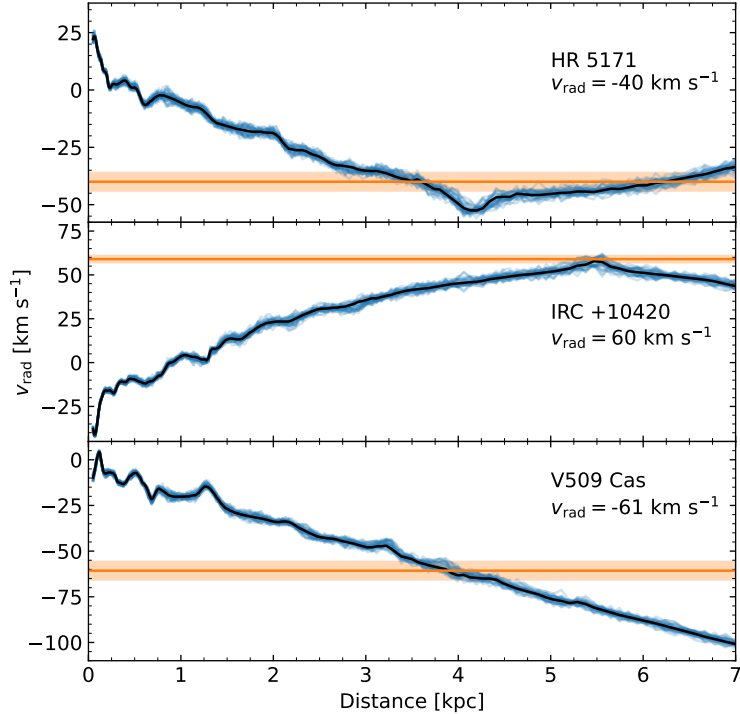


Figure 3.2: Radial velocity of H I gas along the lines of sight towards three YHGs. The thin blue lines show the sampled posterior velocity distribution of H I at each distance bin within a 0.5 deg region around each star. The solid black line indicates the mean velocity. The horizontal orange lines mark the observed stellar radial velocity, and the shaded region shows the approximate variability amplitude. Figure adapted from Paper I.

consistent with the result of CO rotational lines in local standard of rest (LSR) $v_{\text{LSR}} 75 \text{ km s}^{-1}$ (LSR correction $\sim 16 \text{ km s}^{-1}$; Oudmaijer 1998). This velocity suggests a very large distance of 5500 pc. We were unable to constrain a group-based distance. The large distance is consistent with earlier estimates of 5800 pc (Nedoluha & Bowers, 1992) and 4000–6000 pc (Jones et al., 1993) derived from Galactic rotation models. Our result is ~ 1000 pc greater than the distance derived from the *Gaia* parallax (4260^{+878}_{-752} pc). We adopted the *Gaia* distance for this star.

V509 Cas. The star has a systemic velocity of -60.7 km s^{-1} (Paper II), corresponding to a H I-based distance of ~ 3800 pc. This agrees with the group-based distance of 3368 ± 127 pc within the errors. This result is significantly different from 1370 ± 480 pc based on the parallax measured by the *Hipparcos* satellite and commonly used for this star (Nieuwenhuijzen et al., 2012; van Genderen et al., 2019), but in good agreement with a distance of 3917^{+969}_{-737} pc based on its *Gaia* parallax (Bailer-Jones et al., 2021). Thus, we adopted the group-based distance.

3.4. Comparison of distance results

Figure 3.3 compares our group-based distances for the YHG or YSG sample with those listed in the Bailer-Jones et al. (2021) catalogue. We used the RGEO values from that catalogue, as the RPGE0 distances that consider the photometric colour indices are unlikely to reliably characterise supergiants. For stars with relatively small parallax errors, our results agree well with the Bailer-Jones et al. (2021) catalogue values. We found significant differences for stars that have very large parallax errors, where the Bailer-Jones et al. (2021) distances tend to be very large, above 4000 pc. We found that they are likely much closer, because we identified possible affiliations with clusters or OB associations at distances of 2000–3000 pc.

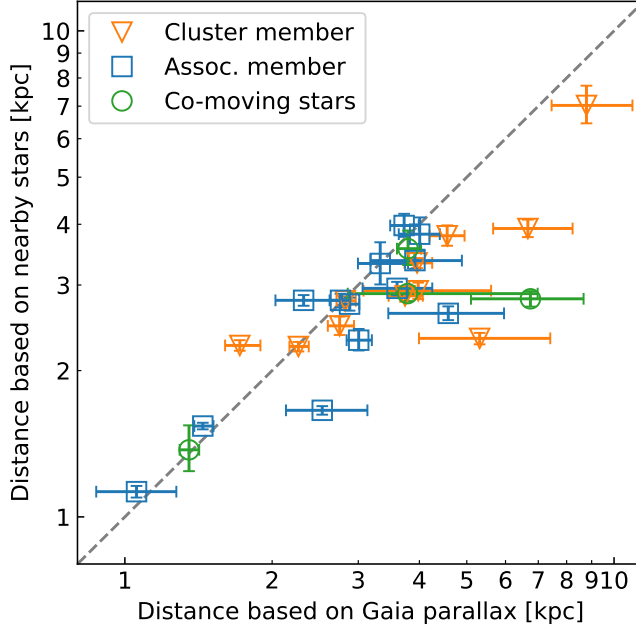


Figure 3.3: Comparison of group-based distances derived in this work with distances derived from *Gaia* parallaxes by Bailer-Jones et al. (2021). Stars associated with clusters, OB association, and stars without an origin group are marked with different symbols and colours. The dashed grey line marks the one-to-one relation. Both axes are logarithmic. Figure adapted from Paper I.

Overall, we improved the distance estimates for 28 stars out of the 35 stars in our sample. Eleven of these 28 stars are cluster members, 13 are in OB associations, and 4 stars do not belong to a stellar group, but we found a co-moving population. For the remaining 7 stars, we were unable to determine a group-based distance. IRAS 17163-3907, HD 179821, IRC +10420, V870 Sco, and IRAS 14394-6059 have co-moving stars spanning distances from 1000 pc to 4000 pc, but no clearly identifiable origin group. Most of these stars are also too distant or too reddened for this method. The final two stars, [FMR2006] 15 and IRAS 18357-0604, belong to a distant (~ 6000 pc) stellar population rich in RSGs. We were unable to obtain group-based distances for them because of their large distance and high extinction.

We derived H I-based distances for 32 stars, 6 of which lack a group-based distance estimate due to a large distance and high extinction. For 3 stars, no systemic radial velocities were available. One target, IRAS 14394-6059, lacks both types of distance estimates, but the *Gaia* parallax places the star beyond 5000 pc, making it a potentially luminous YSG. Six stars have only H I-based distances. These are: IRC +10420, HD 179821, IRAS 17163-3907, [FMR2006] 15, IRAS 18357-0604, and V870 Sco. In general, the H I-based distances agree with the distances derived from the Galactic rotation in previous studies.

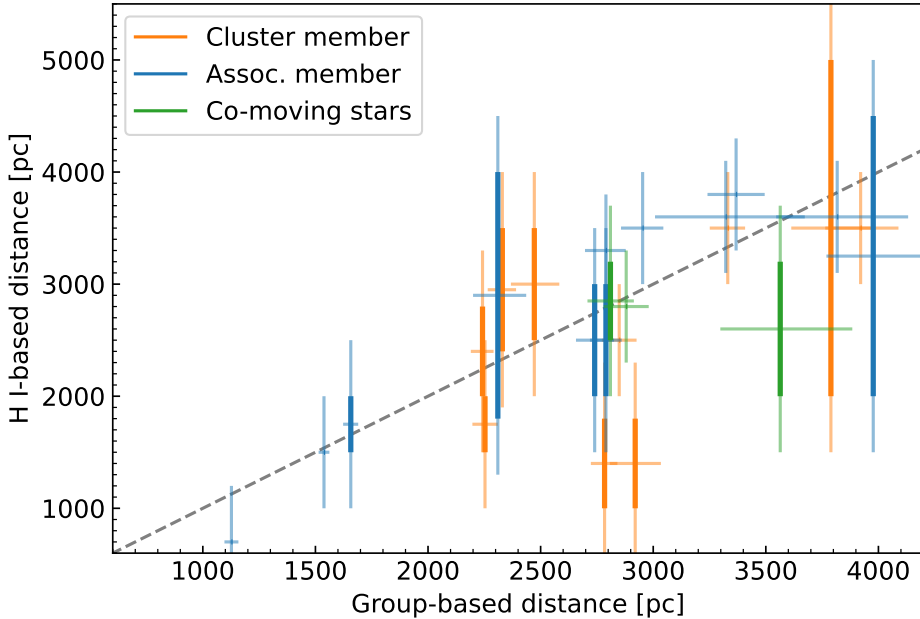


Figure 3.4: Comparison of group-based and H I-based distances. The solid lines indicate the H I-based distance ranges, and the lighter lines illustrate the uncertainties. Affiliations with stellar groups are indicated with different colours as in Fig. 3.3. The dashed grey line marks the one-to-one relation. Figure adapted from Paper I.

Generally, the results of H I-based distances coincide well with the group-based distances within uncertainties of about 500 pc (see Fig. 3.4). For the group-based distances, the uncertainties are about 100 pc for most stars. Group-based distances are most reliable when a proper motion alignment with a cluster or OB association can be established. Otherwise, there remains a higher probability that stars with similar proper motions do not represent the birth environment. Coincidental proper motion alignment between a YHG or YSG and an unrelated OB association or open cluster at a different distance is possible. This problem becomes more severe towards the Galactic centre, where multiple stellar populations lie along the same line of sight, complicating the identification of a possible origin population and preventing reliable distance determination for several stars. Differences between the H I-based and group-based distances can indicate an incorrect origin group

association or help identify potential runaway stars. Of the 26 stars that have both distance estimates, 23 stars have good agreement between the results. For three stars (ϕ Cas, HD 10494, and HD 96918), we found significant discrepancies that we detail below.

Table 1: Distances of YSGs and YHG. The targets are ordered by increasing right ascension. ‘Stellar group’ indicates that the star is not associated with any known cluster or OB association, but a co-moving group of nearby stars is identified.

Identifier	Ident. cluster ⁽¹⁾ /assoc. ⁽²⁾	Distance <i>Gaia</i> ⁽³⁾ (pc)	H I distance (pc)	Group dis- tance (pc)
ϕ Cas	NGC 457	3978^{+1627}_{-903}	1000-1800	2920^{+114}_{-113}
HD 10494	NGC 654 Assoc. 150	2823^{+142}_{-114}	1000-1800	2784^{+57}_{-61}
HD 12399	–	3792^{+240}_{-192}	2000-3200	3564^{+320}_{-266}
HD 18391	SAI 25 Assoc. 143	2263^{+113}_{-93}	2000-2800	2242^{+49}_{-52}
ϵ Aur	Assoc. 147	1056^{+218}_{-182}	~700	1127 ± 31
HD 57118	Assoc. 25	2759^{+116}_{-138}	~3300	2790^{+88}_{-93}
R Pup	NGC 2439 Assoc. 68	3958^{+291}_{-228}	~3500	3331^{+77}_{-80}
HD 74180	Assoc. 107	2532^{+600}_{-397}	1500-2000	1657^{+33}_{-34}
HD 75276	Assoc. 106	1443^{+74}_{-57}	~1500	1538 ± 24
V709 Car	Stellar group	4006^{+397}_{-376}	~3600	3817^{+315}_{-271}
TYC 8958-479-1	Assoc. 8	8783^{+2122}_{-1330}	-	7025^{+687}_{-572}
HD 96918	Assoc. 210/211	4583^{+1376}_{-1127}	500/5000	2623^{+88}_{-83}
o^1 Cen	–	3783^{+3197}_{-928}	~2800	2880 ± 100
V810 Cen	Stock 14 Assoc. 205	5312^{+2095}_{-1319}	2400-3500	2330^{+61}_{-65}
HR 5171A	SFR	3601^{+649}_{-539}	~3500	2953^{+92}_{-96}
UCAC2 4867478	Stellar group	3327^{+465}_{-331}	~3600	3322^{+351}_{-314}
IRAS 14394-6059	–	5450^{+770}_{-686}	-	-
CD-59 5594	Pismis 21 Assoc. 47	3739^{+325}_{-279}	~2500	2849 ± 77
HD 144812	–	1352^{+66}_{-58}	-	1374^{+169}_{-132}
V870 Sco	–	3945^{+940}_{-642}	~3500	-

Table 1: Continued.

Identifier	Ident. cluster ⁽¹⁾ /assoc. ⁽²⁾	Distance <i>Gaia</i> ⁽³⁾ (pc)	H I distance (pc)	Group dis- tance (pc)
V915 Sco	HSC 2870 Assoc. 82	1717 ⁺¹⁷⁵ ₋₁₁₅	1500-2000	2253 ⁺⁵⁷ ₋₅₆
IRAS 17163-3907	–	5196 ⁺¹⁴⁰¹ ₋₁₀₃₂	~1000	-
V925 Sco	Assoc. 82	3006 ⁺¹⁹² ₋₁₆₆	1800-4000	2310 ⁺¹²⁶ ₋₁₁₀
[FMR2006] 15	RSG group ⁽⁴⁾	3654 ⁺¹⁷⁴³ ₋₁₇₅₀	~6500	-
IRAS 18357-0604	RSG assoc. ⁽⁵⁾	4539 ⁺¹⁹³⁹ ₋₁₆₅₅	~5500	-
HD 179821	–	4432 ⁺³⁴⁹ ₋₃₅₅	>5000	-
V1452 Aql	CWNU 1591 ⁽⁶⁾	2748 ⁺¹⁹³ ₋₁₄₈	2500-3500	2472 ⁺¹¹¹ ₋₁₀₄
IRC+10420	–	4260 ⁺⁸⁷⁸ ₋₇₅₂	~5500	-
V1027 Cyg	Assoc. 15	3723 ⁺²⁶⁵ ₋₂₃₇	2000-4500	3977 ⁺²²⁶ ₋₂₀₈
HD 331777	Kronberger 54 Assoc. 15	4559 ⁺³⁸⁸ ₋₃₆₃	2000-5000	3789 ⁺¹⁹⁰ ₋₁₇₆
RW Cep	Berkeley 94 Assoc. 122	6666 ⁺¹⁵⁶¹ ₋₁₀₀₆	~3500	3921 ⁺¹⁶⁸ ₋₁₅₇
V509 Cas	Assoc. 120	3917 ⁺⁹⁶⁹ ₋₇₃₇	~3800	3368 ± 127
6 Cas	Assoc. 141	2319 ⁺⁴⁶³ ₋₂₈₈	2000-3000	2790 ⁺⁷⁰ ₋₇₁
HD 223767	Assoc. 141	2879 ⁺¹³⁶ ₋₁₁₇	2000-3000	2740 ⁺⁸⁶ ₋₈₃
ρ Cas	–	6747 ⁺¹⁹¹⁸ ₋₁₆₄₇	2500-3200	2810 ⁺¹⁰⁴ ₋₁₀₂

References: ⁽¹⁾ Hunt & Reffert (2024); ⁽²⁾ Chemel et al. (2022); ⁽³⁾ Bailer-Jones et al. (2021); ⁽⁴⁾ Davies et al. (2008); ⁽⁵⁾ Clark et al. (2014); ⁽⁶⁾ He et al. (2023).

3.5. Radius and luminosity

Based on our distance estimates, we determined the radii and luminosities for 15 YSGs and five YHG in our sample. In this analysis, we only included stars with available homogeneous angular diameter measurements and adopted literature T_{eff} values. For stars with multiple published T_{eff} values, we adopted an average temperature, and for stars without spectroscopic temperature estimates, we adopted the temperature closest to their spectral type classification. Due to the inhomogeneous data and discrepancies resulting from different methods, we estimated typical temperature uncertainties of at least 200 K. For stars with multiple published T_{eff} measurements, we adopted uncertainties to encompass the range of published values.

To estimate the stellar radii, we used the limb-darkened angular diameter values from the JMMC Stellar Diameter Catalog (JSDC; Bourges et al. 2017; Bourgés

et al. 2014; Chelli et al. 2016). Twenty of the 35 stars in our sample are included in the JSDC catalogue, providing a homogeneous set of angular diameters based on optical and near-infrared colour indices. Of these, 19 have group-based distance values. HD 179821 does not have a group-based distance, but has a relatively good *Gaia* parallax and distance from Bailer-Jones et al. (2021). Using these distances, we calculated the stellar radii ($R/R_{\odot} = 0.1075 \theta d$, where θ is the angular diameter in milliarcseconds and d is the distance in parsecs). The results are listed in Table 2.

For V509 Cas, the JSDC lists an angular diameter of 1.57 ± 0.12 mas, while the diameter measured by van Belle et al. (2009) is smaller by about 20%, 1.24 ± 0.03 mas. The calculated radii are $567 \pm 111 R_{\odot}$ and $449 \pm 20 R_{\odot}$, respectively. The latter value is similar to $\sim 400 R_{\odot}$ found by Nieuwenhuijzen et al. (2012).

For ρ Cas, the JSDC angular diameter is 2.16 ± 0.19 mas, while Anugu et al. (2024a) determined an angular limb-darkened diameter of 2.09 ± 0.02 mas from near-infrared interferometry. At our group-based distance, the resulting radii are $633 \pm 62 R_{\odot}$ and $609 \pm 27 R_{\odot}$, respectively. van Genderen et al. (2025) determined the radius of ρ Cas from its pulsational cycle and found a quiescent radius of $\sim 400 R_{\odot}$ and an outburst radius of $> 700 R_{\odot}$ at a distance of 2500 pc ($\sim 450 R_{\odot}$ and $\sim 780 R_{\odot}$ at our group-based distance of 2800 pc). Since the last outburst in 2013, ρ Cas has been quiescent (van Genderen et al., 2025). There is a considerable discrepancy between the radii derived from interferometric and pulsational studies.

The heterogeneous interferometric studies available for a small number of YSGs and YHG do not allow us to consistently quantify any systematic offset between the JSDC-inferred angular diameters and those obtained from interferometric measurements. However, comparison with literature values obtained through different methods suggests that the JSDC angular diameters for V509 Cas and ρ Cas are likely overestimated. The JSDC empirical relations between angular diameters and photometric indices for luminosity classes I, II, and III are primarily calibrated on K- and M-type giants, with very few hotter stars included (Chelli et al., 2016). For luminous supergiants in advanced evolutionary states, these relations may not apply. In addition, the colours of YHGs are intrinsically variable (van Genderen et al., 2019), which may contribute to the uncertainty in determining diameters from photometric indices. With limited and heterogeneous interferometric measurements available, we cannot establish systematic offsets between angular diameters from the JSDC and those obtained from interferometric measurements. Homogeneously derived angular diameters from the spectral energy distribution or interferometric modelling are required to obtain self-consistent radii for the sample stars.

We estimated the stellar luminosities using the Stefan-Boltzmann law.

$$L = 4\pi R^2 \sigma T_{\text{eff}}^4, \quad (3.8)$$

The resulting luminosities are listed in Table 2. The luminosities of YSGs and YHGs are shown in Fig. 3.5. For V509 Cas and ρ Cas, we used the radii from Nieuwenhuijzen et al. (2012) and van Genderen et al. (2025) instead of the JSDC values to avoid overestimated angular diameters. No angular diameters are listed

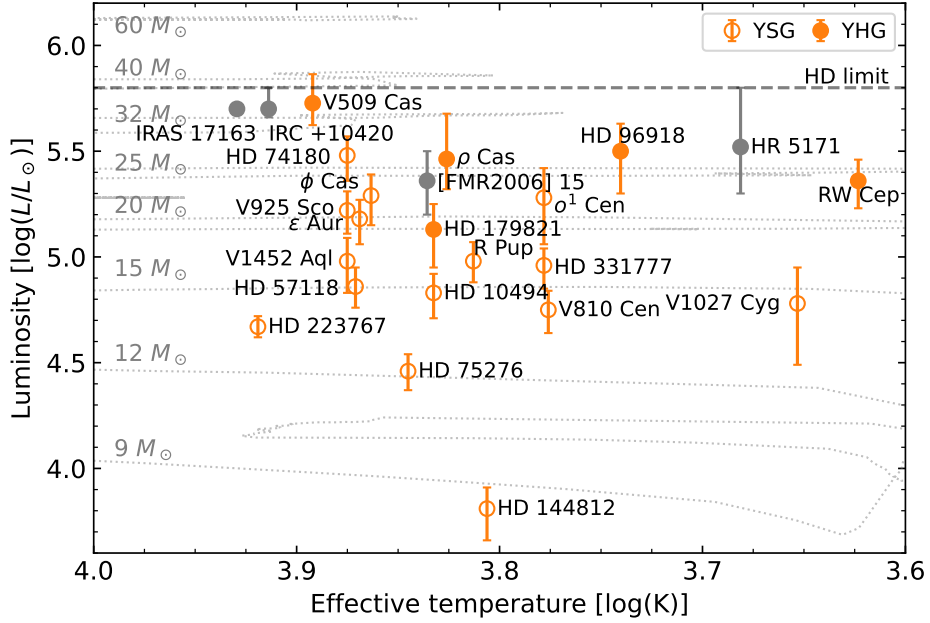


Figure 3.5: Yellow hypergiants and YSGs on the HR diagram. YHGs are shown as filled yellow circles, and YSGs and candidate YHGs are shown as empty yellow circles. Literature values for four YHGs are shown as grey circles. The HD luminosity limit (Humphreys, 1978) is marked with a dashed line. Solar metallicity evolutionary tracks (Ekström et al., 2012) are shown as dotted light grey lines. Figure adapted from Paper I.

in the JDSC for IRC +10420, IRAS 17163-3907, [FMR2006] 15, and HR 5171, but we adopted their luminosities from the literature for reference. Three stars lie near the Humphreys-Davidson (HD) luminosity limit: IRC +10420, IRAS 17163-3907, and V509 Cas. The YSGs occupy a wider range of luminosities, with the most luminous YSGs partially overlapping with the less luminous YHGs. The luminosities of three YHGs, HD 179821, RW Cep, and HD 96918, agree well with previous studies. Significant deviations are found for V509 Cas and ρ Cas, where using the angular diameters from JDSC results in unexpectedly large radii and unreasonably high luminosities ($\log L/L_{\odot} > 5.8$), although the large radius for ρ Cas is supported by an interferometric study (Anugu et al., 2024a). The calculated luminosities for YSGs agree very well in general with literature values. We only found a discrepancy for V810 Cen, where the previous luminosity estimate of $\log L/L_{\odot} = 5.3$ (Kienzle et al., 1998) is much higher than our value of $\log L/L_{\odot} = 4.74^{+0.09}_{-0.11}$ due to a revised distance that is lower by ~ 1000 pc.

Table 2: Derived radii and luminosities for the sample stars. For V509 Cas and ρ Cas we give the radius and luminosity values for both angular diameters: (JDSC) using the angular diameter from Bourges et al. (2017) and (interf.) using interferometric studies of van Belle et al. (2009) and Anugu et al. (2024a).

Identifier	Radius (R_{\odot})	Luminosity ($\log L/L_{\odot}$)
ϕ Cas	276 ± 29	$5.25^{+0.11}_{-0.13}$
HD 10494	187 ± 15	$4.83^{+0.09}_{-0.12}$
ϵ Aur	236 ± 25	$5.13^{+0.09}_{-0.12}$
HD 57118	163 ± 15	$4.86^{+0.09}_{-0.10}$
R Pup	245 ± 22	$4.98^{+0.09}_{-0.1}$
HD 74180	325 ± 28	$5.5^{+0.09}_{-0.11}$
HD 75276	116 ± 9	$4.38^{+0.07}_{-0.09}$
HD 96918	616 ± 69	$5.5^{+0.13}_{-0.2}$
σ^1 Cen	403 ± 41	$5.33^{+0.15}_{-0.21}$
V810 Cen	222 ± 20	$4.74^{+0.09}_{-0.11}$
HD 144812	65 ± 8	$3.81^{+0.10}_{-0.15}$
V925 Sco	242 ± 25	$5.22^{+0.09}_{-0.11}$
HD 179821	264 ± 22	$5.13^{+0.12}_{-0.18}$
V1452 Aql	182 ± 18	$4.98^{+0.11}_{-0.15}$
V1027 Cyg	403 ± 37	$4.78^{+0.17}_{-0.29}$
HD 331777	278 ± 23	$4.96^{+0.08}_{-0.11}$
RW Cep	902 ± 82	$5.36^{+0.10}_{-0.13}$
V509 Cas	567 ± 111 (JDSC)	$6.03^{+0.15}_{-0.23}$ (JDSC)
	449 ± 20 (interf.)	$5.83^{+0.05}_{-0.06}$ (interf.)
HD 223767	108 ± 4	$4.7^{+0.05}_{-0.06}$
ρ Cas	653 ± 63 (JDSC)	$5.86^{+0.13}_{-0.19}$ (JDSC)
	628 ± 24 (interf.)	$5.83^{+0.12}_{-0.16}$ (interf.)

3.6. Discussion

3.6.1. Spatial distribution

Following discussions of the spatial distribution and possible isolation of LBVs and supergiants with the B[e] phenomenon (e.g. Aadland et al., 2018; Deman & Oey, 2024; Martin et al., 2025; Smith & Tombleson, 2015, and references therein), van Genderen et al. (2019) proposed that the YHGs ρ Cas, V509 Cas, HR 5171, and HD 179821 are isolated objects. This might be evidence of an evolutionary connection with LBVs. An explanation for the potential isolation of LBVs is their origin through binary evolution: either merger products or mass gainers in Roche-

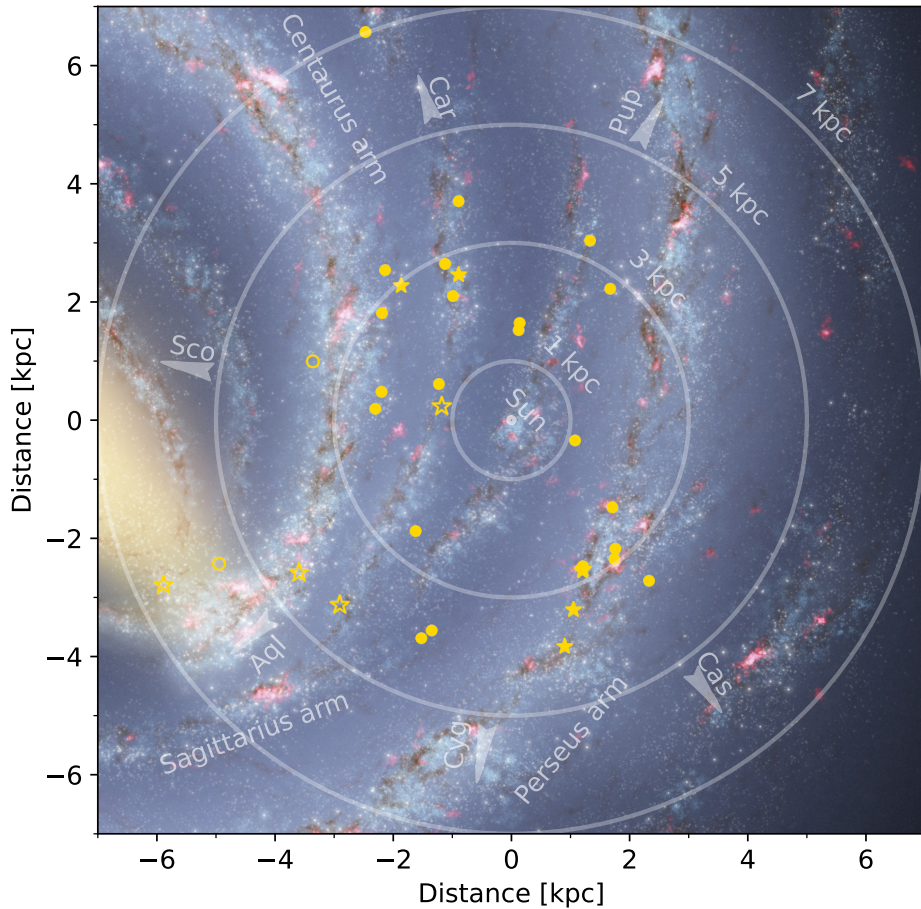


Figure 3.6: Family portrait. Illustration of the Milky Way⁴ showing the distribution of YSGs (circles) and YHG (stars). Objects with group-based distances are marked with filled markers, and objects with distances based on H I or Bailer-Jones et al. (2021) are marked with empty markers. Figure adapted from Paper I.

lobe overflow systems that were kicked out of their original populations after the companion exploded as a stripped-envelope supernova (Smith & Tombleson, 2015).

Figure 3.6 shows the locations of our sample stars projected on a schematic view of the Milky Way. We used the group-based distances where available, and otherwise, the H I-based or Bailer-Jones et al. (2021) distances. The stars broadly trace the spiral arms of the Galaxy. Our results indicate that YHGs are located in heterogeneous environments. Two YHGs are likely cluster members, three are in OB associations, and one is in a star-forming region. Four YHGs may not be affiliated to stellar groups, but two of them are too far away for us to draw a clear conclusion.

⁴ NASA/JPL-Caltech/R. Hurt (SSC/Caltech)

In contrast, a majority of the YSGs in our sample are associated with stellar groups. The kinematic properties of 20 out of 25 YSGs are consistent with membership in open clusters or OB associations. For 5 stars, no clear origin group could be found. In two of these cases, V870 Sco and IRAS 14394-6059, the stars are distant and have high extinction. For the other three stars, HD 12399, α^1 Cen, and HD 144812, we can identify co-moving stars at a similar distance.

Overall, we found that most YSGs are members of young stellar populations. This is consistent with YSGs being younger pre-RSG objects and still affiliated to their birth environments. The environments of the YHGs are more diverse, and for almost half of them, their origin populations remain unclear. This might be the result of different evolutionary histories. If this is the case, there may be multiple ways for a star to become a YHG, and the distance from their birth environments may be a result of binary interactions.

The number of luminous YSGs found in the Large Magellanic Cloud (Martin & Humphreys, 2023) is more than double the size of our sample and could provide more insight into their surrounding environments. Improved astrometry and distances of Galactic YSGs and YHGs will be provided by the *Gaia* DR4 release⁵, which will include epoch astrometry for all sources.

3.6.2. Runaway stars

About 25–30% of the Galactic O-type stars are runaway stars, and about a quarter of them show bow shocks generated from the interaction between their stellar winds and the interstellar medium (Carretero-Castrillo et al., 2025, 2023). Studies in the Small Magellanic Cloud (SMC) suggested that about 65% of the OB-type field stars are runaways, mainly due to dynamical ejections from clusters (Dorigo Jones et al., 2020, and references therein). Since OB stars are the progenitors of YHGs or YSGs, some stars in our sample might have experienced an ejection event. The YHGs in our sample without a clear group affiliation have variable stellar winds and have undergone major mass-loss events (e.g. Jura & Werner, 1999; Koumpia et al., 2020; Lobel et al., 2003a; Oudmaijer, 1998), setting ideal conditions for bow shock formation in a runaway scenario. However, we found no evidence of a bow shock associated with any YHG or YSG in our sample, neither in the literature nor in our examination of Wide-Field Infrared Survey Explorer (WISE; Wright et al. 2010) images.

For stars whose H I-based and group-based distance estimates agree well, a runaway scenario is unlikely, as dynamical perturbations would affect the proper motion, radial velocity, or both, leading to inconsistent distances. An exception is HD 96918, whose proper motion agrees with OB associations no. 210/211 (Chemel et al., 2022), yielding a group distance of 2623^{+88}_{-83} pc, but the H I-based distance is ~ 500 pc or ~ 5000 pc. This discrepancy was already identified by Achmad et al. (1992), whose distance estimates of 2400 ± 900 pc and ~ 2200 pc from independent

⁵ <https://www.cosmos.esa.int/web/gaia/dr4>

methods agree well with our group-based distance. If HD 96918 were a runaway, an apparent alignment with an OB association based on similar proper motion would be unlikely to provide a reliable distance. If HD 96918 has been dynamically perturbed, its radial velocity could deviate from the H I velocity, but the effect has not been significant enough to separate it from the stars in the OB association.

Small offsets in proper motions ($> 2\sigma$ of the cluster mean) are observed for several cluster members: ϕ Cas, HD 18391, and RW Cep have minor proper motion offsets compared to other members of their clusters. HD 223767 has a projected on-sky offset of < 0.1 deg of the open cluster King 12 and shares a similar distance of ~ 2800 pc, but its proper motion differs from that of cluster members by more than 3σ . HD 74180 lies near the open clusters Pismis 6 and Pismis 8, both at distances of ~ 1700 pc and separated by ~ 0.3 deg on sky, with proper motion differences of ~ 0.5 mas yr $^{-1}$. These clusters may originate from the same molecular cloud (Fitzgerald et al., 1979). A proper motion difference of 0.5 mas yr $^{-1}$ corresponds to a velocity difference of ~ 5 km s $^{-1}$ at a distance of 2000 pc and ~ 7 km s $^{-1}$ at 3000 pc, indicating small kinematical differences originating from modest dynamical interactions. Overall, while we found minor kinematic offsets for several stars, we found no clear evidence of runaway YHGs or YSGs in our sample.

3.6.3. Comments on binarity

The binary fraction for YSGs is not well constrained. Recently, a multiplicity study in the SMC suggested that supergiants of spectral classes B, A, and F were either born as effectively single stars or are products of binary mergers (Patrick et al., 2025). For AF-type supergiants in the SMC, the binary fraction was estimated to be smaller than 15% (Patrick et al., 2025). However, O’Grady et al. (2024) estimated the binary fraction of YSGs in the Magellanic Clouds at 20–60%. For reference, O-type stars in the Milky Way have a binary fraction of ~ 70 –90% (Sana et al., 2012, 2014), and the observed binary fraction for RSGs in the SMC and Large Magellanic Cloud (LMC) is ~ 15 –30% (Dai et al., 2025; Dorda & Patrick, 2021; Neugent et al., 2020; Patrick et al., 2019, 2020).

We summarise that a majority of the well-studied YHGs are likely to have binary companions: HR 5171 is a double or triple system, where one companion might be interacting with the hypergiant (Chesneau et al., 2014). 6 Cas is an A+O-type supergiant binary (Maíz Apellániz et al., 2021a). V509 Cas has a likely B-type companion (Lobel et al., 2013). IRAS 17163-3907 has been suggested to have a binary companion (Wallström et al., 2017). ρ Cas, IRC +10420, and [FMR2006] 15 have RUWE values higher than 1.22, which is the threshold commonly used as an indicator for unresolved binarity (Castro-Ginard et al., 2024). Only HD 179821 appears to be single, as it is unlikely to have a companion more massive than $5 M_{\odot}$ and a spectral class earlier than B5 (Jura & Werner, 1999). Less information is available for the YSGs, but some confirmed cases of binarity include ϵ Aur, which

is an eclipsing binary (Stefanik et al., 2010); HD 144812, which is an interacting binary (Kourniotis et al., 2025); V915 Sco, which has a Wolf-Rayet companion (Andrews, 1977); V810 Cen, which is a spectroscopic binary (Kienzle et al., 1998); ϕ Cas and HD 57118, which have been identified as binaries (Burki & Mayor, 1983); and HD 96918, HD 74180, and IRAS 18357-0604, which have high RUWE values.

Overall, about 50% of the YHGs and YSGs in our sample show direct or indirect signs of binarity, with a firm lower limit of 22% (eight confirmed binary systems). We selected our sample based on luminosity estimates in the literature and did not consider any binarity indicators. Nevertheless, these factors are correlated through the contribution of a hot companion to the overall luminosity of the system, which might introduce a bias towards identifying binaries.

3.7. Summary of results

We provided a homogeneous and consistent determination of distances for Galactic YSGs and YHGs. Because the *Gaia* parallaxes contain uncertainties, we explored an indirect method of determining the distance through membership identification with nearby stellar groups, that is, clusters or OB associations. We compared the proper motions of YHGs and YSGs with those of clusters (Hunt & Reffert, 2024) and OB associations (Chemel et al., 2022; Mel’nik & Dambis, 2017) in the surrounding sky region. Using the more reliable parallaxes of co-moving stars, we calculated group-based distances. We validated this method against the large-scale Galactic kinematics by comparing the stellar systemic radial velocities with the Galactic HI velocity map (Söding et al., 2025). Our HI-based distances agree well with previous studies, where distances were derived from comparison with the Galactic rotation curve. The two independent methods agree well for most of the targets.

We determined membership in a cluster or OB association for 20 YSGs. Five YSGs remain without a clearly identified stellar group, and two of them are likely too distant and reddened for the method. The stellar environments of YHGs are more varied:

- Stellar cluster: RW Cep and [FMR2006] 15.
- OB association: 6 Cas, V509 Cas, and HD 96918.
- Star-forming region: HR 5171.
- Unaffiliated: ρ Cas, IRAS 17163-3907, IRC +10420, and HD 179821.

We derived luminosities for 15 YSGs and five YHGs by combining our distance estimates with T_{eff} values from the literature and angular diameters from the JSDC catalogue. Our results agree well in general with previous luminosity estimates.

4. V509 CAS – 25 YEARS OF STABILITY IN THE ‘YELLOW VOID’

This Chapter is based on Paper II: *Yellow hypergiant V509 Cas: Stable in the ‘yellow void’*.

A. Kasikov, I. Kolka, A. Aret, T. Eenmäe, and V. Checha, 2024, A&A 686, A270.

V509 Cas is a representative member of the YHGs and has experienced multiple large-scale shell ejections. Smolinski et al. (1989) described three episodes of mass ejections: in 1970, 1979, and 1982, though the last two have also been treated as a single episode (Nieuwenhuijzen & de Jager, 2000). An extensive study of the yellow hypergiant V509 Cas has been conducted by Nieuwenhuijzen et al. (2012), providing a comprehensive overview of various physical parameters of the star, including temperature, luminosity, colour indices, and $\log g$ values. They place V509 Cas at the high temperature border of the first instability region of the YEV and hypothesise that the star’s approach to this region has increased its atmospheric stability. However, upon crossing over to the second area of instability, the atmosphere may become unstable again, leading to severe mass loss.

4.1. History of variability

During the 20th century, the brightness of V509 Cas gradually increased from around 5.36 mag in the beginning of the 1940s to 4.6 mag by 1976 (Zsoldos, 1986). Since the mass-loss episodes in late-1970s, the brightness has returned to previous levels and the star has become ~ 0.5 mag bluer (Fig. 2.7; Percy & Zsoldos, 1992).

V509 Cas exhibits quasi-periodic variability that is composed of several periods with varying lengths. The lengths and amplitudes of the periods change over time (Nieuwenhuijzen & de Jager, 2000; Percy & Zsoldos, 1992; Sheffer & Lambert, 1987; Zsoldos, 1986). From mid-1900s to the beginning of 2000s the periods decreased from 200–400 days to 100–150 days, and amplitudes from 0.1–0.2 mag to 0.05–0.1 mag, likely related to the increase in the star’s T_{eff} (van Genderen et al., 2019).

In the early 1900s, the star had a G0–G3 spectrum (W. S. Adams et al., 1935; Cannon & Pickering, 1993), corresponding to $T_{\text{eff}}=5100\text{--}5600$ K. Over the course of the 20th century, the temperature of V509 Cas varied by several thousand degrees. Figure 4.1 illustrates T_{eff} values from Nieuwenhuijzen & de Jager (2000), Nieuwenhuijzen et al. (2012), and the current study. In 1969 the T_{eff} ranged from 5250 K to 5630 K and during the outburst in 1973, it decreased to 4900 K (Nieuwenhuijzen & de Jager, 2000). This is attributed to the formation of a cooler pseudo-photosphere from the out-flowing matter. As this pseudo-photosphere dispersed, the T_{eff} increased. A similar pattern was observed during the second mass-loss event in 1979–1982. Over a span of 30 years, the star appeared to ‘bounce’ twice against the border of the yellow void (de Jager, 1998). There is

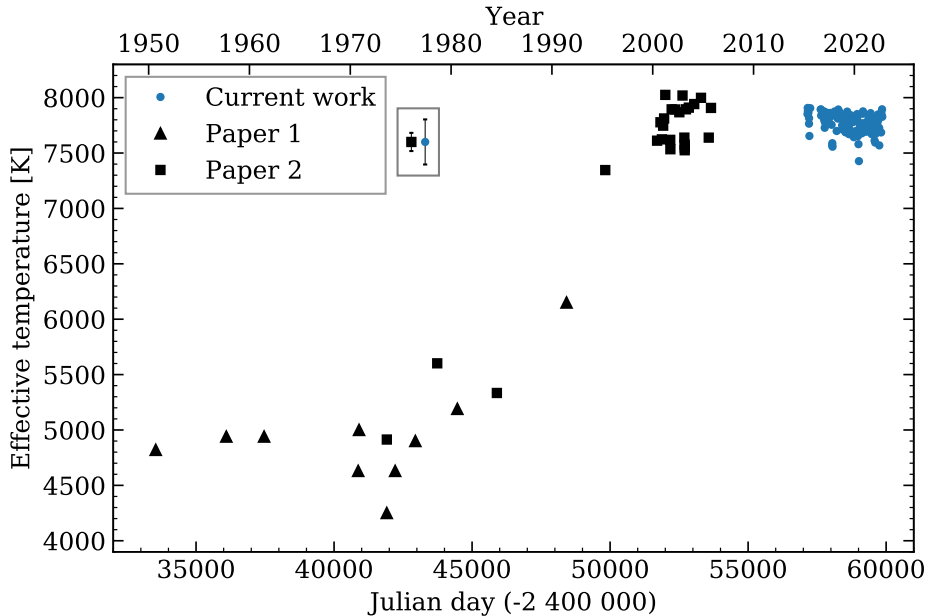


Figure 4.1: Variability of T_{eff} of V509 Cas over the last 70 years, including data from Nieuwenhuijzen & de Jager (2000, Paper 1) and Nieuwenhuijzen et al. (2012, Paper 2). The uncertainties for Nieuwenhuijzen et al. (2012) data near the beginning of 2000s are 60–80 K (sample error bar size is shown in the box), while the uncertainties for earlier data are 72 K in 1973, 120 K in 1978, and 240 K in 1984. For Nieuwenhuijzen & de Jager (2000), the uncertainties for all points were not given. Figure adapted from Paper II.

no indication of distant nebulosity around V509 Cas, suggesting that if the star is a post-RSG, it has only recently (within the last 500–1000 years) entered the instability region (Schuster et al., 2006).

After these mass-loss events, the temperature of V509 Cas continued to rise from 4570 K in 1980 (Nieuwenhuijzen & de Jager, 2000; Piteris et al., 1988) to 7170 K in 1995 (Nieuwenhuijzen & de Jager, 2000), and reached higher-than-ever values at 7900 ± 200 K in 1998 (Israelian et al., 1999). Since then, the rate of temperature increase seems to have slowed. In the early 21st century, T_{eff} has remained close to 8000 K (Aret et al., 2017c; Nieuwenhuijzen et al., 2012; Yamamuro et al., 2007), exhibiting short-term variability of up to a few hundred degrees (Nieuwenhuijzen et al., 2012).

Variations in the radial velocity (v_{rad}) of V509 Cas are predominantly caused by the star’s pulsation cycle (de Jager, 1998). These variations may also reflect the passage of shockwaves through the photosphere (Lambert et al., 1981). Based on observations on 5 epochs between 1921 and 1923, the v_{rad} values ranged from -56.2 to -68.2 km s $^{-1}$, with a total amplitude of 12 km s $^{-1}$ and an average of -60.2 km s $^{-1}$ (Harper, 1923). We have no measurements from the intermediate period until 1976, when during the mass-loss episode Lambert and Luck reported the v_{rad} of ionised lines at -35 km s $^{-1}$, and of neutral metallic lines -40 km s $^{-1}$.

They also noted asymmetrical trailing blue wings in spectral line profiles. By mid-1977, the v_{rad} had shifted to $\sim 60\text{--}65 \text{ km s}^{-1}$, and the profiles became almost symmetrical (Humphreys, 1978; Lambert & Luck, 1978). Since then, the v_{rad} has remained at a similar level with a $\sim 9\text{--}19 \text{ km s}^{-1}$ amplitude (Klochkova, 2019; Lambert et al., 1981; Sheffer & Lambert, 1987).

4.2. Observations and methods

4.2.1. Photometry

AAVSO international database. The majority of photometric data are obtained from the American Association of Variable Star Observers (AAVSO) international database. We use observations from three observers who have carried out the longest time series or have transformed their data to Johnson-Cousins photometric system: W. Vollmann (AAVSO observer code VOL, observations in V -filter (Vollmann, 2023)), M. Sblewski (SMAI, observations in B filter (Sblewski, 2023)) and E. Van Ballegoij (BVE, observations in B -filter (van Ballegoij, 2023)). The observations are summarised in Table 3.

Table 3: Observations from the AAVSO international database. The observation type refers to the used photometric measurement device, where DSLR means the digital single lens reflex camera, CCD is a CCD camera and PEP refers to measurements done with a single-channel photometer using a photodiode. The asterisk marks observations that have not been transformed to the standard Johnson-Cousins system.

Observer	Code	Filters	Obs. type	Data points
Vollmann	VOL	V	DSLR	445
Sblewski	SMAI	B^*	CCD	141
van Ballegoij	BVE	B	PEP	54

Observations from AAVSO Bright Star Monitor. The recent photometric variability of V509 Cas is captured by observations of AAVSO Bright Star Monitor (BSM) program proposal #115 (PI: T. Eenmäe). We used Johnson-Cousins B - and V -filter observations from two observatories: New Hampshire Henden (NH2) and New Mexico Stein (NM). Both sites utilise Takahashi E180 7" reflectors with ASI183MM CMOS-cameras and a selection of photometric filters. Photometric monitoring using BSM started in September 2019 to support TESS observations in sectors 16 and 17, and has continued until present time.

The photometric observations from AAVSO BSM programme have been optimised for measuring bright stars. Nevertheless, the data are still affected by the scintillation effect. To mitigate these scintillation effects when using short exposures, several individual measured data frames are averaged. To better estimate the differential magnitude of the variable star, we used the combined comparison star method. The combined comparison star is composed of the summed flux of three

stars in the field of view: HD 218010, HD 240170 and HD 217127. The first two are included in the list of AAVSO comparison stars and the constant magnitude of the third comparison star has been confirmed by measurements done by the Hipparcos mission (1σ scatter of measurements was ± 0.012 mag (ESA, 1997)).

We obtained pre-processed frames from the BSM programme and measured the magnitudes of the stars using aperture photometry with programme Aperture Photometry Tool (APT, Laher et al. (2012)). The aperture size was selected to be $3 \times$ FWHM of the target. We determined the differential magnitude of V509 Cas either from the average frame of a night (provided by the AAVSO BSM pipeline) or from many individual frames taken during the same night, the results of which were then averaged. Therefore, one point on the graph represents the luminosity of the star in one night. The number of averaged frames and their exposure times are shown in Table 4.

Table 4: Observations with the AAVSO BSM telescopes, filters, the number of frames taken in each filter per night, and the exposure times of each individual frame are given.

Filter	Nr of frames	Exposure	# nights
<i>B</i>	8..10	1.5 s	272
<i>V</i>	15..20	0.75 s	265

The results slightly vary depending on the weather conditions (airmass, transparency of the atmosphere, etc.) and scintillation. The typical root-mean-square (RMS) value is around 3% for both V509 Cas and the combined comparison star. We left out nights on which the conditions were highly unstable and the RMS value was found to be higher than 6%. The resulting differential magnitude of the star (average per night) has the uncertainty 0.01...0.02 mag.

TESS. V509 Cas was observed with the TESS satellite in sectors 16, 17, 24, and 57. The observations were performed at the following dates: 50 days in September–November 2019, 30 days in April–May 2020 and 29 days in October 2022. Although TESS does not provide luminosity measurements in the *V*-filter, these observations show the brightness variability of the star with very good cadence and precision. We measured the differential TESS magnitude of V509 Cas against the comparison star HD 217127, both of them imaged on the same TESS camera and CCD. In the selection of proper apertures and in the correction of the light curve systematics, we have been guided by the papers by Handberg et al. (2021) and Lund et al. (2021). The resulting magnitudes have a precision better than ± 0.005 mag. Therefore, we have used this data to qualitatively describe the variability of V509 Cas and to complement the *V*-filter observations from AAVSO.

Gaia. We are using data from the Gaia Data Release 3 (Gaia Collaboration et al., 2016, 2023). Photometric observations were done between 25th July 2014 and 28th May 2017, spanning a period of 34 months. Gaia has measured the brightness of V509 Cas in three filters: *G*, *G_{BP}*, and *G_{RP}*. We converted those observations to

the Johnson-Cousins system V filter brightnesses, using the colour transformation equations given in the Gaia Data Release 3 Documentation version 1.3 on the Gaia webpage¹. Gaia’s brightness measurements have small errors (<0.001 mag for G_{BP} and G_{RP} , 0.02 mag for G -filter). The more significant errors in the Gaia data come from the conversion of Gaia’s filters to the Johnson-Cousins V -filter magnitude; the standard deviation of the colour transformation equation is 0.03 mag.

4.2.2. Smoothing photometric observations

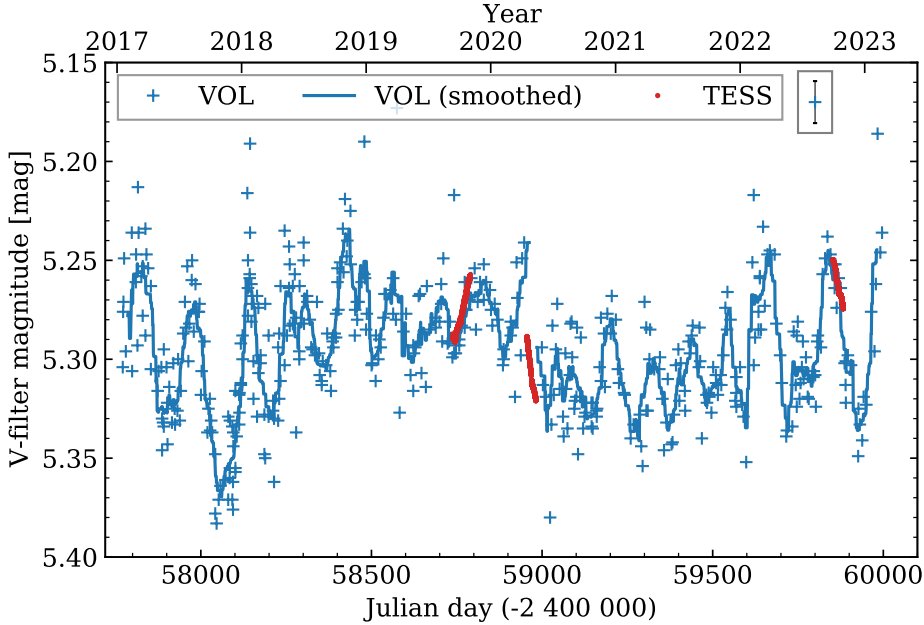


Figure 4.2: Smoothing of AAVSO data taken by observer Vollmann (VOL). Shifted brightness observations from TESS (red dots) follow the smoothed curve. The mean residual of the smoothing is 0.013 mag. The mean error of observations is 0.01 mag. Figure adapted from Paper II.

The V -filter observations by AAVSO (W. Vollmann) span the time period from 2017 to 2023, and they are typically conducted more frequently than once in a fortnight, with a minor gap in early 2020 (see Fig. 4.2). Typical uncertainties of these observations average around 0.01 mag. The brightness fluctuates without obvious regularities in the range of 5.4 to 5.2 mag. A smoothing procedure is advantageous for presenting this variability more clearly. Given the frequent sampling, we applied a straightforward 30-day weighted running mean, assigning less weight to points with higher uncertainties. Smoothing of V -filter observation data is justified by smooth brightness variability evident in the TESS light curve. While TESS did not measure brightness in the V -filter, our smoothed light curve

¹ https://gea.esac.esa.int/archive/documentation/GDR3/Data_processing/chap_cu5pho/cu5pho_sec_photSystem/cu5pho_ssec_photRelations.html

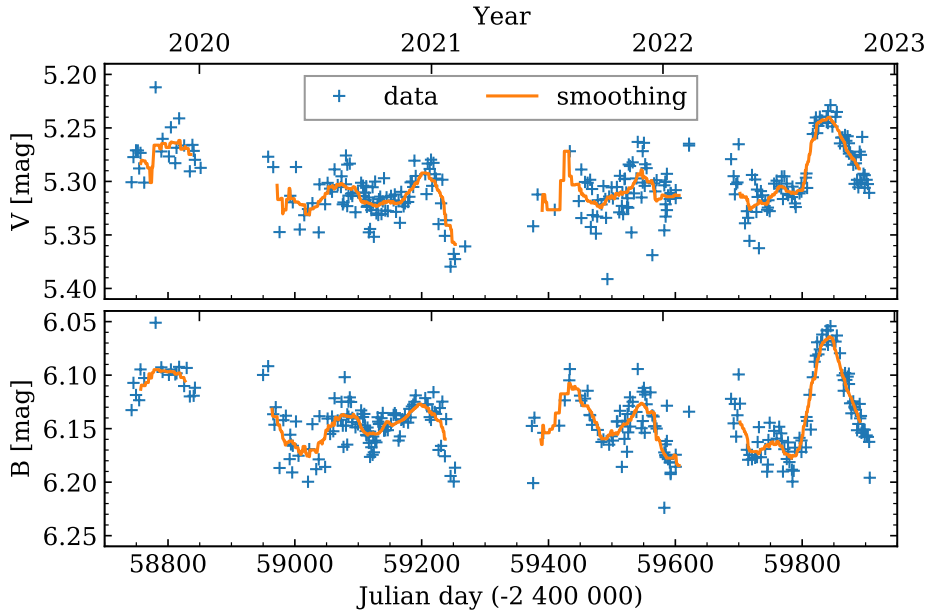


Figure 4.3: Smoothing of BSM V - and B -filter data. The mean residual of the V -filter fit is 0.012 and the B -filter fit is 0.010. The uncertainty of each point is around 0.01..0.02 mag. Figure adapted from Paper II.

effectively tracks the variability behaviour observed in TESS measurements. In Fig. 4.2, we added an arbitrary vertical shift to TESS measurements to achieve the best alignment with AAVSO data, only to illustrate the smoothness of variability.

We applied the same smoothing method to BSM B - and V -filter observations – a running mean with a 30-day window (Fig. 4.3). The BSM magnitudes have been measured with reference to the standard stars (Sect. 4.2.1) obtaining differential magnitudes that have not been transformed to the Johnson-Cousins standard magnitude scale. To align the observations with data provided by AAVSO observers, we shifted them by an empirical constant, which minimised the difference between two sets of data. The BSM observations show similar variability behaviour to the observations from AAVSO. We have also included observations from Gaia (Sect. 4.2.1) to extend the time span covered by the light curve (see Fig. 4.5).

4.2.3. Spectroscopy

Tartu Observatory. V509 Cas was observed using the Tartu Observatory (TO) 1.5-m telescope AZT-12 (Folsom et al., 2022) during the period from 2015 to 2021, in total on 103 nights, fairly evenly distributed across the years. We used the long-slit spectrograph ASP-32 in Cassegrain focus with 1800 lines mm^{-1} diffraction grating providing spectra in the wavelength range from 6300 Å to 6730 Å with a signal-to-noise ratio (S/N) ~ 200 –300 and resolution $R \sim 10000$.

The data were reduced using the IRAF²(Tody, 1986) software, in which `noao`, `imred`, `ccdred`, and `ctioslit` packages for image and long-slit spectral reductions were used. Bias and flat corrections were applied to the spectra. Dark correction was not necessary due to the sufficient cooling of the CCD. For the wavelength calibration, comparison spectra of ThAr hollow cathode lamp were taken before and after target exposure. In addition, the wavelengths of the diffuse interstellar band (DIB) at $\lambda 6379.01$ and some telluric lines near 6400 \AA were used to check and refine the accuracy of the wavelength calibration. The heliocentric correction was applied to the spectra. The spectra were continuum normalised by fitting a cubic spline of the 20th order. Flux calibration was not attempted. The full list of observations can be found in the App. B of Paper II.

Nordic Optical Telescope. In addition to the observations at the TO, in 2021 and 2022 for a period of 14 months, V509 Cas was observed at the 2.56 m Nordic Optical Telescope (NOT) using the FIES echelle spectrograph (instrument description: Telting et al. (2014)) in medium-resolution mode ($R = 45\,000$) and high-resolution mode ($R = 60\,000$) (proposal ID 65-410, PI A. Kasikov). We also include an earlier observation in 2015 in high-resolution mode ($R = 60\,000$). The spectra cover the wavelength range from 3630 \AA to 8980 \AA without gaps. Our observations were carried out with an approximately monthly interval, in total on 16 nights (listed in App. B of Paper II) and were reduced with FIEStool (Stempels & Telting, 2017) standard pipeline.

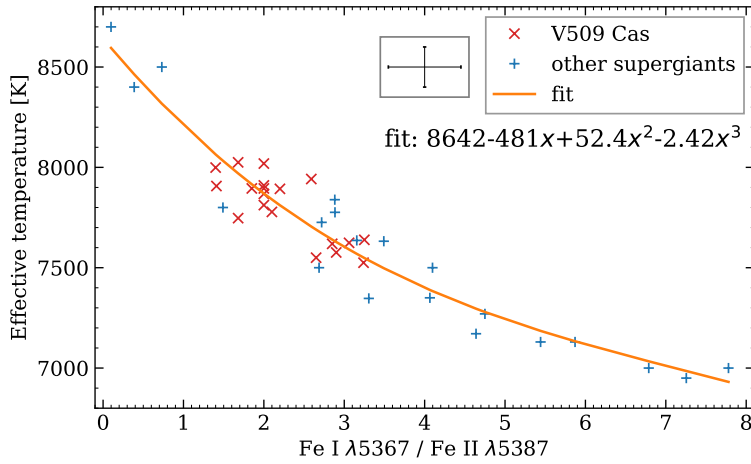
4.2.4. Temperature determination

We determine the T_{eff} spectroscopically using line depth ratios (LDR) of temperature sensitive lines (Gray, 1994; Gray & Johanson, 1991). The LDR method has been used successfully for FGK supergiants (Kovtyukh, 2007), for ρ Cas (Kraus et al., 2019), and for YSGs in the Magellanic Clouds (Kourniotis et al., 2022). The last two papers stressed the necessity of using specific pairs of spectral lines.

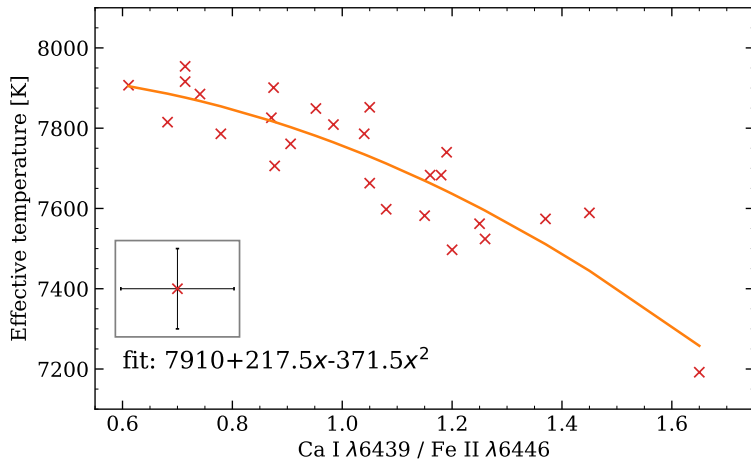
In the case of V509 Cas, the selection of lines for LDR is limited by circumstellar (CS) emission components that first appeared in the spectrum in the 1970s (e.g. Lambert & Luck, 1978). This was first seen in spectral lines of neutral atoms, but now is also present in ionised ones. Other constraints of the LDR method include abundance effects, which can be overcome by using line pairs of the same chemical element. Furthermore, the $\text{LDR} \sim T_{\text{eff}}$ relation depends on the surface gravity and the metallicity of the calibrators (e.g. Fukue et al., 2015; Matsunaga et al., 2021). Taking these limitations into account, we relied on Fe I and Fe II lines. By visual inspection of the spectra we noticed that Fe I lines with $E_{\text{low}} \gtrsim 4.0 \text{ eV}$ and Fe II lines with $E_{\text{low}} > \sim 5.0 \text{ eV}$ have no clearly distinguishable emission components and are very minimally or not at all influenced by CS emission.

We selected Fe I $\lambda 5367.47$ ($E_{\text{low}} = 4.42 \text{ eV}$) and Fe II $\lambda 5387.06$ ($E_{\text{low}} = 10.52 \text{ eV}$) absorption lines. These lines are measurable in the spectra used by

² <https://iraf-community.github.io/>



(a) Temperature fit of V509 Cas and additional calibration stars based on Fe I λ 5367.47 and Fe II λ 5387.06 lines.



(b) Effective temperatures of V509 Cas and the corresponding Ca I λ 6439.08 / Fe II λ 6446.41 line depth ratio.

Figure 4.4: Effective temperature and line-depth-ratio calibration curves. Figures adapted from Paper II.

Nieuwenhuijzen et al. (2012) and also in the spectra of additional calibrators. As calibrators, we selected the SGs from the list presented by Kovtyukh (2007) in Table 4, and added a few more well-analysed SGs to cover the T_{eff} range 7000...8500 K. All calibrators are listed in App. A of Paper II, indicating the sources of their high resolution spectra and of their temperatures applied for cali-

bration. The obtained correlation between LDR and T_{eff} is depicted in Fig. 4.4a including its third order polynomial approximation.

The commonly used interval in TO data is $\sim 6300\text{--}6600 \text{ \AA}$, which does not include the selected lines. Using high resolution spectra of V509 Cas covering the entire optical region (listed in App. A of Paper II), we transformed the calibration to lines included in this region. In this region, there are several non-blended Fe I and Fe II lines which would be suitable for LDR calibration (e.g. Lambert & Luck (1978) indicate the sensitivity of lines Fe I $\lambda 6430.85$ and Fe II $\lambda 6432.68$ in the case of V509 Cas). However, these are affected by CS emission components. By visual inspection, we noticed that the depth of the Ca I $\lambda 6439.08$ line ($E_{\text{low}} = 2.53 \text{ eV}$) is remarkably variable while the depth of Fe II $\lambda 6446.41$ line ($E_{\text{low}} = 6.22 \text{ eV}$) changes much less. Both of these lines are free of distinguishable emission components. We obtained the relation demonstrated in Fig. 4.4b. We used the corresponding second order polynomial fit for calculating the T_{eff} . The values estimated using the correlative relationship(s) have formal errors up to 140 K.

4.3. Results

4.3.1. $B - V$ colour index

Since the late 1990s, the brightness of V509 Cas has stabilised. Between 2014 and 2023, it has consistently remained near 5.3 mag, displaying occasional short-term fluctuations with amplitudes up to 0.13 mag. Over the past two decades, the V -filter brightness variability has remained notably low, especially when compared to the rapid changes observed in the 20th century. In comparison to the Hipparcos measurements in the early 1990s (as reported by Nieuwenhuijzen & de Jager (2000)), the amplitudes of short-term variability have remained at a similar level.

The Hipparcos measurements showed a notable decrease in $(B - V)$ values (Nieuwenhuijzen et al., 2012), which has currently halted (Fig. 2.7 in Chapter 2). The $(B - V)$ colour of the star has remained stable over the last six years, averaging around 0.84 mag with minor short-term fluctuations in the range of 0.05–0.10 mag. van Genderen et al. (2019) showed that amplitude ratios $\text{Ampl } B / \text{Ampl } V$ and $\text{Ampl } V / \text{Ampl } (B - V)$ reveal temperature changes during pulsations, with higher values indicating unstable atmospheric conditions. These amplitude ratios are independent of interstellar reddening and extinction. For V509 Cas, the variability amplitudes in the V -filter and B -filter are very similar, with smaller amplitudes (0.05 mag) during some years alternating with slightly larger amplitudes (~ 0.10 mag) in the following few years (Fig. 4.3). Both amplitude ratios have small values near 1, which is indicative of a stabilising atmosphere.

4.3.2. Period analysis

We applied the Lomb-Scargle period analysis model to the AAVSO V -filter data. Most of the detected periods fall within the 100–200 day range. However, there also

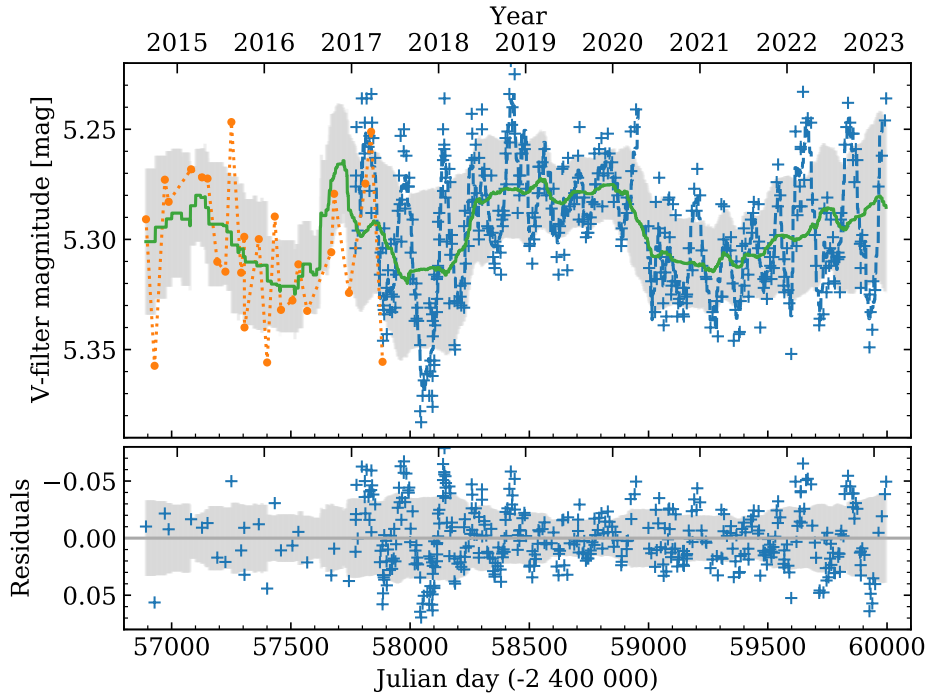
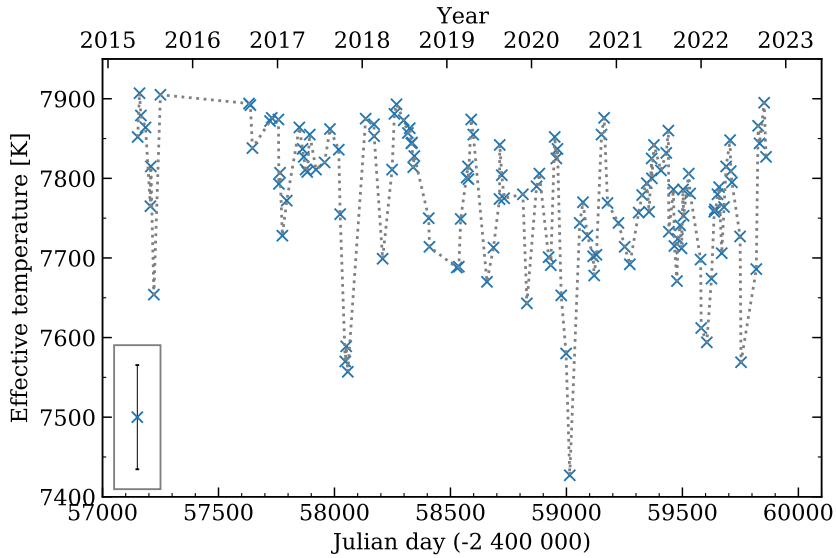


Figure 4.5: *V*-filter brightness from AAVSO Vollmann’s data (blue crosses) and Gaia data (orange dots). The solid green line shows a running mean of 300 days, and the light grey shading corresponds to the standard deviation of the running mean. In the lower figure we show the residuals of the mean level that illustrate the amplitudes of short-term fluctuations, which vary between 0.05–0.13 mag. Figure adapted from Paper II.

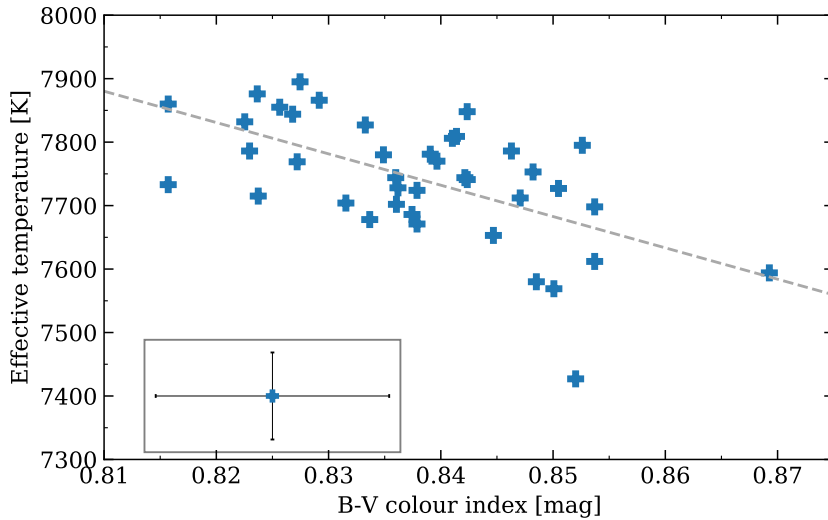
appears to be a much longer periodicity in the data, with a period of approximately 1300 days. Neither our analysis nor earlier studies have identified this extended periodicity in the light curve from 1970s–1990s by Percy & Zsoldos (1992). In Fig. 4.5, a 300-day running mean has been applied to the light curve, which smooths out short-term (< 300 days) variability fluctuations and highlights variability on longer timescales. There is no evident long-term trend of decreasing or increasing variability amplitudes or mean magnitude. The residuals in the lower panel of Fig. 4.5 illustrate the variability of short-term brightness fluctuation amplitudes, when the longer-term curve has been subtracted.

4.3.3. Effective temperature

Over the recent years, the temperature of V509 Cas has remained at a stable level around 7800 K, with the short-term fluctuations being on average less than 200 K (Fig. 4.6a). In the beginning of 2000s, the T_{eff} was 7500–8000 K (Nieuwenhuijzen et al., 2012). It appears that in the last 25 years, the temperature has settled slightly below 8000 K. Compared to the beginning of 2000s, there is also a decrease in the amplitude of temperature fluctuations, which may suggest the stabilisation of the star’s atmosphere.



(a) Effective temperatures based on spectra of V509 Cas. The error bar of the LDR measurements is shown in a box on the left.



(b) Effective temperature values based on spectra versus the $B - V$ colour index from BSM observations on the same epochs.

Figure 4.6: Effective temperature results. Figures adapted from Paper II.

In Fig. 4.6b, we show the relation between colour and temperature variations using our temperature values derived from spectroscopy and the smoothed $B - V$ colour index values. Even during the current 'calming down' phase of V509 Cas,

both the colour and the depth of spectral lines continue to adequately reflect the average effective temperature.

4.3.4. Radial velocity

To characterise the mean expansion and contraction of the stellar surface of V509 Cas, we measure the radial velocity using two relatively strong Si II absorption lines ($\lambda\lambda 6347, 6371$). These lines are expected to be formed over the full extended atmosphere of the star. The high excitation potential of Si II ($E_{\text{low}} = 8.12$ eV) suggests a contribution from deeper layers, while the significant line depth (up to 50% of the continuum level) indicates the contribution from outer layers. Additionally, there is absence of strongly blending lines and emission in the line wings, both of which could distort radial velocity measurements.

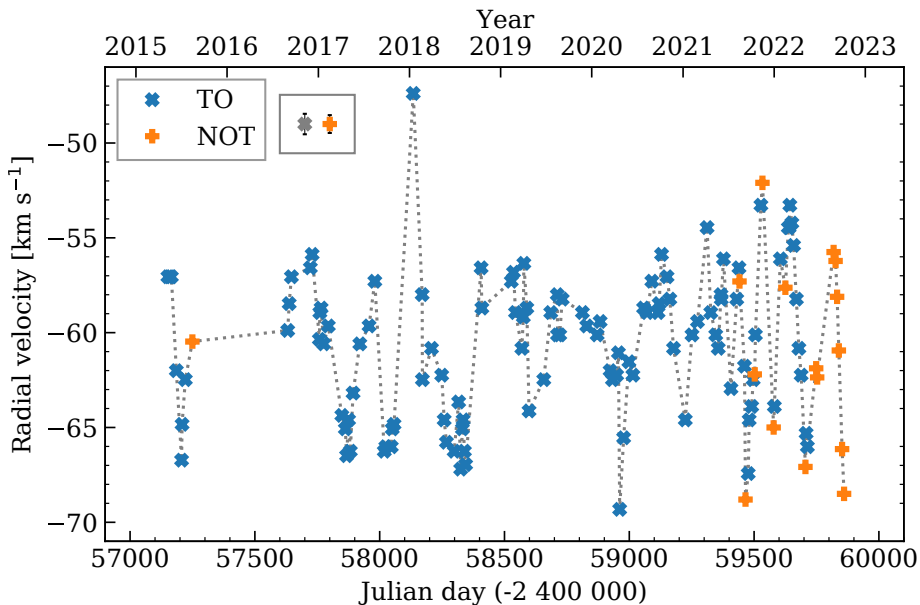


Figure 4.7: Radial velocity variability of V509 Cas. Our radial velocity measurements are based on TO and NOT spectra. Figure adapted from Paper II.

To improve the accuracy of our radial velocities derived from TO spectra, we performed an additional wavelength scale correction procedure. Using high-resolution FIES spectra with a precise wavelength scale, we determined the location of a nearby diffuse interstellar band (DIB) at 6379.00 ± 0.01 Å. This DIB served as a stable reference point, allowing us to calculate the offset value for each TO spectrum, typically of the order of a few hundredths of an angstrom.

We measured the central wavelength of Si II lines by fitting a Gaussian function to the central part of the line. Figure 4.7 shows the radial velocity time series. We assume that the systemic velocity is the average value of all measurements $v_{\text{sys}} = -60.7$ km s⁻¹. Any deviations from this average value indicate dynamics within the star’s atmosphere.

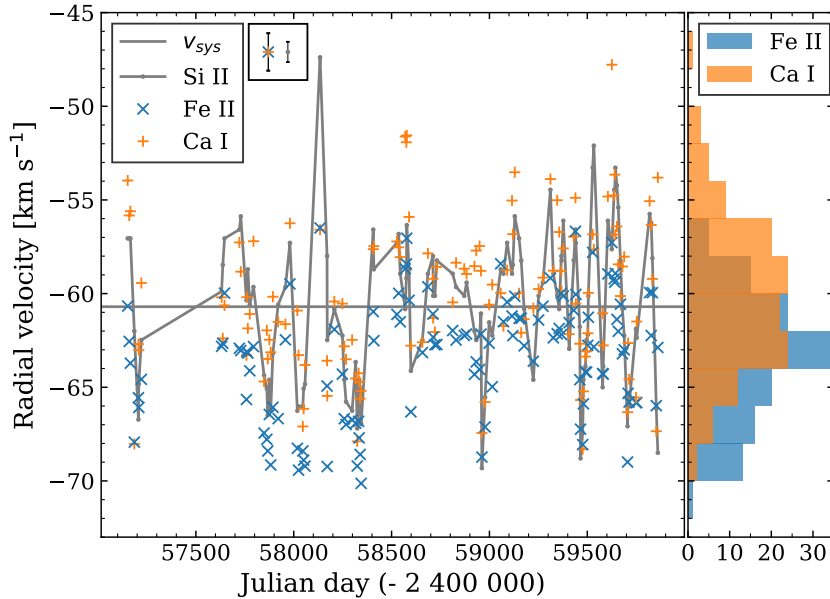


Figure 4.8: Centroid radial velocities of Si II, Ca I, and Fe II lines and their distribution histograms. The error bars for Ca I and Fe II (shown in the corner) are larger than the errors for radial velocities from the Si II line, because the Fe II and Ca I lines are much shallower and therefore the results are more affected by noise. Figure adapted from Paper II.

The radial velocity variability of metal lines has remained at the same level throughout the entire century, from the beginning 1900s (Harper, 1923), to the time of major eruptions in the 1970s. Meanwhile, the star’s temperature has increased by several thousand degrees and its brightness has changed by a magnitude. The similarity in the variability of radial velocity of V509 Cas could indicate that the star had been quasi(?) -periodically pulsating already before the activity in the 1970s. If that’s the case, then at the end of the mass-loss episodes the star simply restored its previous behaviour. In Chapter 2, Fig. 2.8 shows the combined 7-year T_{eff} , v_{rad} , and brightness variability curve.

Temperature sensitive lines. We investigated the radial velocities of the spectral lines used for our temperature determination (Ca I $\lambda 6439$ and Fe II $\lambda 6446$). Given that both of these lines are asymmetric and relatively weak in comparison to Si II lines, we could not use the same Gaussian fitting method. Instead, we calculated the centroid (‘centre of gravity’ of the spectral line) radial velocities. Fig. 4.8 shows the resulting velocity values and the histograms illustrating their distribution.

There is a strong correlation of approximately 0.81 between the radial velocities of Fe II and Ca I lines. The position of the Fe II line centroid oscillates on average at higher blueshift values (by roughly 3.2 km s^{-1}) than the Si II and Ca I. This may be due to the influence of a weak emission component formed in circumstellar material. Emission components are visible above the continuum level in many low-excitation lines, but the emission can affect all lines to a certain degree, depending

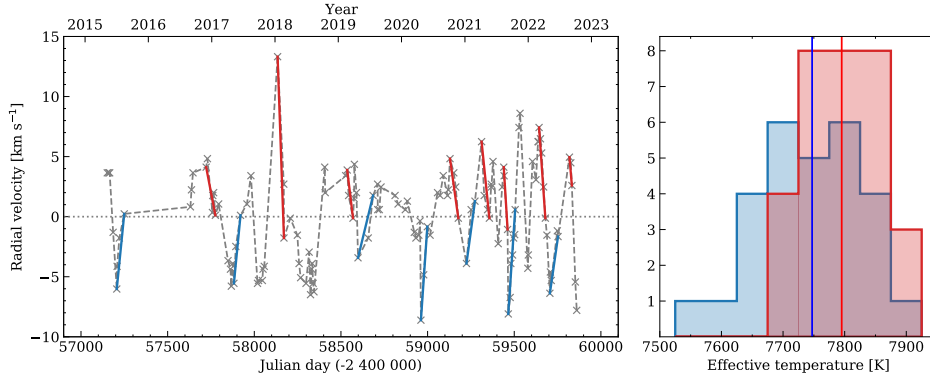


Figure 4.9: Pulsational behaviour of V509 Cas. Left: Radial velocity time series of Si II. As a zero or ‘equilibrium’ velocity, we have chosen the mean radial velocity of the star at -60.7 km s^{-1} (grey horizontal line). We have marked the epochs, when the star is at its contraction state (red) and when the star is in an expanding state (blue). We calculated the mean effective temperature for each state. Right: Histogram of mean effective temperatures. During the star’s expansion state, the temperatures are on average slightly lower than in the contraction states. Figure adapted from Paper II.

on excitation energy and abundance of the element (c.f. Sc II which is discussed in Sect. 4.3.5 and the Fe II $\lambda 7712$ line discussed previously in Kasikov et al., 2022). A very weak emission component is indistinguishable in the shape of the spectral line, but can cause the centroid to shift in velocity scale.

Effect of pulsations on the temperature. Radial velocity derived from the Si II lines could describe the radial component of pulsations of the star – the mean dynamics across the entire visible stellar surface. We aim to describe these movements as expansion and contraction phases of the atmosphere of V509 Cas and assess how the measured radial velocity correlates with the mean temperature level during each stage.

We identified distinct epochs within our radial velocity time series when the star exhibited either contraction (associated with higher radial velocity values) or expansion (associated with smaller radial velocity values). We assume that both of these states end near the mean (equilibrium) velocity value. We excluded potential velocity relaxation periods in which representative data was lacking or when the velocity exhibited only small-amplitude variability around the mean. On the left side of Fig. 4.9, we display these selected ‘expansion’ and ‘contraction’ epochs, marked in blue and red, respectively. We also assume that the ‘contraction’ and ‘expansion’ phases are best developed (and have the characteristic temperature) when the corresponding velocities already show the trend from the local maximum or minimum towards the equilibrium value (epochs of the velocity relaxation). We hypothesised that at the end of the contraction stage, the star should reach higher temperatures due to the compression of atmospheric layers, while at the end of the expansion phase, the temperature should decrease due to the drop in the internal energy (enhanced radiative cooling and work done by gas pressure).

The histogram on the right side of Fig. 4.9 shows the temperatures during these ‘expansion’ and ‘contraction’ epochs. We found that the mean effective temperature during the ‘contraction’ epochs was 7790 K and for the ‘expansion’ epochs 7740 K. The difference is in the order of magnitude of 1σ of the distribution. Both data sets contain temperatures near the overall mean temperature value at 7800 K. However, in the ‘expansion’ states, there is a higher representation of lower temperatures, while in the ‘contraction’ state, a number of higher temperatures are found. These findings support our hypothesis, although further observations with better temporal cadence over several pulsational periods would provide a clearer view.

4.3.5. Disc-like circumstellar structure

Notable features in the spectrum of V509 Cas are the presence of several forbidden lines ([Ca II], [N II], [O I]) as well as emission components in the wings of absorption lines from various elements (e.g. Fe II, Sc II). No large-scale nebulosity has been detected around V509 Cas (Schuster et al., 2003), thus the existence of these emission features calls for an alternative explanation. Similar features have been identified in the spectra of B[e] stars, and it has been suggested that [Ca II] and [O I] lines originate from the inner region of the Keplerian gaseous disc surrounding the stars (Aret et al., 2012; Kraus et al., 2010). In the case of V509 Cas, we observe that the [Ca II] line is double-peaked and remains invariable throughout our observed period (Fig. 4.11). Additionally, [O I] lines have been found in the spectrum, but unlike the [Ca II] lines, these lines are single-peaked and rotationally broadened (Aret et al., 2017c). The shape of the [Ca II] and [O I] line profiles in our observations implies that we are seeing an inclined rotating disc-like structure around the star. The usage of the word ‘disc’ in this context is rather broad, the structure would be most likely akin to a toroidal cloud in Keplerian motion surrounding the star, rather than a thin disc with clear edges.

Kasikov et al. (2022) demonstrated that the observed variability of the Fe II absorption lines with emissions in the wings can be explained by the superposition of absorption and emission components formed in different regions. The absorption component of Fe II line forms in the pulsating atmosphere and changes in sync with the Si II line. The double-peaked emission component originates from a circumstellar disc and is not influenced by the pulsations, similar to the [Ca II] lines. Consequently, in the resulting composite profile, the intensity of the emission components in the blue and red wings of the line is determined by the location and depth of the absorption component, while the emission component remains unchanged.

Similarly to some Fe II lines, the Sc II $\lambda 6604$ line has a central absorption component and two emission components on both sides of the central absorption at velocities of roughly $\pm 40 \text{ km s}^{-1}$. Sc II line has not received special attention in the literature, but Harmer et al., 1978 observed the spectrum of V509 Cas in the H α region, among other lines showing the Sc II line nearby. In 1975 and 1976, at

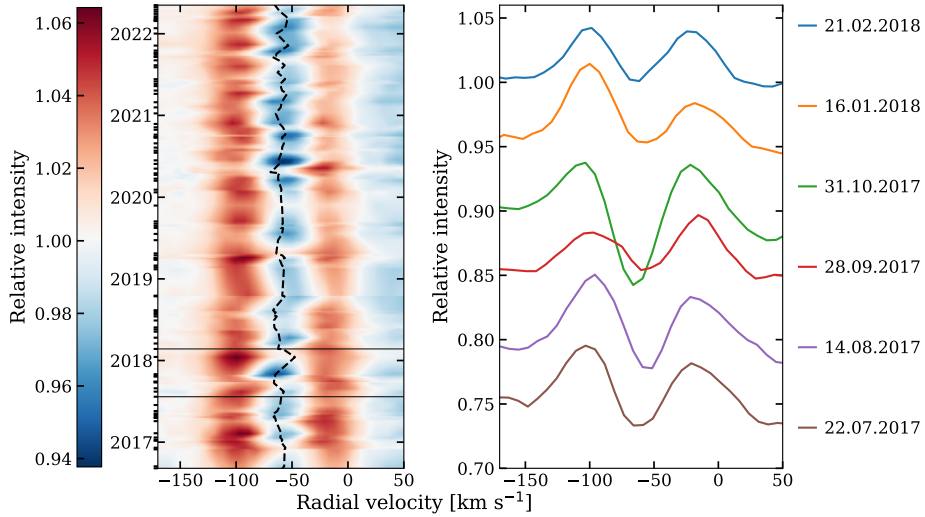


Figure 4.10: Variability of Sc II $\lambda 6604$ line over 6 years. Left: A dynamic spectrum of all TO spectra. White colour corresponds to the continuum level, blue colour indicates absorption and red colour is emission. Darker colour corresponds to stronger absorption or emission strength. Epochs of observations are marked with notches on the left, and gaps between observations have been filled using linear interpolation. The dashed black line shows radial velocity measured from Si II lines. The box indicates the period of observations seen on the right. Right: 6 individual observations in 2017 and 2018. The spectra have been shifted vertically by 0.05 mag between each epoch for clarity. The radial velocity scale on all plots is the same. Figure adapted from Paper II.

the time when the star underwent an episode of enhanced mass loss, the Sc II was an absorption line without any emission peaks.

In Fig. 4.10 (left) we have plotted a timeline spanning more than 6 years of Sc II line variability. The central absorption component is located at roughly -60 km s^{-1} . With a black dashed line, we have also plotted the radial velocity of the star based on the Si II line. The radial velocity of the Sc II absorption behaves synchronously with that of the Si II line. On the right, we have extracted 6 observation epochs to illustrate the variability of Sc II at different Si II radial velocity values. We can see changes in the relative intensity of emission components of Sc II. At some epochs the violet component is stronger and on others the red one is stronger. The shift occurs within a few weeks. The position of the central absorption determines the stronger component, as the absorption component ‘consumes’ either the violet or the red emission wing. There is a correlation between the radial velocity changes and the changes in the intensities of Sc II line emission components and it behaves similarly to the Fe II lines.

In Fig. 4.11, we show profiles of [Ca II], Sc II and Si II at two different epochs. There are two telluric absorption lines at the edges of [Ca II] line at approximate velocities -120 and 20 km s^{-1} , which have been removed through processing the spectra with a telluric standard star, these lines do not affect the emission peak of

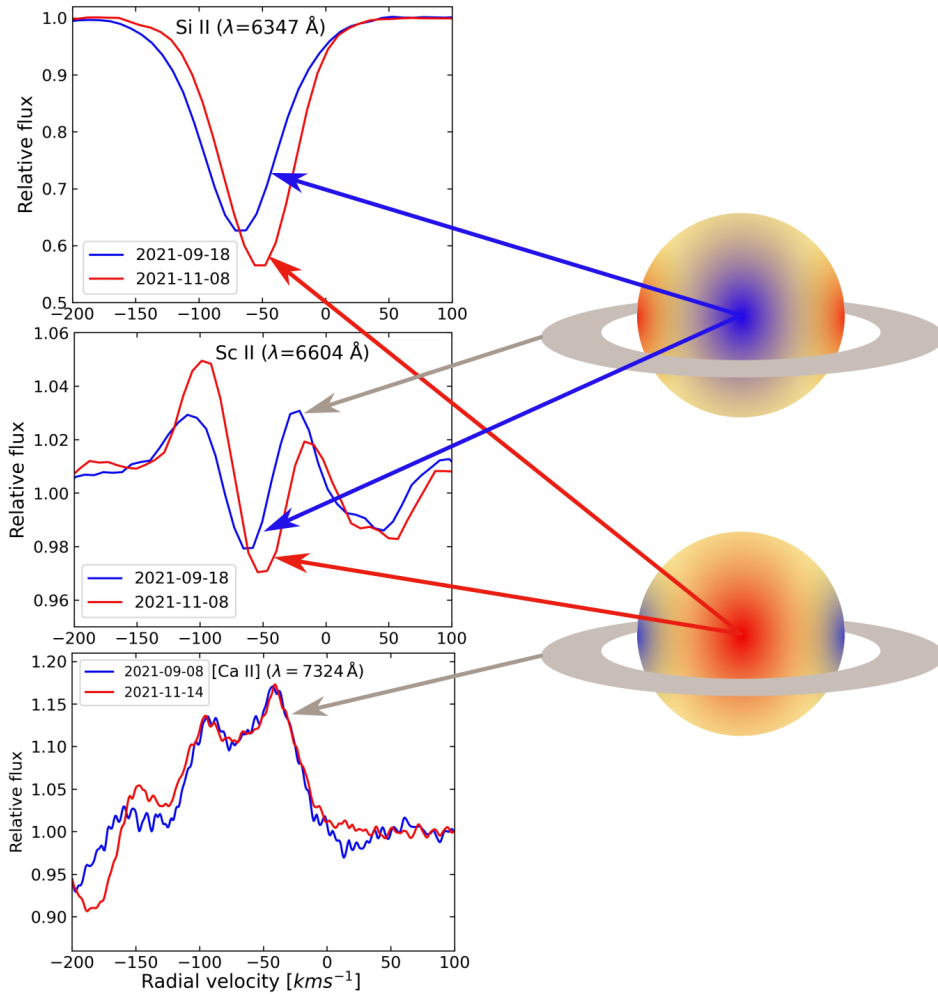


Figure 4.11: Illustrative drawing of the Si II, Sc II, and [Ca II] lines and where the different components are formed. The radial velocity of the absorption components of Si II and Sc II depend on the mean velocity of the stellar surface during the pulsation cycle, while the emission component of Sc II and [Ca II] are formed in the disc and are static.

[Ca II]. In the figure, the variable Si II profile illustrates the average movement of the stellar surface and its radial velocity decreases when the star expands and increases when the star contracts. In contrast, the double-peaked [Ca II] emission line remains virtually unchanged. The Sc II line shows similarities to both of them, the radial velocity of emission wings does not vary, while the central absorption component varies in sync with the Si II line in both radial velocity and depth. Thus, the emission component of Sc II could be static and formed in the circumstellar environment unaffected by the pulsations of the star, and its intensity varies as a result of the variable absorption component.

4.4. Summary of results

We monitored the yellow hypergiant V509 Cas over a seven-year period. We observed no large-scale changes in its variability. The star's T_{eff} has remained stable around 7800 K near the high-temperature border of the yellow void. In comparison to temperature data from Nieuwenhuijzen et al. (2012), the amplitude of short-term temperature fluctuations has decreased.

Based on our radial velocity measurements of Si II $\lambda\lambda 6347, 6371$ lines, the mean radial velocity (systemic velocity) is $v_{\text{sys}} = -60.7 \text{ km s}^{-1}$ and the total amplitude of the radial velocity variability is up to 20 km s^{-1} . These results are consistent with historical radial velocity data for V509 Cas. The star displayed similar values almost a century ago, -60.2 km s^{-1} with an amplitude of 12 km s^{-1} reported by Harper (1923). Remarkably, during that period the star had a substantially different temperature ($T_{\text{eff}} \sim 5000 \text{ K}$) and brightness ($V \sim 5.4 \text{ mag}$) (Nieuwenhuijzen et al., 2012).

The star's brightness in the V filter has a short-term variability timescale between 100 and 200 days, also reported by van Genderen et al. (2019). In addition to the short-term variability, we have observed a more extended longer-term variability with a timescale of 3–4 years. Over the past 50 years, the colour index of V509 Cas has displayed a gradual shift towards bluer values, with current $B - V$ values at 0.84 mag with a variability amplitude of up to 0.1 mag. This marks a unique phase of stability that has not been previously observed.

The possible existence of a disc-like structure around the star has been addressed by Aret et al. (2017c) based on the [Ca II] and [O I] lines in the spectrum. The behaviour of several absorption lines with emission components also supports this hypothesis. We specifically examined the Sc II $\lambda 6604$ line that has emission components with variable intensities in both wings at approximately $\pm 40 \text{ km s}^{-1}$ from the central absorption. The radial velocity of the absorption component behaves similarly to the Si II line due to pulsations. The radial velocity of the emission components does not change, and their intensity is affected by the current state of the absorption.

5. THE ‘GREAT DIMMING’ OF RW CEP

This Chapter is based on Paper III: *Atmospheric dynamics of the hypergiant RW Cep during the Great Dimming*.

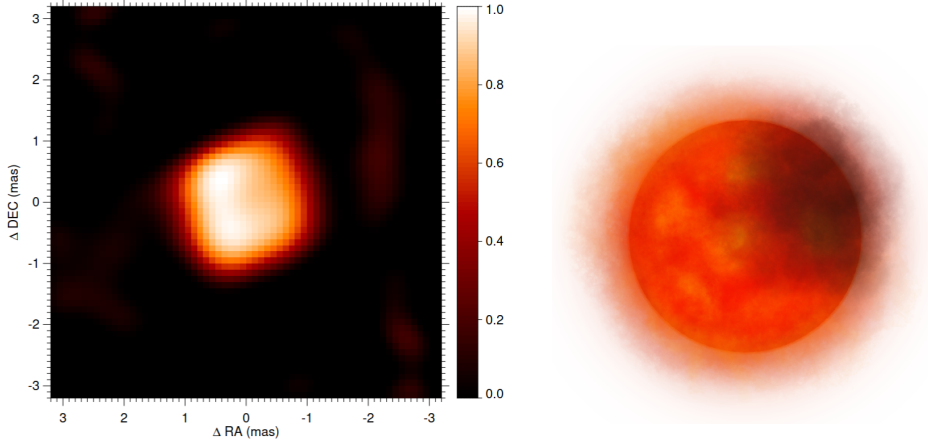
A. Kasikov, I. Kolka, A. Aret, T. Eenmäe, S. P. D. Borthakur, V. Checha, V. Mitrokhina, and S. Yang 2025, *A&A* 694, A153.

The hypergiant RW Cep has been included in various studies of variable and massive stars from the second half of the 20th century. Many of the studies did not specifically focus on RW Cep, although several authors wrote about the exceptional spectral features of the star (e.g. Gahm & Hultqvist, 1972; Merrill & Wilson, 1956). RW Cep gained significantly more attention after W. Vollmann and C. Sigismondi published a notice in the *Astronomer’s Telegram* about the star undergoing a historic dimming event (Vollmann & Sigismondi, 2022). We take a spectroscopic look at this event using high temporal cadence observations taken during and after the dimming minimum. And we put this event in the context of previous variability of the star based on archival data from the beginning of the 2000s.

5.1. History and the Great Dimming

RW Cep has been categorised as an irregular variable since at least 1933, with visual brightness between 6.8–7.5 mag (Keenan, 1942; Rajchl, 1933). Its spectral class has been a subject of discussion, as different studies have classified the star as G8 (Josselin & Plez, 2007; Josselin & Plez, 2003; Morgan & Roman, 1950), K0-2 (Gahm & Hultqvist, 1972; Humphreys, 1978; Keenan & McNeil, 1989), or M0 (Keenan, 1942). The uncertainty in determining the spectral class came from the extreme range in excitation of lines in the spectrum of the star (Morgan & Roman, 1950) or, as Leadbeater (2023) suggests, due to different criteria or spectral regions used by different authors. Nevertheless, authors agree that RW Cep is one of the most luminous stars known in the Galaxy with luminosity class Ia-0 (Humphreys, 1978; Keenan, 1942).

The unusual spectral features of RW Cep have warranted a few detailed studies (e.g. Josselin & Plez, 2007; Merrill & Wilson, 1956). The star has abnormally broad and strong lines (Gahm & Hultqvist, 1972) and its spectrum has been compared to YHG ρ Cas, HR 5171, and V509 Cas (Humphreys, 1978; Lobel et al., 2003a). RW Cep has infrared excess characterised by 150–250 K (Jones et al., 2023) or 300 K (Stickland, 1985) black-body emission. A dusty shell is located at 1000–1400 au from the star, which is compatible with a previous mass-loss ejection \sim 95–140 years ago (Jones et al., 2023). Five previous dimming episodes were identified by Anugu et al. (2024a) based on visual observational data, during which the brightness of the star decreased up to 1.2 mag below normal. The average length of a dimming episode has been around three years.



(a) H-band image reconstruction during the dimming minimum. Adapted from Anugu et al. (2023). (b) Illustration of the dust cloud shielding the starlight.

Figure 5.1: RW Cep during the dimming minimum.

The Great Dimming of RW Cep was reported in December 2022 by Vollmann and Sigismondi, when the star’s V magnitude had decreased from ~ 6.4 mag down to 7.6 mag. In the past 100 years, this recent event seems to be the most significant dimming episode, so calling it the ‘Great Dimming’ seems very appropriate (Anugu et al., 2024a). On several occasions (e.g. Anugu et al., 2024a; Anugu et al., 2023; Leadbeater, 2023; Vollmann & Sigismondi, 2022), parallels have been drawn between the dimming of RW Cep and the dimming event of Betelgeuse in 2019 (Montargès et al., 2021).

Leadbeater (2023) published spectroscopic monitoring observations taken during the dimming minimum from December 2022 to February 2023, when the star’s brightness was at its lowest. The spectra revealed new emission components superimposed on the absorption lines – especially a strong emission in $H\alpha$. They estimated the star’s spectral class during the dimming as K4 I.

Interferometric imaging of the surface of RW Cep in H and K filters with the Center for High Angular Resolution Astronomy (CHARA) array during and following the dimming episode revealed an asymmetric stellar surface, extended plume emissions, and localised emission and absorption due to dust (Fig. 5.1a). Anugu et al. (2023) compared near-infrared K-band spectra taken before and during the dimming. They detected added flux that corresponds to dust emission. Additionally, the CO $2.29 \mu\text{m}$ line appears significantly deeper, indicating a lower photospheric temperature. They estimate the T_{eff} from the pre-dimming spectrum taken in 2005 to be 4200 K, and during the dimming 3900 K or even less.

5.2. Observations and methods

5.2.1. Spectroscopic data

We collected spectroscopic data from five instruments, covering the years 1999–2024, though there are very few observations from 2007 to 2021. In this section we give a brief overview of all spectroscopic observations used in this paper, the individual observations are listed in App. D of Paper III.

ELODIE. We use archival spectra from the beginning of the 2000s. ELODIE echelle spectrograph was operated at the 1.93 m telescope in Observatoire de Haute-Provence (Moultaka et al., 2004). The spectra cover the wavelength range 3850–6800 Å, with a spectral resolution of $R \sim 42\,000$ (Baranne et al., 1996). The reduced spectra were accessed through the ELODIE archive¹. The signal-to-noise ratio (S/N) of the spectra is 200–300.

Dominion Astrophysical Observatory (DAO). We include observations taken with the McKellar spectrograph at the 1.2 m telescope (Monin et al., 2014). The data were accessed through the Canadian Astronomy Data Centre archive². The spectra have resolution $R \sim 17\,000$, the wavelength ranges of spectra vary slightly, but generally cover the range 6300–6900 Å. The S/N of the spectra is 100–300.

Echelle SpectroPolarimetric Device for the Observation of Stars (ESPaDOnS). Two high resolution ($R \sim 80\,000$) and very high S/N (>600) spectra from 2006 are from the Polarbase³ archive (Donati et al., 1997; Petit et al., 2014). Observations cover a very wide wavelength range from 3700 to 10 500 Å.

Ondřejov Observatory. We included one observation epoch from the 2-meter telescope in Ondřejov Observatory in the Czech Republic, operated by the Astronomical Institute of the Czech Academy of Sciences. The spectra were taken in wavelength range 6250–6750 Å, with resolution $R \sim 40\,000$ and S/N 330.

Fibre-fed Echelle Spectrograph (FIES). We observed RW Cep during its dimming period with FIES (Telting et al., 2014) at the Nordic Optical Telescope on La Palma. The spectra were taken in medium-resolution ($R \sim 45\,000$) mode covering the wavelength range 3630–8980 Å. The spectra were reduced with the standard FIEStool pipeline (Stempels & Telting, 2017). The S/N is 200–300.

Tartu Observatory (TO). Observations were made with the long-slit spectrograph ASP-32 mounted in the Cassegrain focus of the 1.5 m telescope AZT-12. The monitoring program began in December 2022, at the brightness minimum of RW Cep, and the latest spectra included in this paper were taken 1.5 years later, in May 2024. The spectra were taken using the 1800 lines mm^{-1} grating with the spectral resolution $R \sim 10\,000$, covering the wavelength range 6300–6600 Å (Folsom et al., 2022). The S/N of spectra is 200–300. The data were reduced using the IRAF⁴ (Tody, 1986) packages: NOAO, IMRED, CCDRED, CTIOSLIT, and RV.

¹ <http://atlas.obs-hp.fr/elodie/>

² <https://www.cadc-ccda.hia-ihp.nrc-cnrc.gc.ca/>

³ <http://polarbase.irap.omp.eu/>

⁴ <https://iraf-community.github.io/>

Wavelength calibration was made based on the ThAr hollow cathode lamp. The spectrograph is mounted at the Cassegrain focus of the telescope, which causes minor flexure in the instrument due to telescope movement. This affects the accuracy of the wavelength scale and the resulting error is wavelength dependent, larger ($\sim 0.1 \text{ \AA}$) near 6300 \AA , and near-zero at 6600 \AA . For radial velocity measurements of a single line, this can be easily remedied by selecting nearby lines with known wavelengths and measuring the difference (DIB at $\lambda 6379.01$ was used in our previous work; Paper II). However, in this paper, we measure the radial velocities of a substantial amount of lines over the entire spectral range, so this single-line approach is inadequate.

To remedy the instrumental wavelength error, we calculated a correction curve. We measured the wavelengths of five relatively strong night sky emission lines in the sky background of a spectrophotometric standard star 10 Lac and compared them to the wavelengths from the European Southern Observatory UV-visual echelle spectrograph (UVES; Hanuschik, 2003). Based on the wavelength differences, we calculated a linear correction curve. To correct the spectra of RW Cep, we scaled the correction curve to each individual spectrum using the strongest atmospheric [O I] $\lambda 6363.776$ line. Measuring all five lines for each spectrum of RW Cep is not feasible, because the other four are much weaker and only become visible in long (>1 h) exposures. Following this wavelength scale correction, the radial velocities measured from TO spectra agree very well to those measured from FIES spectra at nearby dates. We can guarantee velocity accuracy of approximately $\sim 2.5 \text{ km s}^{-1}$. The spectra were normalised to (pseudo-)continuum with the SUPNET software (Róžański et al., 2022) using a series of carefully selected “anchor points” in the spectra.

5.2.2. Spectroscopic measurements

Our TO spectral time series begins at the dimming minimum with high temporal cadence. The observations were made with TO long-slit spectrograph in the wavelength range of $6300\text{--}6600 \text{ \AA}$. Therefore, most of the spectral lines discussed in this paper fall in that region.

Radial velocity. We measured the radial velocities of spectral lines by using Gaussian fitting of the line profile core or by calculating the first moment (intensity weighted velocity) of the spectral line:

$$v_{\text{rad}} = \frac{\sum_i^N I_i v_i}{\sum_i^N I_i}, \quad (5.1)$$

where I is intensity and v is velocity. The Gaussian method was preferred for TO, DAO, and Ondřejov spectra, where the spectral line profiles were more symmetric and cores of the spectral lines could be fitted well. The moment method was the preferable method used for FIES, ELODIE, and ESPaDOnS spectra, where the higher spectral resolution reveals the finer structure and asymmetry of the spectral

lines. Measurements of the first moment can be significantly affected by any blends in the line wings. The spectrum of RW Cep is densely packed with spectral lines; therefore, deblending was necessary in many cases. To deblend two lines, we fitted a Gaussian to the line next to the target line and subtracted the fit. When deblending was not possible and the centre of the line was symmetric enough to be approximated with a Gaussian, we occasionally opted for Gaussian fitting in the case of FIES and ELODIE spectra as well. In the case of a strong blend and asymmetric spectral line, the radial velocity could not be reliably measured.

The most significant contribution to the error of the first moment is the selection of the wavelength window in which it is calculated. To estimate the uncertainty from window selection, we measured the line moment in windows of various sizes that extended past line wings or included only the central part of the line. In all ELODIE, ESPaDOnS, and FIES spectra, we measured some relatively unblended spectral lines (e.g. Si II λ 6347 and Fe I λ 6358) using around ten different window widths. The standard deviation of moments calculated in different wavelength windows was $\sim 1.2 \text{ km s}^{-1}$, though in cases where the S/N of the spectrum is low (~ 100), or the line is weak ($<20\%$ continuum depth), errors can be up to $\sim 2 \text{ km s}^{-1}$.

Line depth. We measured the depth of each spectral line. We define the depth of spectral line in respect to the continuum, and higher values correspond to stronger absorption lines. Line depth is a more robust measure of the intensity of a spectral line than the equivalent width. Equivalent width can be complicated to measure when the lines are blended – as is often the case in RW Cep – and if the continuum is difficult to place. Line depth is also affected by inaccuracies due to the position of the continuum, but we minimised it by carefully selecting the points through which the pseudo-continuum was placed for the spectra of RW Cep. We measured the line depth either through Gaussian fitting in the cases where it was used for radial velocity or from the lowest point in the spectral line. Unlike equivalent width, line depth is sensitive to the resolution of the instrument, which makes it more difficult to compare results from different instruments. In the case of RW Cep, this is not a significant issue due to its extremely wide spectral lines, so even with moderate resolution, the line profile is physical rather than instrumental. We estimate the precision for line depth measurements at 0.006–0.008.

5.2.3. Photometry

We collected photometric data from several freely accessible archives.

The Kamogata/Kiso/Kyoto Wide Field Survey (KWS). The observations were taken from 2011 to 2024. The data includes measurements in Johnson-Cousins *V* and in Cousins *I_c* filters (Maehara, 2014),⁵ a total of 416 nights of *V* filter observations and 312 nights of *I_c* filter observations. The mean given instrumental uncertainty of the *V*-filter measurements is 0.006 mag, and for *I_c*-filter observations

⁵ <http://kws.cetus-net.org/~maehara/VSdata.py>

0.009 mag. The mean scatter of measurements taken within one night is around 0.011 mag.

We cleaned the KWS data by removing points with instrumental uncertainties larger than 0.03 mag, and by filtering the data with a 10-day running median window and removing points that deviated by more than 3σ . Additionally, observations taken within one night were averaged, and nights with a measurement scatter in the V filter >0.04 mag or in the Ic filter >0.05 mag were excluded. These values are significantly larger than the mean scatter within one night, which is around 0.011 mag for both filters. We also adopted this value as uncertainty displayed in the figures for KWS, as it better describes the scatter of data points than the instrumental uncertainty given for each individual point. The mean uncertainty for ($V-Ic$) colour is 0.017 mag.

American Association of Variable Star Observers (AAVSO). W. Vollmann, a member of the AAVSO (observer code VOL) has observed RW Cep using a digital camera in the Johnson-Cousins V filter (transformed into standard magnitudes) in 2018–2024 (Vollmann, 2024). The mean uncertainty of the observations is 0.013 mag. The magnitudes in the AAVSO database were systematically slightly lower than those reported by KWS – a mean difference of ~ 0.08 mag. To line up the data from AAVSO and KWS, we shifted all measurements from AAVSO by this value.

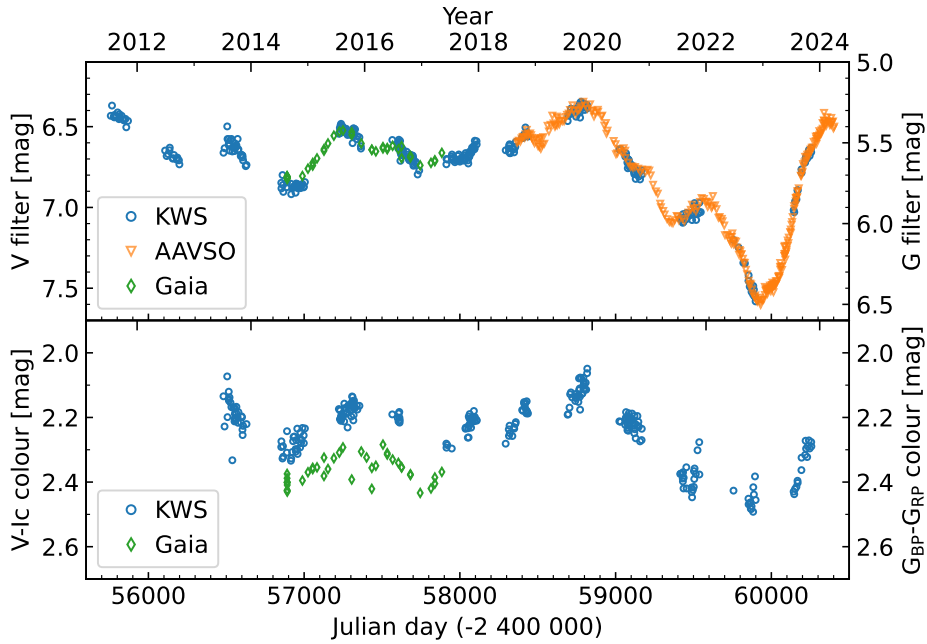
Gaia. Additionally, we have included multi-epoch photometry from *Gaia* in G , G_{BP} and G_{RP} filters (Gaia Collaboration et al., 2016, 2023). The uncertainties given for G -band are ~ 0.3 mmag, for G_{BP} -band ~ 0.9 mmag, and the G_{RP} -band ~ 0.6 mmag.

5.3. Results

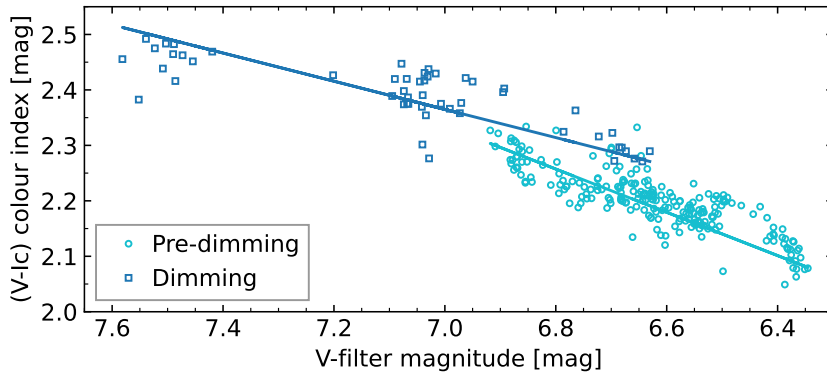
5.3.1. Light curve

In Fig. 5.2a upper panel, we plotted the AAVSO light curve by W. Vollmann, the smoothed KWS V -filter data, and the *Gaia* G -band magnitude. The *Gaia* data and AAVSO measurements show a smooth variability of brightness in 2012–2020 between 6.4 and 6.9 mag in V -filter. The Great Dimming of RW Cep lasted from 2020 to 2024 and minimal brightness was from Dec 2022 to Jan 2023 at around 7.6 mag. The recovery from the dimming minimum was smooth, without significant bumps or pauses. By mid-2024 the brightness was back to normal pre-dimming levels. Our spectroscopic observations begin near dimming minimum and cover the period of brightness recovery.

In the bottom panel of Fig. 5.2a, we plotted the ($V-Ic$) colour index from KWS and ($G_{BP}-G_{RP}$) colour from *Gaia*. Both colour indices show similar variability during the pre-dimming period, between 2.1 and 2.4 mag for ($V-Ic$) and 2.3–2.45 mag for ($G_{BP}-G_{RP}$). During the dimming RW Cep reddened by 0.2–0.3 mag in ($V-Ic$). The change in colour was accompanied by a change in the T_{eff} (Anugu



(a) Upper panel: V -filter light curve from AAVSO and KWS data, including G -filter data from Gaia. Lower panel: $(V-Ic)$ colour together with $(G_{BP}-G_{RP})$ colour from Gaia. Each point corresponds to one night. The uncertainties are smaller than the data points. We note that the y-axes for Gaia data are on the right of the figure, but the scale unit sizes are the same for both V -filter and Gaia data. However, the axis limits for V filter and Gaia are different in the upper panel.



(b) Correlation between V -filter magnitude and $(V-Ic)$ colour index based on KWS data and two linear fits: one corresponds to normal variability, and the other to the dimming period data. The standard deviation of the fit residuals is 0.03 mag for the pre-dimming period and 0.04 mag for the dimming period. For $(V-Ic)$ colour, KWS has an instrumental uncertainty of about 0.025 mag.

Figure 5.2: Photometric data. Figures adapted from Paper III.

et al., 2023). There is a very good correlation between the brightness change in V filter and the colour index, as seen in Fig. 5.2b. The slope of the correlation changes during the dimming, indicating the changed state of RW Cep.

There are some periodicity estimates for the light curve of RW Cep. Anugu et al. (2024a) find a variable period between 350 and 800 days, with a peak at 403 days, and also a longer ~ 6.8 -year period. Previous studies by Percy & Kolin (2000) and Chinarova & Andronov (2000) found periods between 600 and 900 days, while Kholopov et al. (1998) detected a shorter, 346-day period and Chinarova & Andronov (2000) also found a longer than 2000-day period.

5.3.2. Following $H\alpha$ through the dimming

Figure 5.3 shows the radial velocity (first moment, Eq. 5.1) variability of the $H\alpha$ absorption component during and after the dimming minimum. Small panels at the sides show example line profiles. The $H\alpha$ profile of RW Cep is non-symmetric and slightly variable in the 'calm' state of the star based on spectra from 1999 to 2016. The v_{rad} at that time varied between -55 and -40 km s $^{-1}$. An extended timeline of the variability of the $H\alpha$ profile in RW Cep is given in App. B of Paper III.

The Great Dimming introduced a strong emission component to the line profile of $H\alpha$ that spans a wide range of velocities. A hint of emission appeared more than a year before the dimming minimum in a spectrum from September 2021, when the blue wing of the $H\alpha$ line reached almost 10% above the continuum level. Anugu et al. (2024a) suggests, based on light curve analysis, that the gas ejection began in 2020. In September 2021, the brightness of RW Cep was already rapidly decreasing (light curve in Fig. 5.2a). However, at that time, the v_{rad} of $H\alpha$ was at a normal level (-42 km s $^{-1}$). The brightness decrease indicates that around August 2021, the ejected gas was already condensing into dust, which came into our line of sight and began shielding starlight. The movement of the cloud was perhaps due to the rotation of the star, simply a physical movement, or a combination of both. The main panel of Fig. 5.3 starts about a year later, from August 2022, when the emission component in the blue wing of $H\alpha$ was readily visible (panel no. 1).

The emission strength increased in the following months while the star's brightness decreased. The emission reached its maximum in the beginning of January 2023 (panel no. 2), during the brightness minimum. The peak of the emission was located blueward (at lower velocities) of the central absorption, creating the asymmetric profile. The emission width extended from near -120 km s $^{-1}$ to velocities up to 0 km s $^{-1}$. In the figure, the wings of the emission component can be seen on both sides of the photospheric absorption.

By May 2023 (panel no. 3), the emission strength decreased, and the red wing of the absorption line broadened, resulting in an increase in the measured v_{rad} . In the following panels 4 and 5, we see a further decrease in the strength of the emission component and a strongly asymmetric tilt of the absorption line towards higher velocities. From interferometry of Anugu et al. (2023), it is visible that by

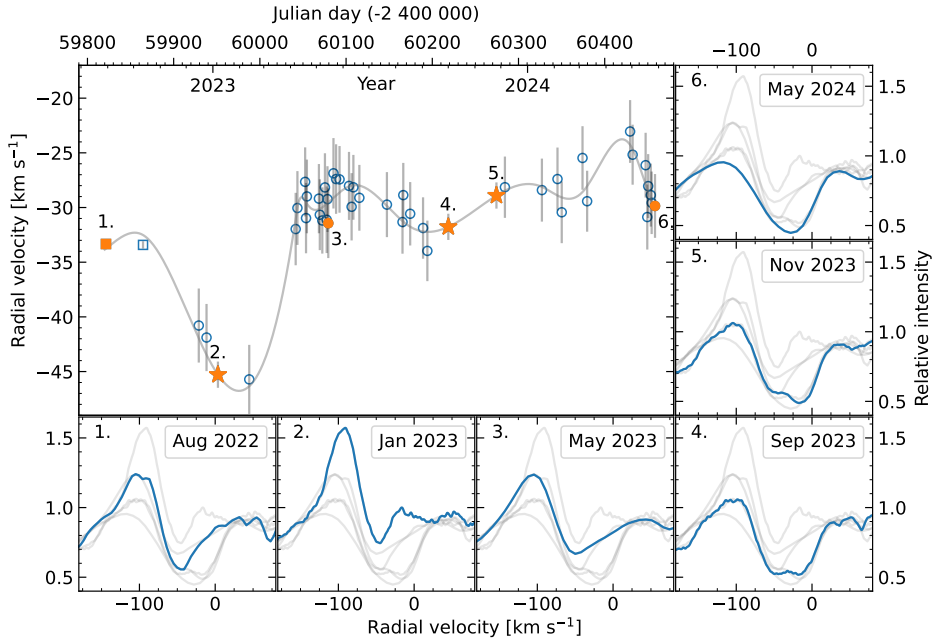


Figure 5.3: Variability of the radial velocity and $H\alpha$ line profile during the dimming. The main panel showcases the v_{rad} variability, and the small numbered panels around it correspond to spectral line profiles on dates highlighted and numbered on the main panel. Behind the highlighted line, all other five profiles are drawn in light grey. Panel no. 1 is from before the dimming minimum, but the emission is already visible. Panel no. 2 is taken when the star was faintest. The following panels, 3–6, were taken during the brightening. Panels 2, 4, and 5 are FIES spectra; panel 1 is from DAO; and panels 3 and 6 are TO spectra. The lower resolution of panels 3 and 6 results in a smoother profile shape. The systemic velocity has not been subtracted from the velocity axis. Figure adapted from Paper III.

October 2023 the shape of the stellar surface had become much more symmetric. Based on the spectral features of $H\alpha$, the dust and gas ejected during the eruption had not yet fully dissipated by then. The emission in $H\alpha$ was down to continuum level by the beginning of 2024 (panel no. 6), when the star regained its former brightness. However, by mid-2024 the $H\alpha$ line profile had not yet recovered its former depth or pre-outburst radial velocity, which could still be the influence of the weakened emission.

5.3.3. Radial velocity variability

We measured radial velocities of 33 unblended Fe I lines, the details of all lines are given in the App. A of Paper III. Of these lines, 16 are well-resolved in TO spectra and we followed their variability through the dimming event. The spectral line data for all selected lines (wavelength, excitation potential of the lower level E_{low} and oscillator strength $\log gf$) are from the Belgian Repository of fundamental Atomic

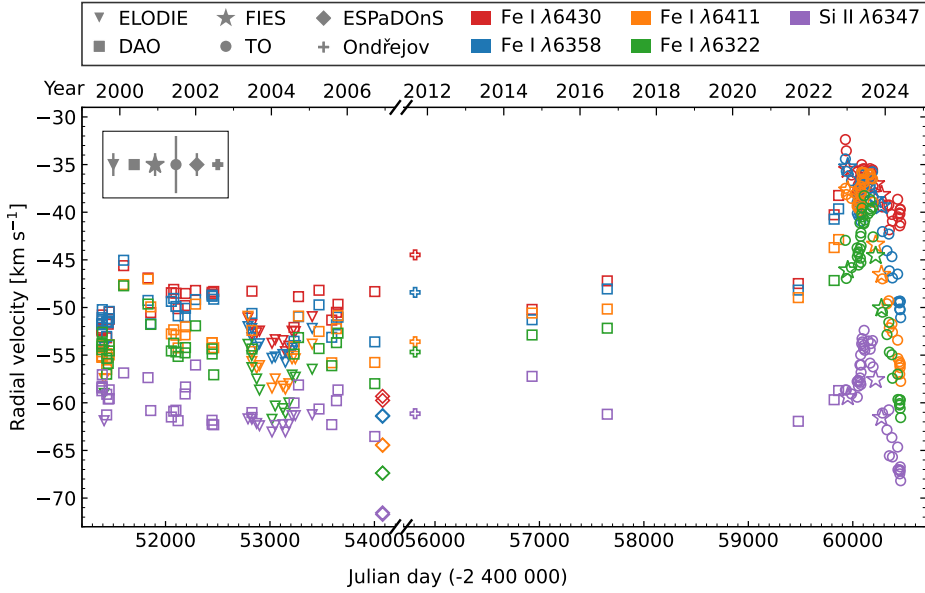


Figure 5.4: Mean core velocities of four representative Fe I lines and a Si II line. The full timeline covers the years from the beginning of the 2000s until mid-2024. We note that there is a gap in the x-axis. Different symbols mark data from different spectrographs (mean error bars for each instrument are given in the top-left corner). The colours red, blue, orange, and green correspond to Fe I $\lambda\lambda$ 6430, 6358, 6411, and 6322 lines respectively, and purple corresponds to Si II λ 6347. Figure adapted from Paper III.

Data and Stellar Spectra (BRASS) database⁶ (Lobel et al., 2019).

In Fig. 5.4, we have drawn a full timeline of the v_{rad} variability of four distinct Fe I lines $\lambda\lambda$ 6430, 6358, 6411, and 6322 from 1999 to 2024. These four lines are representative subset of our sample, their E_{low} values vary from 0.8 to 3.6 eV. Additionally, we have added the Si II λ 6347.11 line (E_{low} 8.121 eV and $\log gf = 0.297$), which has a much lower v_{rad} .

At the beginning of 2000s, the spectral lines span a range of velocities from -63 to -45 km s^{-1} , with variability amplitudes of individual lines in 5 – 10 km s^{-1} range. We consider this period as the 'normal' or 'calm' state of the star. There is a small dip in the v_{rad} curve in 2003–2005, but comparison with the long-time visual brightness curve (Anugu et al., 2023) is stable between 6.8 and 7 mag at that time. At the same time, the radial velocity of Si II shows barely any change. Other variations include an abrupt ~ 10 km s^{-1} jump in early 2000; and a sudden significant drop in late 2006. We have very little data from 2006 to 2021. The Ondřejov spectrum from 2011 and DAO spectra from 2014, 2016, and 2021 show that the radial velocity remained relatively on the same level as in the beginning of 2000s. Throughout the years, we see a clear gradient in the v_{rad} of different spectral lines. Some lines, such as Si II and Fe I λ 6322 have systematically lower v_{rad} than

⁶ <http://brass.sdf.org/>

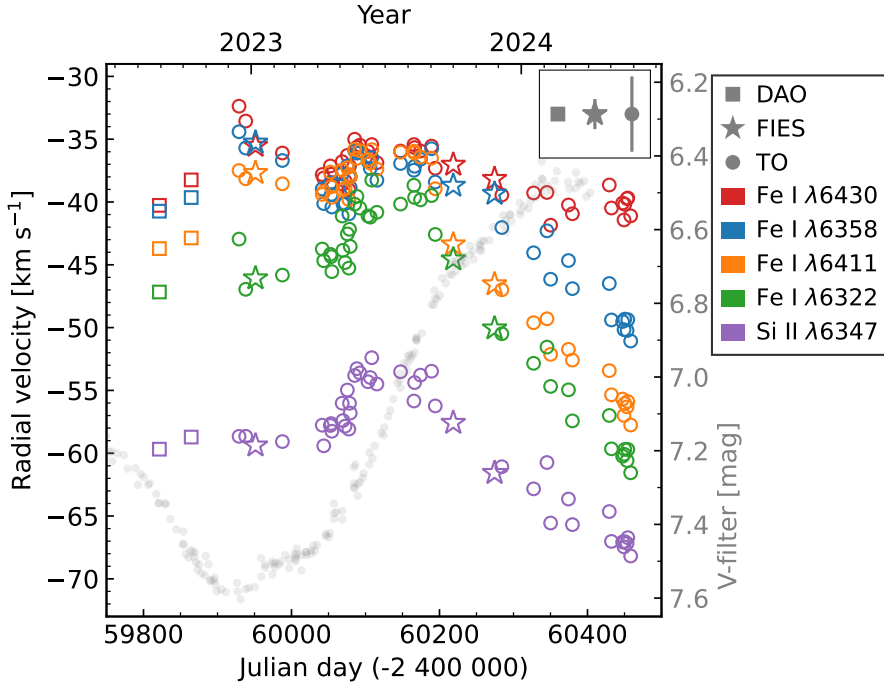


Figure 5.5: Zoom-in on the dimming period from Fig. 5.4 with the same spectral lines using the same labels and colours. Light grey shows the V -filter light curve for reference (y-axis on the right). All four Fe I lines achieve similar maximum v_{rad} during the dimming minimum, but the post-dimming behaviour is different: some lines have returned to their normal levels (orange and green in the figure), while others (red) retain the high radial velocity for longer. Figure adapted from Paper III.

other lines, such as Fe I $\lambda 6430$. Even though the radial velocities of individual lines are variable over time, all lines vary almost in synchronisation with each other during the velocity drops and rises.

Radial velocity during the Great Dimming. There is a sharp rise in velocity compared to the calm state. In Fig. 5.5 we show the v_{rad} curves along with the brightness in the V filter for reference (light grey). For the Fe I lines, there seem to be two separate velocity maxima – one corresponds to the dimming minimum in late-2022 and early-2023 (JD $\sim 2\,459\,950$) and the other peak approximately six months later, in May-June 2023 (JD $\sim 2\,460\,100$). For Si II, there is only one velocity maximum in May-June. The Si II line is generally found in much hotter stars than RW Cep, and therefore must be formed deep in the atmosphere. During the peak, the velocities of the Fe I and the Si II were $10\text{--}20\text{ km s}^{-1}$ over the normal level. The initial maximum that corresponds to the dimming minimum is most likely related to the added emission component that we saw in $H\alpha$. The second velocity maximum half a year later, and the following behaviour of the spectral lines are related to large-scale motions in the atmosphere that reach into deeper atmospheric layers.

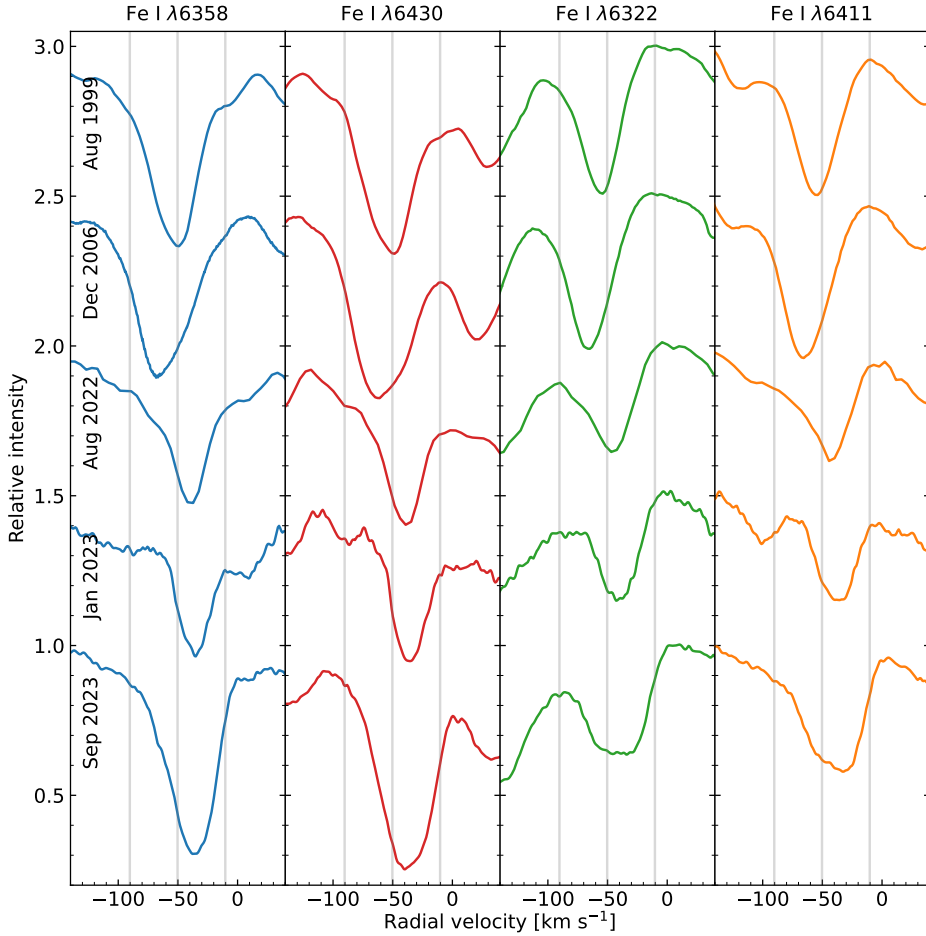


Figure 5.6: Comparison of four Fe I lines (columns) on different epochs (rows) before and during the Great Dimming. The $\lambda\lambda 6358, 6430$ lines represent the strong Fe I lines and the $\lambda\lambda 6322, 6411$ represent the weak Fe I lines. The colours correspond to Fig. 5.4. The central thin grey line traces the v_{sys} and two additional lines are drawn at $\pm 40 \text{ km s}^{-1}$ to guide the eye. The spectra are from ELODIE (August 1999), ESPaDOnS (December 2006), DAO (August 2022), and FIES (January and September 2023). Figure adapted from Paper III.

After the dimming minimum, the lines have behaved quite differently. Some (such as Fe I $\lambda\lambda 6411, 6322, 6358$) have almost returned to their normal velocities within a year after the velocity maximum. However, the velocities of other lines (e.g. $\lambda 6430$) still remain almost 10 km s^{-1} higher than normal. The velocity span of all Fe I lines post-dimming is $\sim 25 \text{ km s}^{-1}$.

5.3.4. Variability in spectral line profiles

In Fig. 5.6, we have drawn the line profiles of the four Fe I lines from Fig. 5.4 (the colour palette is the same). Before the dimming, all Fe I lines displayed minor variability (1999 and 2006). Shortly before the dimming minimum, in August 2022, the v_{rad} has increased and the line depths and widths have decreased. This can be attributed to the added blue-shifted emission. For the Fe I lines, the emission is not strong enough to reach higher than the continuum level. The emission strengthens by January 2023, where the resolution is sufficiently high to trace the small emission bump near -70 km s^{-1} . There is also blue-shifted emission in many other low-excitation absorption lines: Ca I, Ti I, Sc II, V I.

The added emission component in the Fe I and many other absorption lines means that the line-depth-ratio method (Sect. 4.2.4) would be unreliable for estimating the T_{eff} of RW Cep during the dimming period. Therefore, we rely on the T_{eff} measurements from Anugu et al. (2023) of 4200 K in the calm state and 3900 K during the dimming minimum. The variability in T_{eff} is also supported by the change in ($V-I_c$) colour index and the shift in its variability behaviour (Fig. 5.2b). During the dimming minimum, we did not detect any strong TiO bands in the spectrum of RW Cep. If present, they are either weak or strongly blended with other lines. TiO bands were present in the YHG ρ Cas during its outburst, and they form in the upper atmospheric layers with $T_{\text{eff}} < 4000 \text{ K}$ (Lobel et al., 2003a).

After the dimming minimum, by September 2023, the emission has almost disappeared in $H\alpha$, and in Fe I lines. The two stronger Fe I lines $\lambda\lambda 6358, 6430$ no longer have any indication of an emission affecting their blue wings. Additionally, they have become significantly stronger, even stronger than before the dimming. This could be caused by the decrease in T_{eff} , which would strengthen lines with lower E_{low} values (Fe I $\lambda 6358$ has $E_{\text{low}} = 0.859 \text{ eV}$ and $\lambda 6430$ has $E_{\text{low}} = 2.176 \text{ eV}$). The weaker Fe I lines $\lambda\lambda 6322, 6411$ show a slightly different behaviour. We see the disappearance of the added emission component in the blue wing, but by September 2023, the lines have grown increasingly wider, with especially enhanced red absorption wing. The line profile has acquired an almost rectangular shape, as the lines have remained shallower than normal. The decreased T_{eff} during the dimming period could account for the shallower line depth in lines with a higher E_{low} ; however, it does not account for the increased line width.

Similar flat-bottomed absorption lines have been recorded in the spectrum of ρ Cas. These are strong low-energy absorption lines, where the line profile is affected by added emission from cooler and diffuse shells near the star (Lobel et al., 1998). However, in our case, the weaker and higher E_{low} lines have flat-bottomed profile shapes (Fe I $\lambda 6322$ has $E_{\text{low}} = 2.588 \text{ eV}$ and $\lambda 6411$ has $E_{\text{low}} = 3.654 \text{ eV}$). It would be reasonable to think that any persisting emission effect would primarily affect the lines with lower E_{low} values.

Figure 5.7 illustrates the variability of line profiles during the dimming (c.f. Fig. 2.5 which shows the ‘normal’ convective variability). The left column shows

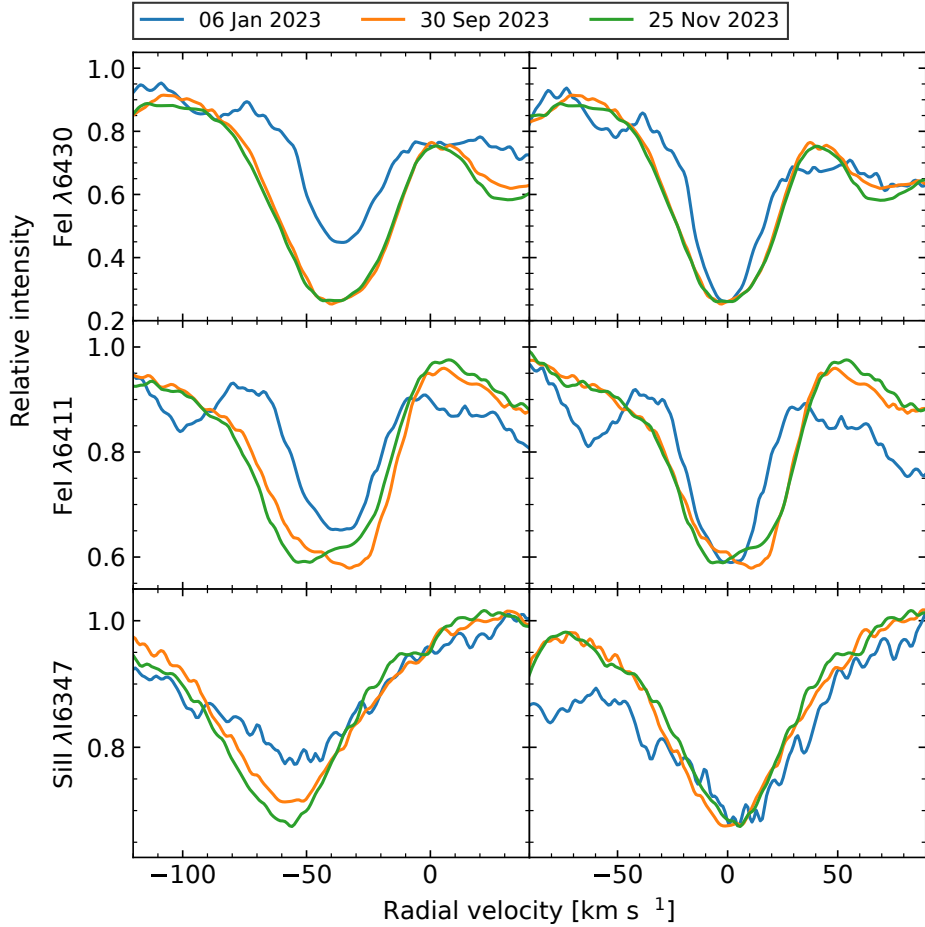


Figure 5.7: Variability of absorption line profiles. We have plotted FIES spectra on three dates. The January spectrum (blue) was taken during the dimming minimum, and the other two were taken nine months (orange) and 11 months (green) later, when the brightness had returned to a near-normal level. Figure adapted from Paper III.

the observed line profiles drawn on top of each other, the colours mark different epochs. The right column shows the same line profiles, but centred in v_{rad} and scaled to the depth of the deepest line. This is done for two Fe I lines: $\lambda 6430$ line in the top panels and $\lambda 6411$ on the bottom panels. The Fe I $\lambda 6430$ is a very strong line that shows minor changes in its v_{rad} during the event, up to 10 km s^{-1} . While the Fe I $\lambda 6411$ is a weaker line that shows significantly more variability in v_{rad} , up to 25 km s^{-1} (cf. the v_{rad} curves in Fig. 5.4).

In January 2023, the line profiles are much shallower and narrower. When scaled to the same depth, the added emission contribution can be seen in both wings of the line. In the Si II line ($E_{\text{low}} = 8.121 \text{ eV}$, $\log gf = 0.297$), there is no indication of the line profile becoming narrower, and the v_{rad} curve does not show a velocity maximum during the dimming minimum (Fig. 5.5). It is slightly shallower

in January, which can be explained by the T_{eff} decrease. The September and November profiles are almost identical for the $\lambda 6430$ line, but the weaker $\lambda 6411$ line shows a change from a more enhanced red wing absorption to a stronger absorption in the blue wing. This change in line profile shape causes the radial velocity of this weaker line to decrease quite rapidly in comparison to the stronger lines (cf. Fig. 5.5). The Si II line shows a decrease in radial velocity, while the line depth increases.

5.3.5. Variability in depths of spectral lines

We measured the line depths of the selected Fe I lines from TO spectra during the dimming (Fig. 5.8). Two significant observations can be drawn from this figure: 1) Stronger lines exhibit greater variability in their line depth compared to weaker lines; 2) There is a noticeable shift in the trend of line depth changes in mid- to late-2023, where the increasing line depths appear to plateau, and in the case of weaker lines, even begin to decline. The change in the trend takes place after the radial velocity maximum in mid-2023.

In Fig. 5.9a, we correlate the variability of Fe I radial velocity with the line depths. We have plotted the v_{rad} versus line depth on each observation epoch (the grey circles for TO data and stars for FIES data). Next, we calculated a linear fit through the data points for each epoch. The grey areas on the plot mark these linear fits. Area no. 1 describes the relation between v_{rad} and line depth for all observations made between March 2023 and August 2023; Area no. 2 describes the relation between v_{rad} and line depth in observations starting from December 2023 onwards.

We highlight in blue a couple of epochs from the brightness minimum in late 2022 and early 2023, when the lines were very shallow and the correlation slopes were notably steeper. We notice a significant change in the slope of the correlation between v_{rad} and line depth between the two periods. The correlation shifted in September-November 2023, the FIES observations taken during that time are highlighted orange on the plot. The line depths of TO and FIES data are not directly comparable due to the different resolutions (spectral lines of TO are shallower, and thus FIES data have not been included in Fig. 5.8), but the slope of the correlation is comparable. The change in correlation corresponds to the stabilisation of line depths.

We also measured the spectral line depths and drew a correlation plot for the early 2000s data (Fig. 5.9b). On most epochs, the correlation between v_{rad} and line depth follows the same trend marked with the grey area. The true correlation might not be fully linear, especially for the weakest lines, which have a strong preference towards lower velocities. Epochs with distinct correlation slopes have been highlighted with colours. The first group: blue, orange, and red correspond to the sudden increase in radial velocity in the year 2000 and the correlation slopes resemble the beginning of the Great Dimming. In the light curve (visual

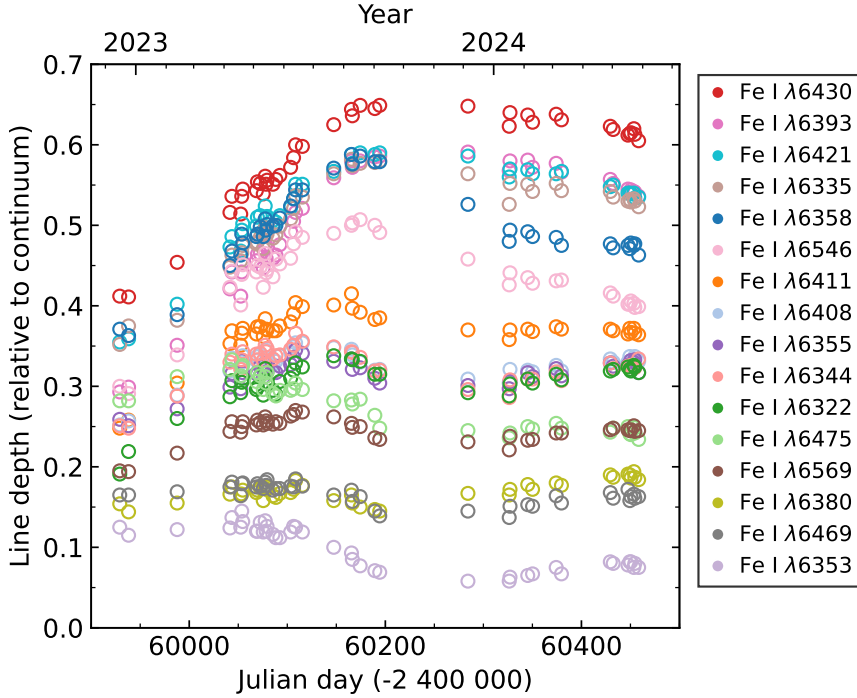
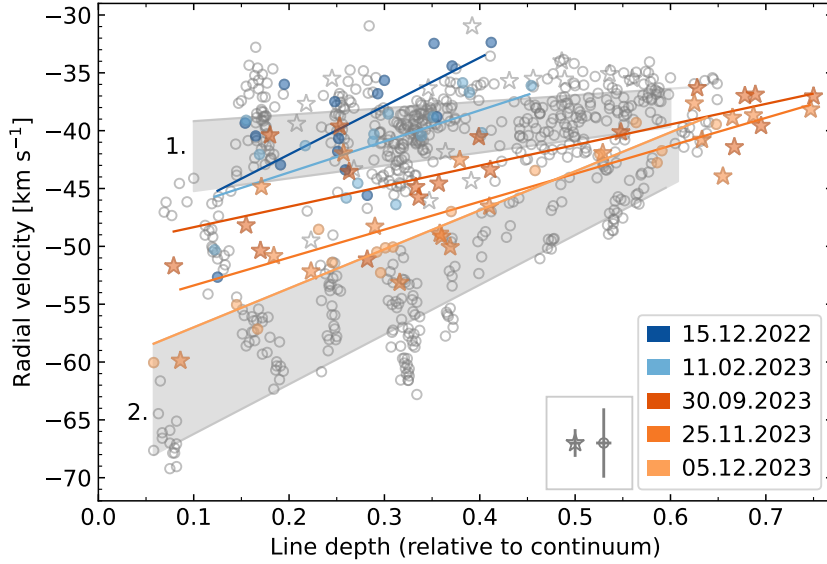


Figure 5.8: Line depth variability in time measured from TO spectra. Colours mark different Fe I lines. The Fe I lines from Fig. 5.5 are marked here with the same red, blue, orange and green colours. Stronger spectral lines have higher line depth values. The error bars are up to the same size as the data points. Figure adapted from Paper III.

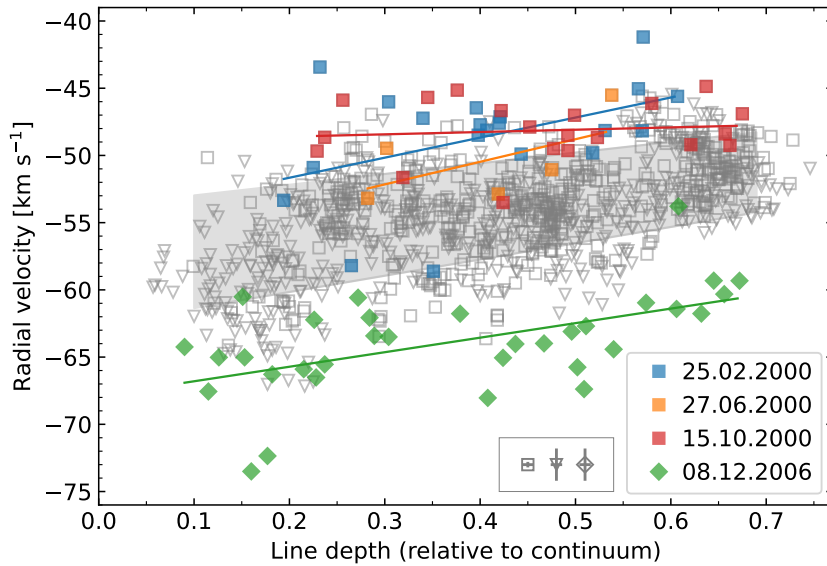
observations given by Anugu et al., 2024a), we see a minor local minimum at that time with visual brightness 7.3–7.1 mag. The other outliers in the early 2000s are the two ESPaDOnS spectra from December 2006 (one of them is plotted in green on the figure). From these spectra, we measure the lowest v_{rad} values for RW Cep. Otherwise, the spectra seem similar to others from that period. Regrettably, we do not have any more spectra following the ESPaDOnS measurements.

5.3.6. The velocity gradient and systemic velocity

Systematic blueward velocity shifts in the stellar atmosphere are the result of granulation (Gray, 2021): more light originates from the central parts of the granules than the inter-granular areas. Therefore, our radial velocity values measure the granule rise velocity averaged over the stellar disc. The weaker Fe I lines, but also Si II, have generally $E_{\text{low}} > 2.5$ eV values and describe the motions deeper in the atmosphere. Stronger lines describe the upper parts of the atmosphere. We have shown a clear correlation between line depth and its radial velocity in Fig. 5.9a and Fig. 5.9b. The velocity stratification remains the same during 1999–2006, as well as in the extraordinary conditions during the dimming period.



(a) Correlation during the dimming. TO data are marked with circles and FIES data with stars. The grey areas describe the correlation during two distinct time periods: Area no. 1 is between March 2023 and Aug 2023; Area no. 2 is from Dec 2023 onwards. Highlighted dates show the change in correlation. The correlation shift from area 1 to area 2 happened within a few months in late 2023 (orange). During the dimming minimum the lines were extremely shallow (blue).



(b) Correlation in 1999–2006. The grey area shows the standard correlation slopes. Different colours highlight non-standard correlations. Shapes correspond instruments: square is DAO, triangle is ELODIE, and diamond is ESPaDOnS.

Figure 5.9: Correlation between v_{rad} and line depth. Figures adapted from Paper III.

The velocity gradient due to granulation (or in our case, giant convective cells) allows us to estimate the systemic velocity (v_{sys}) of RW Cep. For this calculation, we used the mean velocities of the strongest Fe I lines during the relatively calm period at the beginning of the 2000s. We measured six lines with line depth values ≥ 0.60 and averaged their radial velocities in 1999–2006 (leaving out the December 2006 event), resulting in a velocity of $-50.3 \pm 3.3 \text{ km s}^{-1}$, which we adopt as the v_{sys} of the star. Previous literature estimates are -54 km s^{-1} (Merrill & Wilson, 1956) and -62.8 km s^{-1} (Gahm & Hultqvist, 1972).

Kravchenko et al. (2019) studied the atmosphere of μ Cep, a RSG with a radius of nearly $1000 R_{\odot}$ and effective temperature $T_{\text{eff}} \approx 3700 \text{ K}$ (at first glance a rather similar star to RW Cep). They measured the first moments of spectral lines originating at different depths of the star’s atmosphere over a time period of almost 7 years. They also detected a velocity gradient in the atmosphere, but the velocity gradient they measured was not stable in time: over a timescale of 300–800 days, the gradient reversed. If the upper layers had previously had higher radial velocities, then the velocities decreased and the velocities of deeper layers increased. The star underwent three variability cycles within their observation period. This was considered a clear indication of the movement of giant convective cells and the turn-over of material in the atmosphere.

RW Cep is in both size and temperature very similar to μ Cep. Both stars also show long-term periodic variability in their light curves: Kravchenko et al. (2019) cite 800-day and 4400-day periods for μ Cep, and Anugu et al. (2024a) find 400-day and 2500-day periods for RW Cep. Thus, it would be expected that the movement of its giant convective cells (as seen in interferometry by Anugu et al., 2024a; Anugu et al., 2023) would be revealed in its radial velocity field similarly to how we see it in μ Cep. However, we do not see such atmospheric turn-over activity in RW Cep.

5.3.7. Emission in resonance lines

In 1956, Merrill and Wilson found several strong resonance lines with two absorption components, separated by a central maximum (e.g. Ca I, Cr I, Mn I, Sr II, Ti I). They marked that the lines were very asymmetrical and that the central maximum was very narrow, possibly originating from a superimposed emission. The mean velocity of the central maximum over 42 lines was at -59.2 km s^{-1} . Gahm & Hultqvist (1972) found a central emission component in Na I D line doublet with a mean velocity of -62 km s^{-1} , in good agreement with Merrill & Wilson (1956), indicating that the physical processes behind the line profiles were similar in 1955 and 1969, when the individual authors took their observations.

Josselin & Plez (2007) attribute the line doubling to ascending and descending gas in a small number of giant convective cells. The velocity dispersion would cause the centre of the line profile to split. Lobel et al. (1998) described a visually similar splitting effect in low excitation ($E_{\text{low}} < 1.6 \text{ eV}$) metallic absorption line

cores in the spectrum of a YHG ρ Cas. However, for ρ Cas, the split profile shape is caused by the superposition of a static narrow emission upon a broad and strong absorption line. They gave as an example the profile of the Ba II $\lambda 6141.321$ resonance line ($E_{\text{low}} = 0.7040$ eV). This gives us here an opportunity to draw a direct parallel between RW Cep and ρ Cas.

In Fig. 5.10 panel 1, the Ba II profile in the spectrum of RW Cep looks quite similar to the profile seen in ρ Cas (cf. Fig. 13 in Lobel et al., 1998). The velocity of the central emission peak stays constant in time, while the intensities of the blue and red absorption wings vary. The other line of the doublet at $\lambda 6496$ is also visible and has a very similar profile shape.

In panel 2, we have drawn the Ca I resonance line ($E_{\text{low}} = 0.0$ eV) profiles at same epochs. The Ca I line shows a very similar two-bottom profile shape. The intensities of the absorption components vary more significantly than in Ba II, the red component almost disappears in 2006, while the blue component strengthens. The emission peak in the Ca I line has the same velocity as in Ba II line, at approximately -56 km s $^{-1}$.

During the January brightness minimum, the blue wings of both lines have almost completely disappeared, most likely due to the added blue-shifted emission. The emission completely fills the line wing, leaving only a small nook near -60 km s $^{-1}$ to mark the absorption component. The emission strength has decreased by September, when we see a deeper line profile.

In panels 3 and 4, we plot the K I $\lambda 7698$ and Na I D $_2$ $\lambda 5895.92$ lines. The profiles of these lines are complex, they are not blended with other metal lines, but some absorption components have an interstellar origin. There is also a notable telluric blend for K I at around -95 km s $^{-1}$. The central emission components in K I and Na I are located at the same velocity as in the Ba II and the Ca I lines. In K I, the emission reaches approximately 10% above the continuum level. This excludes the possibility that the central emission feature appears due to a superposition of two absorption components with different velocities. Two absorption lines could not form a central feature that would rise above the continuum level.

In addition to increasing in strength, the emission gained a flat-topped shape during the brightness minimum (January 2023). In the subsequent months, its strength decreased, but the shape remained the same (cf. September 2023). Asymmetric emission shape during the dimming period can be seen in the Ba II and the Ca I lines as well. The shape of the central emission line forms in a complex interplay of the circumstellar absorption we see during the calm period and the added processes during the dimming: both emission and enhanced absorption. The combination of these would result in the flat-topped shape of the emission line. The enhanced absorption would cause the emission to weaken by September compared to the calm period (as seen in K I and Na I D lines).

The velocity of the emission components remains remarkably stable in time, even during the Great Dimming. This implies a similar emission origin, as in the case of ρ Cas – a stable and cooler static envelope (Lobel et al., 1998). Interfer-

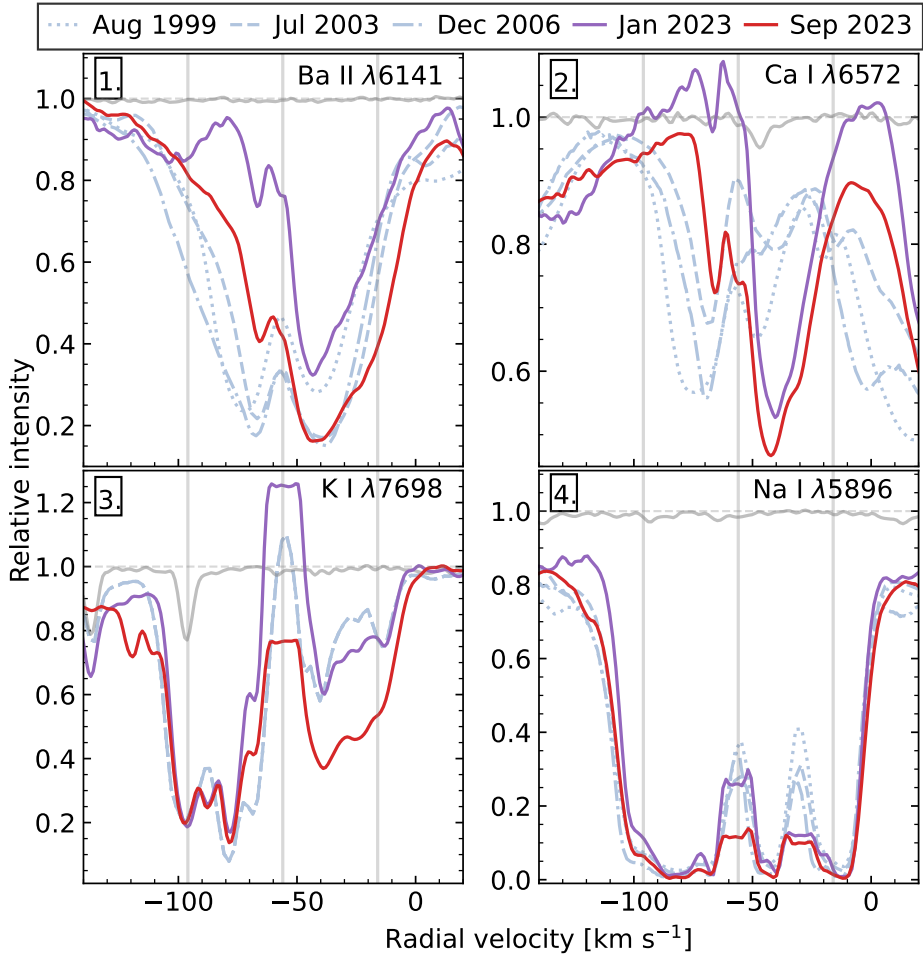


Figure 5.10: Selection of resonance lines in the spectrum of RW Cep. Panels 1-4: Ba II $\lambda 6141.71$, Ca I $\lambda 6572.78$, K I $\lambda 7698.96$, and Na I D₂ $\lambda 5895.92$. Thin blue lines show the line profiles in August 1999 (dotted, ELODIE), July 2003 (dashed, ELODIE), and December 2006 (dash-dotted, ESPaDOnS) and profiles during the dimming minimum are drawn in solid lines: January 2023 (purple, FIES) and 9 months later in September 2023 (red, FIES). Additionally, a telluric standard spectrum from the same January 2023 night has been included (light grey) to display the locations of blending telluric lines, especially in K I. For the K I only ESPaDOnS and FIES spectra are displayed due to the limited spectral range of ELODIE. Grey vertical lines trace the location of the emission peak at -56 km s^{-1} and also at $\pm 40 \text{ km s}^{-1}$ from it to help guide the eye.

ometric observations show the vast atmosphere and historical light curves show evidence of multiple previous mass-loss outbursts (Anugu et al., 2024a; Jones et al., 2023). This creates an environment of cool and diffuse gas surrounding the star – its upper atmospheric layers transition smoothly to circumstellar matter. Similar split line profiles of strong absorption lines that are composed of atmospheric and circumstellar components have been found in AGB stars (Klochkova, 2014).

5.4. Summary of results

We have presented a high temporal cadence spectroscopic time series that covers the variability of RW Cep from the brightness minimum of the Great Dimming and its return to near-normal levels. During the dimming, the H α line gained a strong emission component that was displaced slightly towards the blue wing. It reached its maximum strength during the dimming minimum and declined in intensity following that.

The atmosphere of RW Cep has a velocity gradient of $\sim 10\text{--}20\text{ km s}^{-1}$. The gradient remained stable in time throughout 1999–2006 and increased during the Great Dimming. There is a correlation that stronger lines have higher v_{rad} values and weaker lines have lower v_{rad} values, which corresponds to the motions inside giant convective cells. We observe that atmospheric stratification in radial velocities has remained stable over all the observations in the last 25 years. We measured the v_{sys} of the star at -50.3 km s^{-1} .

The radial velocity curve during the dimming reveals different behaviour for spectral lines of different strengths. The strongest lines have a radial velocity maximum during the dimming minimum from December 2023 to January 2023, while the radial velocity of the weaker lines changes only slightly or not at all in the case of Si II. The likely cause for this is the added emission, which is blue-shifted. This results in the absorption component shifting redwards to higher velocities. The Si II line forms deeper in the atmosphere and thus is not affected by the emission or the radial velocity changes at that time. The decrease in the line depth of Si II and weaker Fe I lines could be caused by the $\sim 300\text{ K}$ decrease in T_{eff} during the Great Dimming.

All of our studied spectral lines have a radial velocity maximum approximately six months after the dimming minimum, in May–June 2023, when their velocities are $\sim 10\text{ km s}^{-1}$ higher than in the pre-dimming period. By then, the emission strength had greatly decreased (to below half of its maximum value based on H α profiles), so it probably had a minor influence on the radial velocity changes. This radial velocity variability shows large-scale motions in the atmosphere of the star. Lines that are formed deeper in the atmosphere show a faster return to normal radial velocity values, while the lines that formed at higher atmospheric layers remained displaced for a longer period of time.

More information about the circumstellar environment of RW Cep was revealed by the central emission component that splits the cores of strong resonance lines

(e.g. Ca I, Ba II, K I, and Na I D lines). The above-continuum height of the emission peak in the K I line in December 2006 and its velocity stability over time imply its circumstellar origin. It is the only spectroscopic feature in the spectrum of RW Cep that holds a stable velocity over time, at -56 km s^{-1} .

In Betelgeuse, the surface mass ejection was triggered by outward-directed photospheric motion and shocks (Dupree et al., 2022). However, for RW Cep in September 2021, the measured v_{rad} values of H α and other lines (discussed in the following sections) remained within the normal range, so if any outburst activity took place in 2021, then either it did not significantly disrupt the stellar atmosphere, or it was localised to the other side of the star and is thus not visible in our v_{rad} measurements. Within the next year, the gas and dust cloud came further into our line of sight and, by the time of the brightness minimum, shielded the largest percentage of the stellar surface (as can be seen in interferometric images by Anugu et al., 2023) and the emission in H α reached its maximum strength. Following the dimming minimum, the cloud either dispersed or moved out of the line of sight, resulting in a smooth increase of the star's brightness and, accordingly, a decrease in H α emission strength.

6. CONCLUSIONS

A homogeneous characterisation of YSGs and YHG is needed to establish trends in mass-loss, variability, and evolutionary status. As a first step toward a population-level study of YSGs and YHG in the Milky Way, we determined their cluster and OB association memberships to study their stellar environments. This allowed us to improve the distance estimates for 28 stars out of the 35 stars in our sample. We found that 15 of the 20 YSGs are affiliated with clusters or OB associations, whereas the environments of YHG are more varied – clusters or OB associations (5 stars), star-forming region (1 star), and no detected affiliation (4 stars). We found no clear evidence of dynamical ejections, but a ‘walkaway’ scenario remains plausible for some objects.

We investigated two prominent hypergiants in different evolutionary phases: V509 Cas appears to be approaching the end of its YHG phase, while RW Cep may be on the path to become a YHG.

V509 Cas has been stable near the high-temperature border of the YEV at ~ 7900 K for 25 years. Long-term photometric and spectroscopic monitoring of the star shows quiescent atmospheric pulsations with amplitude in $T_{\text{eff}} \sim 200$ K, in V -filter brightness ~ 0.05 mag, and in $v_{\text{rad}} \sim 10$ km s $^{-1}$ on timescales of 100-200 days. The pulsational behaviour resembles ρ Cas with $\sim 1/4$ period phase lag between the radial velocity and brightness.

RW Cep shows variability consistent with large-scale convective motions expected for a red hypergiant. During the Great Dimming, the kinematics of its upper atmosphere changed, with a peak in radial velocity around six months after the brightness minimum. Blue-shifted emission from the cooling ejected gas filled in the $H\alpha$ absorption and appeared in other low-energy and resonance lines. The appearance of the $H\alpha$ emission resembled ρ Cas during its outburst (Lobel et al., 2003a), but we did not detect TiO absorption bands. Interferometry revealed decreased flux on the western hemisphere of the star (Anugu et al., 2023), consistent with dust formation and our spectroscopic observations.

The circumstellar environments of V509 Cas and RW Cep have similarities with other evolved massive stars, reflecting similar mass-loss history. The central emission components in the resonance lines of RW Cep indicate the presence of a circumstellar shell, akin to the structure surrounding ρ Cas (Lobel et al., 1998). The forbidden lines in V509 Cas indicate disc-like circumstellar geometry, such as the decretion discs of B[e]SG stars, also found in YHG ρ Cas and IRC +10420 (Aret et al., 2017c). Although two objects are insufficient for broad generalisations, RW Cep and V509 Cas may represent different states in YHG evolution.

The upcoming *Gaia* Data Release 4 will improve the astrometric measurements and enable further studies of massive-star populations. Multi-wavelength spectroscopic and interferometric surveys of Galactic YSGs and YHG would be valuable to homogeneously determine the stellar parameters, better constrain the radii and luminosities, identify binaries, and study the circumstellar environments.

REFERENCES

- Aadland, E., Massey, P., Neugent, K. F., and Drout, M. R. (2018). *Shedding Light on the Isolation of Luminous Blue Variables*. AJ 156.6, p. 294.
- Achmad, L., Lamers, H. J. G. L. M., Nieuwenhuijzen, H., and van Genderen, A. M. (1992). *A Photometric Study of the GO-41a+ Hypergiant HD 96918 (V382 Carinae)*. A&A 259, pp. 600–606.
- Adams, S. M., Kochanek, C. S., Gerke, J. R., Stanek, K. Z., and Dai, X. (2017). *The Search for Failed Supernovae with the Large Binocular Telescope: Confirmation of a Disappearing Star*. MNRAS 468.4, pp. 4968–4981.
- Adams, W. S., Joy, A. H., Humason, M. L., and Brayton, A. M. (1935). *The Spectroscopic Absolute Magnitudes and Parallaxes of 4179 Stars*. ApJ 81, p. 187.
- Aldering, G., Humphreys, R. M., and Richmond, M. (1994). *SN 1993J: The Optical Properties of Its Progenitor*. AJ 107, p. 662.
- Allen, D. A., and Swings, J. P. (1976). *The Spectra of Peculiar Be Star with Infrared Excesses*. A&A 47, pp. 293–302.
- Anderson, E., and Francis, C. (2012). *VizieR Online Data Catalog: Extended Hipparcos Compilation (XHIP)*. VizieR Online Data Catalog 5137, V/137B.
- Andrews, J. P. (1977). *HR 6392: A Double Star with Very High Luminosities*. MNRAS 178, pp. 131–136.
- Antoni, A., and Quataert, E. (2023). *Numerical Simulations of the Random Angular Momentum in Convection - II. Delayed Explosions of Red Supergiants Following 'failed' Supernovae*. MNRAS 525, pp. 1229–1245.
- Antoniadis, K., Bonanos, A. Z., de Wit, S., Zapartas, E., Munoz-Sanchez, G., et al. (2024). *Establishing a Mass-Loss Rate Relation for Red Supergiants in the Large Magellanic Cloud*. A&A 686, A88.
- Anugu, N., Baron, F., Monnier, J. D., Gies, D. R., Roettenbacher, R. M., et al. (2024a). *CHARA Near-infrared Imaging of the Yellow Hypergiant Star Rho Cassiopeiae: Convection Cells and Circumstellar Envelope*. ApJ 974, p. 113.
- Anugu, N., Baron, F., Gies, D. R., Lanthermann, C., Schaefer, G. H., et al. (2023). *The Great Dimming of the Hypergiant Star RW Cephei: CHARA Array Images and Spectral Analysis*. AJ 166, p. 78.
- Anugu, N., Gies, D. R., Roettenbacher, R. M., Monnier, J. D., Montargés, M., et al. (2024b). *Time Evolution Images of the Hypergiant RW Cephei during the Rebrightening Phase Following the Great Dimming*. ApJ 973, p. L5.
- Aret, A., Kolka, I., Kraus, M., and Maravelias, G. (2017a). *Similarities in the Structure of the Circumstellar Environments of B[e] Supergiants and Yellow Hypergiants*. In: *The B[e] Phenomenon: Forty Years of Studies*. Ed. by A. Miroshnichenko, S. Zharikov, D. Korčáková, and M. Wolf. ASP Conference Series, Vol. 508. Astronomical Society of the Pacific.
- Aret, A., Kraus, M., Kolka, I., and Maravelias, G. (2017b). *A New Outburst of the Yellow Hypergiant Star ρ Cas*. In: *The B[e] Phenomenon: Forty Years of Studies*. Ed. by A. Miroshnichenko, S. Zharikov, D. Korčáková, and M. Wolf. ASP Conference Series, Vol. 508. Astronomical Society of the Pacific, p. 357.
- Aret, A., Kraus, M., Kolka, I., and Maravelias, G. (2017c). *The Yellow Hypergiant - B[e] Supergiant Connection*. In: *Stars: From Collapse to Collapse*. Ed. by Y. Y. Balega, D. O. Kudryavtsev, I. I. Romanyuk, and I. A. Yakunin. Vol. 510. Astronomical Society of the Pacific.

- Aret, A., Kraus, M., Muratore, M. F., and Borges Fernandes, M. (2012). *A New Observational Tracer for High-Density Disc-like Structures around B[e] Supergiants*. MNRAS 423.1, pp. 284–293.
- El-Badry, K. (2025). *How to Use Gaia Parallaxes for Stars with Poor Astrometric Fits*. The Open Journal of Astrophysics 8, p. 62.
- Bailer-Jones, C. A. L., Rybizki, J., Fouesneau, M., Demleitner, M., and Andrae, R. (2021). *Estimating Distances from Parallaxes. V. Geometric and Photogeometric Distances to 1.47 Billion Stars in Gaia Early Data Release 3*. AJ 161, p. 147.
- Balona, L. A. (1982). *Radial Velocity Observations of Yellow Supergiants*. MNRAS 201, pp. 105–110.
- Baranne, A., Queloz, D., Mayor, M., Adrianzyk, G., Knispel, G., et al. (1996). *ELODIE: A Spectrograph for Accurate Radial Velocity Measurements*. A&AS 119, pp. 373–390.
- Beasor, E. R., Davies, B., Smith, N., van Loon, J. T., Gehrz, R. D., et al. (2020). *A New Mass-Loss Rate Prescription for Red Supergiants*. MNRAS 492.4, pp. 5994–6006.
- Beasor, E. R., Davies, B., Smith, N., van Loon, J. T., Gehrz, R. D., et al. (2023). *Correction to: 'A New Mass-Loss Rate Prescription for Red Supergiants'*. MNRAS 524, pp. 2460–2462.
- Beasor, E. R., Hosseinzadeh, G., Smith, N., Davies, B., Jencson, J. E., et al. (2024). *JWST Reveals a Luminous Infrared Source at the Position of the Failed Supernova Candidate N6946-BH1*. ApJ 964.2, p. 171.
- Beasor, E. R., Smith, N., and Jencson, J. E. (2025). *The Red Supergiant Progenitor Luminosity Problem*. ApJ 979.2, p. 117.
- Beasor, E. R., Smith, N., Pearson, J., Subrayan, B., Berger, E., et al. (2026). *The Fate of the Failed Supernova Candidate M31-2014-DS1*. MNRAS 546, p. 52.
- Bekhti, N. B., Flöer, L., Keller, R., Kerp, J., Lenz, D., et al. (2016). *HI4PI: A Full-Sky HI Survey Based on EBHIS and GASS*. A&A 594, A116.
- Bottlinger, C. F. (1911). *Die Bahn Des Spektroskopischen Doppelsternes α Orionis*. Astron. Nachr. 187, p. 33.
- Bourges, L., Mella, G., Lafrasse, S., Duvert, G., Chelli, A., et al. (2017). *VizieR Online Data Catalog: JMMC Stellar Diameters Catalogue - JSDC. Version 2*. VizieR Online Data Catalog 2346, pp. II/346.
- Bourgés, L., Lafrasse, S., Mella, G., Chesneau, O., Bouquin, J. L., et al. (2014). *The JMMC Stellar Diameters Catalog v2 (JSDC): A New Release Based on SearchCal Improvements*. In: *ASP Conference Series*. Vol. 485. Hawaii, USA, p. 223.
- Boyarchuk, A. A., Boyarchuk, M. E., and Petrov, P. P. (1988a). *Spectral Variability of the Supergiant ρ Cas in 1985 - 86*. In: *Proceedings of the 6th Soviet-Finnish Astronomical Meeting*. Ed. by U. Hänni, and I. Tuominen, p. 40.
- Boyarchuk, A. A., Gubeny, I., Kubat, I., Lyubimkov, L. S., and Sakhbullin, N. A. (1988b). *Effects of Deviation from Local Thermodynamic Equilibrium in the Atmosphere of F Supergiants - Part Three - Analysis of NAI Lines - Results of Calculations*. Astrophysics 28, pp. 202–208.
- Burki, G., and Mayor, M. (1983). *Nineteen New Spectroscopic Binaries and the Rate of Binary Stars among F-M Supergiants*. A&A 124, pp. 256–266.
- Campillay, A. R., Arias, J. I., Barbá, R. H., Morrell, N. I., Gamen, R. C., et al. (2019). *Spectroscopic Study of the Extremely Young O-type Triple System Herschel 36 A in the Hourglass Nebula - I. Orbital Properties*. MNRAS 484, pp. 2137–2147.
- Cannon, A. J., and Pickering, E. C. (1993). *VizieR Online Data Catalog: Henry Draper Catalogue and Extension 1918-1924*. VizieR Online Data Catalog 3135, III/135A.

- Cantat-Gaudin, T., and Brandt, T. D. (2021). *Characterizing and Correcting the Proper Motion Bias of the Bright Gaia EDR3 Sources*. A&A 649, A124.
- Carretero-Castrillo, M., Benaglia, P., Paredes, J. M., and Ribó, M. (2025). *New Stellar Bow Shocks and Bubbles Found around Runaway Stars*. A&A 694, A250.
- Carretero-Castrillo, M., Ribó, M., and Paredes, J. M. (2023). *Galactic Runaway O and Be Stars Found Using Gaia DR3*. A&A 679, A109.
- Castro-Carrizo, A., Quintana-Lacaci, G., Bujarrabal, V., Neri, R., and Alcolea, J. (2007). *Arcsecond-Resolution 12CO Mapping of the Yellow Hypergiants IRC +10420 and AFGL 2343*. A&A 465, pp. 457–467.
- Castro-Ginard, A., McMillan, P. J., Luri, X., Jordi, C., Romero-Gómez, M., et al. (2021). *Milky Way Spiral Arms from Open Clusters in Gaia EDR3*. A&A 652, A162.
- Castro-Ginard, A., Penoyre, Z., Casey, A. R., Brown, A. G. A., Belokurov, V., et al. (2024). *Gaia DR3 Detectability of Unresolved Binary Systems*. A&A 688, A1.
- Chelli, A., Duvert, G., Bourguès, L., Mella, G., Lafrasse, S., et al. (2016). *Pseudomagnitudes and Differential Surface Brightness: Application to the Apparent Diameter of Stars*. A&A 589, A112.
- Chemel, A. A., de Grijs, R., Glushkova, E. V., and Dambis, A. K. (2022). *Search for OB Associations in Gaia Early Data Release 3*. MNRAS 515, pp. 4359–4370.
- Chesneau, O., Meilland, A., Chapellier, E., Millour, F., van Genderen, A. M., et al. (2014). *The Yellow Hypergiant HR 5171 A: Resolving a Massive Interacting Binary in the Common Envelope Phase*. A&A 563, A71.
- Chiavassa, A., Pasquato, E., Jorissen, A., Sacuto, S., Babusiaux, C., et al. (2011). *Radiative Hydrodynamic Simulations of Red Supergiant Stars - III. Spectro-photocentric Variability, Photometric Variability, and Consequences on Gaia Measurements*. A&A 528, A120.
- Chinarova, L. L., and Andronov, I. L. (2000). *Catalogue of Main Characteristics of Pulsations of 173 Semi-Regular Stars*. Odessa Astronomical Publications 13, pp. 116–176.
- Chiosi, C., and Maeder, A. (1986). *The Evolution of Massive Stars with Mass Loss*. ARA&A 24, pp. 329–375.
- Clark, J. S., Negueruela, I., and González-Fernández, C. (2014). *IRAS 18357-0604 - an Analogue of the Galactic Yellow Hypergiant IRC +10420?* A&A 561, A15.
- Conti, P. S. (1975). *On the Relationship between Of and WR Stars*. Memoires of the Societe Royale des Sciences de Liege 9, pp. 193–212.
- Crockett, R. M., Eldridge, J. J., Smartt, S. J., Pastorello, A., Gal-Yam, A., et al. (2008). *The Type IIb SN 2008ax: The Nature of the Progenitor*. MNRAS 391, pp. L5–L9.
- Dai, M., Wang, S., and Jiang, B. (2025). *The Binary Fraction of Red Supergiants in the Magellanic Clouds*. Mon Not R Astron Soc 539.2, pp. 1220–1235.
- Davies, B., Figer, D. F., Law, C. J., Kudritzki, R.-P., Najarro, F., et al. (2008). *The Cool Supergiant Population of the Massive Young Star Cluster RSGC1*. ApJ 676.2, p. 1016.
- Davies, B., Oudmaijer, R. D., and Sahu, K. C. (2007). *Integral-Field Spectroscopy of the Post-Red Supergiant IRC +10420: Evidence for an Axisymmetric Wind*. ApJ 671, pp. 2059–2067.
- Davies, B., and Beasor, E. R. (2018). *The Initial Masses of the Red Supergiant Progenitors to Type II Supernovae*. MNRAS 474.2, pp. 2116–2128.
- Davies, B., Crowther, P. A., and Beasor, E. R. (2018). *The Luminosities of Cool Supergiants in the Magellanic Clouds, and the Humphreys–Davidson Limit Revisited*. MNRAS 478.3, pp. 3138–3148.

- Davies, B., Origlia, L., Kudritzki, R.-P., Figer, D. F., Rich, R. M., et al. (2009). *Chemical Abundance Patterns in the Inner Galaxy: The Scutum Red Supergiant Clusters*. *ApJ* 696.2, p. 2014.
- De, K., MacLeod, M., Jencson, J. E., Lovegrove, E., Antoni, A., et al. (2026). *Disappearance of a Massive Star in the Andromeda Galaxy Due to Formation of a Black Hole*. *Science* 391.6786, pp. 689–693.
- de Jager, C. (1980). *The Brightest Stars*. Geophysics and Astrophysics Monographs.
- de Jager, C. (1998). *The Yellow Hypergiants*. *A&AR* 8, pp. 145–180.
- de Jager, C., de Koter, A., Carpay, J., and Nieuwenhuijzen, H. (1991). *The Atmospheric Motion Field in Super- and Hypergiants*. *A&A* 244, p. 131.
- de Jager, C., Lobel, A., and Israelian, G. (1997). *Turbulence, Mass Loss and H α Emission by Stochastic Shocks in the Hypergiant ρ Cassiopeiae*. *A&A* 325, pp. 714–724.
- de Jager, C., Nieuwenhuijzen, H., and van der Hucht, K. A. (1988). *Mass Loss Rates in the Hertzsprung-Russell Diagram*. *A&AS* 72, pp. 259–289.
- de Jager, C., and Nieuwenhuijzen, H. (1997). *An Obstacle to the Late Evolution of Massive Stars*. *MNRAS* 290, pp. L50–L54.
- Delgado, A. J., Djupvik, A. A., Costado, M. T., and Alfaro, E. J. (2013). *Berkeley 94 and Berkeley 96: Two Young Clusters with Different Dynamical Evolution*. *MNRAS* 435.1, pp. 429–439.
- Deman, J. A., and Oey, M. S. (2024). *Kinematic Insights into Luminous Blue Variables and B[e] Supergiants*. *ApJ* 976, p. 125.
- Dharmawardena, T. E., Mairs, S., Scicluna, P., Bell, G., McDonald, I., et al. (2020). *Betelgeuse Fainter in the Submillimeter Too: An Analysis of JCMT and APEX Monitoring during the Recent Optical Minimum*. *ApJ* 897, p. L9.
- Donati, J.-F., Semel, M., Carter, B. D., Rees, D. E., and Collier Cameron, A. (1997). *Spectropolarimetric Observations of Active Stars*. *MNRAS* 291, pp. 658–682.
- Dorda, R., and Patrick, L. R. (2021). *Multiplicity among the Cool Supergiants in the Magellanic Clouds*. *MNRAS* 502, pp. 4890–4902.
- Dorigo Jones, J., Oey, M. S., Paggeot, K., Castro, N., and Moe, M. (2020). *Runaway OB Stars in the Small Magellanic Cloud: Dynamical versus Supernova Ejections*. *ApJ* 903, p. 43.
- Dorn-Wallenstein, T. Z., Chen, K. M., Wu, S. C., Goldberg, J. A., O’Grady, A. J. G., et al. (2025). *A Spectroscopic Hunt for Post-Red Supergiants in the Large Magellanic Cloud II: Turbulent Line Broadening in the Spectra of LMC Yellow Supergiants*. *ApJ* 991, p. 173.
- Dorn-Wallenstein, T. Z., Levesque, E. M., Neugent, K. F., Davenport, J. R. A., Morris, B. M., et al. (2020). *Short-Term Variability of Evolved Massive Stars with TESS. II. A New Class of Cool, Pulsating Supergiants*. *ApJ* 902, p. 24.
- Dorn-Wallenstein, T. Z., Levesque, E. M., and Davenport, J. R. A. (2019). *Short-Term Variability of Evolved Massive Stars with TESS*. *ApJ* 878, p. 155.
- Drout, M. R., Massey, P., and Meynet, G. (2012). *The Yellow and Red Supergiants of M33*. *ApJ* 750, p. 97.
- Drout, M. R., Massey, P., Meynet, G., Tokarz, S., and Caldwell, N. (2009). *Yellow Supergiants in the Andromeda Galaxy (M31)*. *ApJ* 703, pp. 441–460.
- Dupree, A. K., and Montargès, M. (2025). *Betelgeuse, the Prototypical Red Supergiant*. *Galaxies* 13.3, p. 50.

- Dupree, A. K., Strassmeier, K. G., Calderwood, T., Granzer, T., Weber, M., et al. (2022). *The Great Dimming of Betelgeuse: A Surface Mass Ejection and Its Consequences*. *ApJ* 936, p. 18.
- Dwarkadas, V. V. (2014). *On the Lack of X-ray Bright Type IIP Supernovae*. *MNRAS* 440, pp. 1917–1924.
- Ekström, S., Georgy, C., Eggenberger, P., Meynet, G., Mowlavi, N., et al. (2012). *Grids of Stellar Models with Rotation. I. Models from 0.8 to 120 M₀ at Solar Metallicity (Z = 0.014)*. *A&A* 537, A146.
- Ekström, S., and Georgy, C. (2025). *Stellar Evolution Through the Red Supergiant Phase*. *Galaxies* 13, p. 81.
- Elias-Rosa, N., Van Dyk, S. D., Li, W., Miller, A. A., Silverman, J. M., et al. (2010). *The Massive Progenitor of the Type II-linear Supernova 2009kr*. *ApJ* 714, pp. L254–L259.
- Elias-Rosa, N., Van Dyk, S. D., Li, W., Morrell, N., Gonzalez, S., et al. (2009). *On the Progenitor of the Type II-Plateau SN 2008cn in NGC 4603*. *ApJ* 706, pp. 1174–1183.
- ESA (1997). *The HIPPARCOS and TYCHO Catalogues. Astrometric and Photometric Star Catalogues Derived from the ESA HIPPARCOS Space Astrometry Mission*. ESA Special Publication 1200.
- Fabricius, C., Luri, X., Arenou, F., Babusiaux, C., Helmi, A., et al. (2021). *Gaia Early Data Release 3. Catalogue Validation*. *A&A* 649, A5.
- Fadeyev, Y. A. (2011). *Pulsational Instability of Yellow Hypergiants*. *Astronomy Letters* 37, pp. 403–413.
- Fang, Q., Moriya, T. J., and Maeda, K. (2025). *Red Supergiant Problem Viewed from the Nebular Phase Spectroscopy of Type II Supernovae*. *ApJ* 986.1, p. 39.
- Feast, M. W., and Thackeray, A. D. (1956). *Red Supergiants in the Large Magellanic Cloud*. *MNRAS* 116, p. 587.
- Figier, D. F., MacKenty, J. W., Robberto, M., Smith, K., Najarro, F., et al. (2006). *Discovery of an Extraordinarily Massive Cluster of Red Supergiants*. *ApJ* 643, pp. 1166–1179.
- Filippenko, A. V. (1997). *Optical Spectra of Supernovae*. *ARA&A* 35, pp. 309–355.
- Filippenko, A. V. (2005). *Supernovae and Their Massive Star Progenitors*. In: *The Fate of the Most Massive Stars*. Ed. by R. Humphreys, and K. Stanek. ASP Conference Series, Vol. 332. Astronomical Society of the Pacific.
- Fitton, S., Tofflemire, B. M., and Kraus, A. L. (2022). *Disk Material Inflates Gaia RUWE Values in Single Stars*. *Res. Notes AAS* 6, p. 18.
- Fitzgerald, M. P., Boudreault, R., Fich, M., Luiken, M., and Witt, A. N. (1979). *The Open Clusters Pismis 6 and 8, and Wat 6*. *A&AS* 37, pp. 351–360.
- Fletcher, E. S. (1963). *Model-Independent Correlation of Stars and Neutral Hydrogen*. *AJ* 68, p. 407.
- Folsom, C. P., Kama, M., Eenmäe, T., Kolka, I., Aret, A., et al. (2022). *A Rare Phosphorus-Rich Star in an Eclipsing Binary from TESS*. *A&A* 658, A105.
- Froebrich, D., Schmeja, S., Samuel, D., and Lucas, P. W. (2010). *Old Star Clusters in the FSR Catalogue*. *MNRAS* 409.3, pp. 1281–1288.
- Fukue, K., Matsunaga, N., Yamamoto, R., Kondo, S., Kobayashi, N., et al. (2015). *Line-Depth Ratios in H-band Spectra to Determine Effective Temperatures of G- and K-type Giants and Supergiants*. *ApJ* 812, p. 64.
- Gahm, G. F., and Hultqvist, L. (1972). *Spectral Properties of Luminous Late-Type Stars*. *A&A* 16, p. 329.
- Gaia Collaboration, Prusti, T., de Bruijne, J. H. J., Brown, A. G. A., Vallenari, A., et al. (2016). *The Gaia Mission*. *A&A* 595, A1.

- Gaia Collaboration, Vallenari, A., Brown, A. G. A., Prusti, T., de Bruijne, J. H. J., et al. (2023). *Gaia Data Release 3. Summary of the Content and Survey Properties*. A&A 674, A1.
- Georgy, C. (2012). *Yellow Supergiants as Supernova Progenitors: An Indication of Strong Mass Loss for Red Supergiants?* A&A 538, p. L8.
- Gerke, J. R., Kochanek, C. S., and Stanek, K. Z. (2015). *The Search for Failed Supernovae with the Large Binocular Telescope: First Candidates*. MNRAS 450.3, pp. 3289–3305.
- Glatzel, W., and Kraus, M. (2024). *Instabilities in the Yellow Hypergiant Domain*. MNRAS 529, pp. 4947–4957.
- Goldberg, J. A., Joyce, M., and Molnár, L. (2024). *A Buddy for Betelgeuse: Binarity as the Origin of the Long Secondary Period in α Orionis*. ApJ 977, p. 35.
- Gontcharov, G. A., Marchuk, A. A., Khovrichiev, M. Y., Mosenkov, A. V., Savchenko, S. S., et al. (2023). *New Interstellar Extinction Maps Based on Gaia and Other Sky Surveys*. Astronomy Letters 49, pp. 673–696.
- Gorlova, N., Lobel, A., Burgasser, A. J., Rieke, G. H., Ilyin, I., et al. (2006). *On the CO Near-Infrared Band and the Line-splitting Phenomenon in the Yellow Hypergiant Rho Cassiopeiae*. ApJ 651.2, p. 1130.
- Gray, D. F. (1994). *Spectral Line-Depth Ratios as Temperature Indicators for Cool Stars*. PASP 106, p. 1248.
- Gray, D. F. (2008). *Mass Motions in the Photosphere of Betelgeuse*. AJ 135, pp. 1450–1458.
- Gray, D. F. (2021). *The Observation and Analysis of Stellar Photospheres*. 4th ed. UK: Cambridge University Press.
- Gray, D. F., and Johanson, H. L. (1991). *Precise Measurement of Stellar Temperatures Using Line-Depth Ratios*. PASP 103, p. 439.
- Groh, J. H., Meynet, G., and Ekström, S. (2013). *Massive Star Evolution: Luminous Blue Variables as Unexpected Supernova Progenitors*. A&A 550, p. L7.
- Handberg, R., Lund, M. N., White, T. R., Hall, O. J., Buzasi, D. L., et al. (2021). *TESS Data for Asteroseismology: Photometry*. AJ 162, p. 170.
- Hanuschik, R. W. (2003). *A Flux-Calibrated, High-Resolution Atlas of Optical Sky Emission from UVES*. A&A 407, pp. 1157–1164.
- Harmer, D. L., Lawson, P. A., and Stickland, D. J. (1978). *The Spectrum of the G Supergiant HR 8752*. The Observatory 98, pp. 250–257.
- Harper, W. (1923). *The Radial Velocities of 125 Stars*. Publications of the Dominion Astrophysical Observatory Victoria 2, pp. 189–203.
- Hawkins, G. W., Skinner, C. J., Meixner, M. M., Jernigan, J. G., Arens, J. F., et al. (1995). *Discovery of an Extended Nebula around AFGL 2343 (HD 179821) at 10 Microns*. ApJ 452, p. 314.
- He, Z., Liu, X., Luo, Y., Wang, K., and Jiang, Q. (2023). *Unveiling Hidden Stellar Aggregates in the Milky Way: 1656 New Star Clusters Found in Gaia EDR3*. ApJS 264, p. 8.
- Healy, S., Horiuchi, S., Colomer Molla, M., Milisavljevic, D., Tseng, J., et al. (2024). *Red Supergiant Candidates for Multimessenger Monitoring of the next Galactic Supernova*. MNRAS 529.4, pp. 3630–3650.
- Howell, S. B., Ciardi, D. R., Clark, C. A., Hope, D. A., Littlefield, C., et al. (2025). *The Probable Direct-imaging Detection of the Stellar Companion to Betelgeuse*. ApJ 988, p. L47.

- Humphreys, R. M. (1970). *The Space Distribution and Kinematics of Supergiants*. AJ 75, pp. 602–623.
- Humphreys, R. M. (1978). *Studies of Luminous Stars in Nearby Galaxies. I. Supergiants and O Stars in the Milky Way*. ApJS 38, pp. 309–350.
- Humphreys, R. M., and Davidson, K. (1979). *Studies of Luminous Stars in Nearby Galaxies. III. Comments on the Evolution of the Most Massive Stars in the Milky Way and the Large Magellanic Cloud*. ApJ 232, pp. 409–420.
- Humphreys, R. M., Strecker, D. W., and Ney, E. P. (1971). *High-Luminosity G Supergiants*. ApJ 167, p. L35.
- Humphreys, R. M. (2019). *Comments on the Progenitor of NGC 6946-BH1*. Res. Notes AAS 3, p. 164.
- Humphreys, R. M., and Davidson, K. (1994). *The Luminous Blue Variables: Astrophysical Geysers*. PASP 106, p. 1025.
- Humphreys, R. M., Davidson, K., Richards, A. M. S., Ziurys, L. M., Jones, T. J., et al. (2021). *The Mass-loss History of the Red Hypergiant VY CMa*. AJ 161.3, p. 98.
- Humphreys, R. M., Davidson, K., and Smith, N. (2002). *Crossing the Yellow Void: Spatially Resolved Spectroscopy of the Post-Red Supergiant IRC +10420 and Its Circumstellar Ejecta*. AJ 124, pp. 1026–1044.
- Humphreys, R. M., Gordon, M. S., Martin, J. C., Weis, K., and Hahn, D. (2017). *Luminous and Variable Stars in M31 and M33. IV. Luminous Blue Variables, Candidate LBVs, B[e] Supergiants, and the Warm Hypergiants: How to Tell Them Apart*. ApJ 836, p. 64.
- Humphreys, R. M., Jones, T. J., and Gehrz, R. D. (1987). *The Enigmatic Object Variable A in M33*. AJ 94, p. 315.
- Humphreys, R. M., Stangl, S., Gordon, M. S., Davidson, K., and Grammer, S. H. (2019). *Luminous and Variable Stars in NGC 2403 and M81*. AJ 157, p. 22.
- Humphreys, R. M., Strecker, D. W., Murdock, T. L., and Low, F. J. (1973). *IRC+10420 - Another Eta Carinae?* ApJ 179, p. L49.
- Hunt, E. L., and Reffert, S. (2024). *Improving the Open Cluster Census. III. Using Cluster Masses, Radii, and Dynamics to Create a Cleaned Open Cluster Catalogue*. A&A 686, A42.
- Iben Jr., I. (1964). *The Surface Ratio of N14 to C12 during Helium Burning*. ApJ 140, p. 1631.
- Israelian, G., Lobel, A., and Schmidt, M. R. (1999). *The Yellow Hypergiants HR 8752 and ρ Cassiopeiae near the Evolutionary Border of Instability*. ApJ 523, pp. L145–L149.
- Jencson, J. E., Sand, D. J., Andrews, J. E., Smith, N., Pearson, J., et al. (2022). *An Exceptional Dimming Event for a Massive, Cool Supergiant in M51*. ApJ 930.1, p. 81.
- Jones, T. J., Humphreys, R. M., Gehrz, R. D., Lawrence, G. F., Zickgraf, F.-J., et al. (1993). *IRC +10420: A Cool Hypergiant near the Top of the H-R Diagram*. ApJ 411, p. 323.
- Jones, T. J., Shenoy, D., and Humphreys, R. (2023). *The Recent Mass Loss History of the Hypergiant RW Cep*. Res. notes AAS 7, p. 92.
- Josselin, E., and Plez, B. (2007). *Atmospheric Dynamics and the Mass Loss Process in Red Supergiant Stars*. A&A 469, pp. 671–680.
- Josselin, E., and Plez, B. (2003). *The Atmosphere of Red Supergiants*. Modelling of Stellar Atmospheres. Proceedings of the 210th Symposium of the International Astronomical Union 210. Ed. by N. Piskunov, W. W. Weiss, and D. F. Gray.
- Jura, M., and Werner, M. W. (1999). *The Detached Dust Shell around the Massive Star HD 179821*. ApJ 525, pp. 113–L116.

- Kasikov, A., Kolka, I., and Aret, A. (2022). *Following V509 Cas into the Void with FIES*. In: *NOT - A Telescope For the Future*, p. 14.
- Kastner, J. H., and Weintraub, D. A. (1995). *The Massive Post-Red Supergiants IRC +10420 and HD 179821*. *ApJ* 452, p. 833.
- Kee, N. D., Sundqvist, J. O., Decin, L., de Koter, A., and Sana, H. (2021). *Analytic, Dust-Independent Mass-Loss Rates for Red Supergiant Winds Initiated by Turbulent Pressure*. *A&A* 646, A180.
- Keenan, P. C. (1971). *Classification of Supergiants of Types G, K, and M*. Contributions from the Kitt Peak National Observatory 554, pp. 35–39.
- Keenan, P. C. (1942). *Luminosities of the M-Type Variables of Small Range*. *ApJ* 95, p. 461.
- Keenan, P. C., and McNeil, R. C. (1989). *The Perkins Catalog of Revised MK Types for the Cooler Stars*. *ApJS* 71, p. 245.
- Kholopov, P. N., Samus, N. N., Frolov, M. S., Goranskij, V. P., Gorynya, N. A., et al. (1998). *Combined General Catalogue of Variable Stars*. Combined General Catalogue of Variable Stars.
- Kienzle, F., Burki, G., Burnet, M., and Meynet, G. (1998). *The Pulsating Yellow Supergiant V810 Centauri*. *A&A* 337, pp. 779–789.
- Kilpatrick, C. D., Drout, M. R., Achettil, K., Dimitriadis, G., Foley, R. J., et al. (2021). *A Cool and Inflated Progenitor Candidate for the Type Ib Supernova 2019yvr at 2.6 Yr before Explosion*. *MNRAS* 504.2, pp. 2073–2093.
- Kilpatrick, C. D., Foley, R. J., Abramson, L. E., Pan, Y.-C., Lu, C.-X., et al. (2017). *On the Progenitor of the Type IIb Supernova 2016gkg*. *MNRAS* 465, pp. 4650–4657.
- Kippenhahn, R., and Weigert, A. (1990). *Stellar Structure and Evolution*.
- Klochkova, V. G. (2014). *Circumstellar Envelope Manifestations in the Optical Spectra of Evolved Stars*. *Astrophysical Bulletin* 69, pp. 279–295.
- Klochkova, V. G. (2019). *Unity and Diversity of Yellow Hypergiants Family*. *Astrophys. Bull.* 74.4, pp. 475–489.
- Klochkova, V. G., Chentsov, E. L., and Panchuk, V. E. (1997). *Optical Spectrum of the IR Source IRC+10420 in 1992-1996*. *MNRAS* 292, pp. 19–26.
- Kochanek, C. S., Beacom, J. F., Kistler, M. D., Prieto, J. L., Stanek, K. Z., et al. (2008). *A Survey About Nothing: Monitoring a Million Supergiants for Failed Supernovae*. *ApJ* 684, pp. 1336–1342.
- Kochanek, C. S., Neustadt, J. M. M., and Stanek, K. Z. (2024). *The Search for Failed Supernovae with the Large Binocular Telescope: The Mid-infrared Counterpart to N6946-BH1*. *ApJ* 962, p. 145.
- Koumpia, E., Oudmaijer, R. D., de Wit, W.-J., Mérand, A., Black, J. H., et al. (2022). *Tracing a Decade of Activity towards a Yellow Hypergiant. The Spectral and Spatial Morphology of IRC+10420 at Au Scales*. *MNRAS* 515.2, p. 2766.
- Koumpia, E., Oudmaijer, R. D., Graham, V., Banyard, G., Black, J. H., et al. (2020). *Optical and Near-Infrared Observations of the Fried Egg Nebula. Multiple Shell Ejections on a 100 Yr Timescale from a Massive Yellow Hypergiant*. *A&A* 635, A183.
- Kourniotis, M., Kraus, M., Arias, M. L., Cidale, L., and Torres, A. F. (2018). *On the Evolutionary State of Massive Stars in Transition Phases in M33*. *MNRAS* 480.3, pp. 3706–3717.
- Kourniotis, M., Kraus, M., Maryeva, O., Borges Fernandes, M., and Maravelias, G. (2022). *Revisiting the Evolved Hypergiants in the Magellanic Clouds*. *MNRAS* 511.3, pp. 4360–4376.

- Kourniotis, M., Bonanos, A. Z., Yuan, W., Macri, L. M., Garcia-Alvarez, D., et al. (2017). *Monitoring Luminous Yellow Massive Stars in M 33: New Yellow Hypergiant Candidates*. A&A 601, A76.
- Kourniotis, M., Kraus, M., Arias, M. L., and Cidale, L. S. (2025). *HD 144812: A Transition-Phase Massive Star in a Binary System*. MNRAS 540, pp. L28–L33.
- Kovtyukh, V. V. (2007). *High-Precision Effective Temperatures of 161 FGK Supergiants from Line-Depth Ratios*. MNRAS 378, pp. 617–624.
- Kovtyukh, V. V., Gorlova, N. I., and Belik, S. I. (2012). *Accurate Luminosities from the Oxygen 7771–4 Å Triplet and the Fundamental Parameters of F–G Supergiants*. MNRAS 423.4, pp. 3268–3273.
- Kraus, M. (2019). *A Census of B[e] Supergiants*. Galaxies 7, p. 83.
- Kraus, M., Borges Fernandes, M., and de Araújo, F. X. (2010). *Neutral Material around the B[e] Supergiant Star LHA 115-S 65. An Outflowing Disk or a Detached Keplerian Rotating Disk?* A&A 517, A30.
- Kraus, M., Kolka, I., Aret, A., Nickeler, D. H., Maravelias, G., et al. (2019). *A New Outburst of the Yellow Hypergiant Star ρ Cas*. MNRAS 483, pp. 3792–3809.
- Kraus, M., Kourniotis, M., Arias, M. L., Torres, A. F., and Nickeler, D. H. (2023). *Dense Molecular Environments of B[e] Supergiants and Yellow Hypergiants*. Galaxies 11, p. 76.
- Kravchenko, K., Chiavassa, A., Eck, S. V., Jorissen, A., Merle, T., et al. (2019). *Tomography of Cool Giant and Supergiant Star Atmospheres II. Signature of Convection in the Atmosphere of the Red Supergiant Star μ Cep*. A&A 632, A28.
- Kravchenko, K., Jorissen, A., Eck, S. V., Merle, T., Chiavassa, A., et al. (2021). *Atmosphere of Betelgeuse before and during the Great Dimming Event Revealed by Tomography*. A&A 650, p. L17.
- Lagadec, E., Zijlstra, A. A., Oudmaijer, R. D., Verhoelst, T., Cox, N. L. J., et al. (2011). *A Double Detached Shell around a Post-Red Supergiant: IRAS 17163-3907, the Fried Egg Nebula*. A&A 534, p. L10.
- Laher, R. R., Gorjian, V., Rebull, L. M., Masci, F. J., Fowler, J. W., et al. (2012). *Aperture Photometry Tool*. PASP 124, p. 737.
- Lambert, D. L., Hinkle, K. H., and Hall, D. N. B. (1981). *Circumstellar Shells of Luminous Supergiants. I. Carbon Monoxide in Rho CAS and HR 8752*. ApJ 248, pp. 638–650.
- Lambert, D. L., and Luck, R. E. (1978). *Spectrum Variations of the Superluminous Star HR 8752*. MNRAS 184, pp. 405–422.
- Lamers, H. J. G. L. M., de Groot, M., and Cassatella, A. (1983). *P Cygni Stars as an Intermediate Stage between Red Supergiants and Wolf-rayet Stars*. A&A 123, pp. L8–L10.
- Lamers, H. J. G. L. M., Zickgraf, F.-J., de Winter, D., Houziaux, L., and Zorec, J. (1998). *An Improved Classification of B[e]-Type Stars*. A&A 340, pp. 117–128.
- Leadbeater, R. (2023). *The 2022 Dimming of RW Cep - A First Look*. British Astronomical Association Variable Star Section Circular 195, pp. 7–12.
- Lee, U., Saio, H., and Osaki, Y. (1991). *Viscous Excretion Discs around Be Stars*. MNRAS 250, pp. 432–437.
- Levesque, E. M. (2017). *Astrophysics of Red Supergiants*. UK: IOP Publishing.
- Liimets, T., Kraus, M., Moiseev, A., Duronea, N., Cidale, L. S., et al. (2022). *Follow-Up of Extended Shells around B[e] Stars*. Galaxies 10, p. 41.

- Lindgren, L., Bastian, U., Biermann, M., Bombrun, A., de Torres, A., et al. (2021a). *Gaia Early Data Release 3. Parallax Bias versus Magnitude, Colour, and Position*. A&A 649, A4.
- Lindgren, L., Klioner, S. A., Hernández, J., Bombrun, A., Ramos-Lerate, M., et al. (2021b). *Gaia Early Data Release 3. The Astrometric Solution*. A&A 649, A2.
- Lobel, A. (2001). *On the Dynamic Stability of Cool Supergiant Atmospheres*. ApJ 558, pp. 780–801.
- Lobel, A., Achmad, L., de Jager, C., and Nieuwenhuijzen, H. (1992). *On the Instability Parameters of Stellar Atmospheres*. A&A 264, p. 147.
- Lobel, A., de Jager, C., Nieuwenhuijzen, H., Smolinski, J., and Gesicki, K. (1994). *Pulsation of the Yellow Hypergiant ρ Cassiopeiae in 1970*. A&A 291, pp. 226–238.
- Lobel, A., de Jager, K., and Nieuwenhuijzen, H. (2013). *Long-Term Spectroscopic Monitoring of Cool Hypergiants HR 8752, IRC+10420, and 6 Cas near the Yellow Evolutionary Void*. In: *ASP Conference Series*. Vol. 470. Noordwijkerhout, The Netherlands, p. 167.
- Lobel, A., Dupree, A. K., Stefanik, R. P., Torres, G., Israelian, G., et al. (2003a). *High-Resolution Spectroscopy of the Yellow Hypergiant ρ Cassiopeiae from 1993 through the Outburst of 2000-2001*. ApJ 583, pp. 923–954.
- Lobel, A., Dupree, A. K., Stefanik, R. P., Torres, G., Israelian, G., et al. (2003b). *The Millennium Outburst of the Cool Hypergiant Rho Cassiopeiae: Spectroscopy and Modeling*. In: *Modelling of Stellar Atmospheres*. Ed. by N. Piskunov, W. W. Weiss, and D. F. Gray. Proceedings of the IAU Symposium 210. Astronomical Society of the Pacific.
- Lobel, A., Israelian, G., de Jager, C., Musaev, F., Parker, J. W., et al. (1998). *The Spectral Variability of the Cool Hypergiant Rho Cassiopeiae*. A&A 330, pp. 659–675.
- Lobel, A., Royer, P., Martayan, C., Laverick, M., Merle, T., et al. (2019). *The Belgian Repository of Fundamental Atomic Data and Stellar Spectra (BRASS)*. Atoms 7, p. 105.
- Long, G., Song, H., Meynet, G., Maeder, A., Zhang, R., et al. (2022). *The Formation of the Stripped-envelope Type IIb Supernova Progenitors: Rotation, Metallicity, and Overshooting*. ApJS 262, p. 26.
- López Ariste, A., Wavasseur, M., Mathias, P., Lèbre, A., Tessore, B., et al. (2023). *The Height of Convective Plumes in the Red Supergiant μ Cep*. A&A 670, A62.
- Lovegrove, E., and Woosley, S. E. (2013). *Very Low Energy Supernovae from Neutrino Mass Loss*. ApJ 769, p. 109.
- Lovy, D., Maeder, A., Noels, A., and Gabriel, M. (1984). *Supergiant Variability : Theoretical Pulsation Periods and Comparison with Observations*. A&A 133, pp. 307–312.
- Lund, M. N., Handberg, R., Buzasi, D. L., Carboneau, L., Hall, O. J., et al. (2021). *TESS Data for Asteroseismology: Light-curve Systematics Correction*. ApJS 257, p. 53.
- MacLeod, M., Blunt, S., De Rosa, R. J., Dupree, A. K., Granzer, T., et al. (2025). *Radial Velocity and Astrometric Evidence for a Close Companion to Betelgeuse*. ApJ 978, p. 50.
- Maeder, A. (1992). *The p -Inversion and the Geyser Model for Supergiant Envelopes*. In: *Instabilities in Evolved Super- and Hypergiants*. Ed. by C. de Jager, and H. Nieuwenhuijzen. Proceedings of the International Colloquium, Amsterdam, p. 138.
- Maehara, H. (2014). *Automated Wide-field Survey for Transient Objects with a Small Telescope*. JAXA-RR-13-010, pp. 119–127.
- Maíz Apellániz, J., Barbá, R. H., Fariña, C., Sota, A., Pantaleoni González, M., et al. (2021a). *Lucky Spectroscopy, an Equivalent Technique to Lucky Imaging. II. Spa-*

- tially Resolved Intermediate-Resolution Blue-Violet Spectroscopy of 19 Close Massive Binaries Using the William Herschel Telescope.* A&A 646, A11.
- Maíz Apellániz, J., and Negueruela, I. (2025). *Barbá 2: A New Supergiant-Rich Galactic Stellar Cluster.* In: *Highlights of Spanish Astrophysics XII.* Ed. by M. Manteiga, F. González-Galindo, A. Labiano-Ortega, M. J. Martínez-González, N. Rea, et al. Proceedings of the XVI Scientific Meeting of the Spanish Astronomical Society. Granada, Spain, p. 224.
- Maíz Apellániz, J., Pantaleoni González, M., and Barbá, R. H. (2021b). *Validation of the Accuracy and Precision of Gaia EDR3 Parallaxes with Globular Clusters.* A&A 649, A13.
- Mantegazza, L. (1992). *Luminosities of Yellow Supergiants from Near-Infrared Spectra : Calibration through Magellanic Cloud Stars.* A&A 265, pp. 527–534.
- Marco, A., Negueruela, I., Castro, N., and Simón-Díaz, S. (2025). *NGC 663 as a Laboratory for Massive Star Evolution.* MNRAS 542, pp. 703–734.
- Marston, A. P., and McCollum, B. (2008). *Extended Shells around B[e] Stars. Implications for B[e] Star Evolution.* A&A 477, pp. 193–202.
- Martin, J. C., Humphreys, R. M., and Davidson, K. (2025). *On the Spatial Distribution of Luminous Blue Variables, B[e] Supergiants, and Wolf-Rayet Stars in the Large Magellanic Cloud.* ApJ 994, p. 159.
- Martin, J. C., and Humphreys, R. M. (2023). *A Census of the Most Luminous Stars. I. The Upper HR Diagram for the Large Magellanic Cloud.* AJ 166, p. 214.
- Matsunaga, N., Jian, M., Taniguchi, D., and Elgueta, S. S. (2021). *Line-Depth Ratios as Indicators of Effective Temperature and Surface Gravity.* MNRAS 506, pp. 1031–1044.
- Maund, J. R., Fraser, M., Ergon, M., Pastorello, A., Smartt, S. J., et al. (2011). *The Yellow Supergiant Progenitor of the Type II Supernova 2011dh in M51.* ApJ 739, p. L37.
- Maund, J. R., Fraser, M., Reilly, E., Ergon, M., and Mattila, S. (2015). *Whatever Happened to the Progenitors of Supernovae 2008cn, 2009kr and 2009md?* MNRAS 447.4, pp. 3207–3217.
- McClure-Griffiths, N. M., Stanimirović, S., and Rybczyk, D. R. (2023). *Atomic Hydrogen in the Milky Way: A Stepping Stone in the Evolution of Galaxies.* ARA&A 61, pp. 19–63.
- Mel’nik, A. M., and Dambis, A. K. (2017). *Kinematics of OB-associations in Gaia Epoch.* MNRAS 472, pp. 3887–3904.
- Merrill, P. W., and Wilson, O. C. (1956). *Complex Lines in the Spectrum of RW Cephei.* ApJ 123, p. 392.
- Meynet, G., Chomienne, V., Ekström, S., Georgy, C., Granada, A., et al. (2015). *Impact of Mass-Loss on the Evolution and Pre-Supernova Properties of Red Supergiants.* A&A 575, A60.
- Miroshnichenko, A. S. (2007). *Toward Understanding the B[e] Phenomenon. I. Definition of the Galactic FS CMa Stars.* ApJ 667, pp. 497–504.
- Miroshnichenko, A. S., Zharikov, S. V., Vaidman, N. L., and Khokhlov, S. A. (2025). *The B[e] Phenomenon in Supergiants. A Result of Mass Transfer in Binaries, Mergers, or What?* In: *Massive Stars Across Redshifts in the Era of JWST and Large-Scale Surveys.* Ed. by A. Wofford, N. St-Louis, M. Garcia, and S. Simón-Díaz. Proceedings of the IAU Symposium 402. Cambridge University Press.
- Monin, D., Saddlemyer, L., and Bohlender, D. (2014). *Robotic Operation of the DAO 1.2-m Telescope and McKellar Spectrograph.* In: *Revista Mexicana de Astronomía y Astrofísica Conference Series.* Vol. 45, p. 69.

- Montargès, M., Cannon, E., Lagadec, E., de Koter, A., Kervella, P., et al. (2021). *A Dusty Veil Shading Betelgeuse during Its Great Dimming*. *Nature* 594, pp. 365–368.
- Montargès, M., Chiavassa, A., Kervella, P., Ridgway, S. T., Perrin, G., et al. (2017). *The Convective Surface of the Red Supergiant Antares. VLT/PIONIER Interferometry in the near Infrared*. *A&A* 605, A108.
- Morgan, W. W., and Roman, N. G. (1950). *Revised Standards for Supergiants on the System of the Yerkes Spectral Atlas*. *ApJ* 112, pp. 362–364.
- Morris, P. W., Voors, R. H. M., Lamers, H. J. G. L. M., and Eenens, P. R. J. (1997). *Near-Infrared Spectra of LBV; Be and B[e] Stars: Does Axisymmetry Provide a Morphological Link?* In: *Luminous Blue Variables: Massive Stars in Transition*. Ed. by A. Nota, and H. J. G. L. M. Lamers. Vol. 120. ASP Conference Series; Vol. 120, p. 20.
- Moultaka, J., Ilovaisky, S., Prugniel, P., and Soubiran, C. (2004). *ELODIE-SOPHIE: Spectroscopic Archive*. In: *SF2A-2004: Semaine de l’Astrophysique Française*, p. 547.
- Munoz-Sanchez, G., de Wit, S., Bonanos, A. Z., Antoniadis, K., Boutsia, K., et al. (2024). *Episodic Mass Loss in the Very Luminous Red Supergiant [W60] B90 in the Large Magellanic Cloud*. *A&A* 690, A99.
- Muñoz-Sánchez, G., Kalitsounaki, M., de Wit, S., Antoniadis, K., Bonanos, A. Z., et al. (2026). *The Dramatic Transition of the Extreme Red Supergiant WOH G64 to a Yellow Hypergiant*. *Nat Astron*, pp. 1–12.
- Nakanishi, H., and Sofue, Y. (2003). *Three-Dimensional Distribution of the ISM in the Milky Way Galaxy: I. The H I Disk*. *PASJ* 55, pp. 191–202.
- Nedoluha, G. E., and Bowers, P. F. (1992). *VLA Observations of 1612 and 1665 MHz OH Masers Associated with IRC +10420*. *ApJ* 392, p. 249.
- Negueruela, I., Alfaro, E. J., Dorda, R., Marco, A., Maíz Apellániz, J., et al. (2022). *Westerlund 1 under the Light of Gaia EDR3: Distance, Isolation, Extent, and a Hidden Population*. *A&A* 664, A146.
- Neugent, K. F., Levesque, E. M., Massey, P., Morrell, N. I., and Drout, M. R. (2020). *The Red Supergiant Binary Fraction of the Large Magellanic Cloud*. *ApJ* 900, p. 118.
- Neugent, K. F., Massey, P., Skiff, B., and Meynet, G. (2012). *Yellow and Red Supergiants in the Large Magellanic Cloud*. *ApJ* 749, p. 177.
- Nieuwenhuijzen, H., and de Jager, C. (1995). *Atmospheric Accelerations and the Stability of Dynamic Supergiant Atmospheres*. *A&A* 302, p. 811.
- Nieuwenhuijzen, H., and de Jager, C. (2000). *Checking the Yellow Evolutionary Void. Three Evolutionary Critical Hypergiants: HD 33579, HR 8752 & IRC +10420*. *A&A* 353, pp. 163–176.
- Nieuwenhuijzen, H., De Jager, C., Kolka, I., Israelian, G., Lobel, A., et al. (2012). *The Hypergiant HR 8752 Evolving through the Yellow Evolutionary Void*. *A&A* 546, A105.
- Niu, Z., Sun, N.-C., and Liu, J. (2024). *Discovery of a Dusty Yellow Supergiant Progenitor for the Type IIb SN 2017gkk*. *ApJ* 970, p. L9.
- Norris, R. P., Baron, F. R., Monnier, J. D., Paladini, C., Anderson, M. D., et al. (2021). *Long Term Evolution of Surface Features on the Red Supergiant AZ Cyg*. *ApJ* 919.2, p. 124.
- O’Connor, E., and Ott, C. D. (2011). *Black Hole Formation in Failing Core-Collapse Supernovae*. *ApJ* 730, p. 70.
- O’Grady, A. J. G., Drout, M. R., Neugent, K. F., Ludwig, B., Götberg, Y., et al. (2024). *Binary Yellow Supergiants in the Magellanic Clouds. I. Photometric Candidate Identification*. *ApJ* 975, p. 29.

- O'Grady, A. J. G., O'Connor, B., Goldberg, J. A., Joyce, M., Molnár, L., et al. (2025). *Betelgeuse's Buddy: X-Ray Constraints on the Nature of α Ori B*. *ApJ* 992, p. 107.
- Oksala, M. E., Kraus, M., Arias, M. L., Borges Fernandes, M., Cidale, L., et al. (2012). *The Sudden Appearance of CO Emission in LHA 115-S 65*. *MNRAS* 426.1, pp. L56–L60.
- Oksala, M. E., Kraus, M., Cidale, L. S., Muratore, M. F., and Borges Fernandes, M. (2013). *Probing the Ejecta of Evolved Massive Stars in Transition. A VLT/SINFONI K-band Survey*. *A&A* 558, A17.
- Oudmaijer, R. D. (1998). *High Resolution Spectroscopy of the Post-Red Supergiant IRC+10420 - I. The Data*. *A&ASS* 129.3, pp. 541–552.
- Oudmaijer, R. D., Davies, B., de Wit, W.-J., and Patel, M. (2009). *Post-Red Supergiants*. In: *The Biggest, Baddest, Coolest Stars*. Ed. by D. G. Luttermoser, B. J. Smith, and R. E. Stencel. ASP Conference Series, Vol. 412. Astronomical Society of the Pacific, p. 17.
- Oudmaijer, R. D., and Wit, W. J. de (2013). *Neutral and Ionised Gas around the Post-Red Supergiant IRC +10 420 at AU Size Scales*. *A&A* 551, A69.
- Oudmaijer, R. D., Groenewegen, M. A. T., Matthews, H. E., Blommaert, J. A. D. L., and Sahu, K. C. (1996). *The Spectral Energy Distribution and Mass-Loss History of IRC+10420*. *MNRAS* 280, pp. 1062–1070.
- Pasquato, E., Pourbaix, D., and Jorissen, A. (2011). *Limits in Astrometric Accuracy Induced by Surface Brightness Asymmetries in Red Supergiant Stars*. *A&A* 532, A13.
- Patrick, L. R., Lennon, D. J., Britavskiy, N., Evans, C. J., Sana, H., et al. (2019). *The VLT-FLAMES Tarantula Survey. XXXI. Radial Velocities and Multiplicity Constraints of Red Supergiant Stars in 30 Doradus*. *A&A* 624, A129.
- Patrick, L. R., Lennon, D. J., Evans, C. J., Sana, H., Bodensteiner, J., et al. (2020). *Multiplicity of the Red Supergiant Population in the Young Massive Cluster NGC 330*. *A&A* 635, A29.
- Patrick, L. R., Lennon, D. J., Najarro, F., Shenar, T., Bodensteiner, J., et al. (2025). *Binarity at LOW Metallicity (BLOeM): The Multiplicity Properties and Evolution of BAF-type Supergiants*. *A&A* 698, A39.
- Pauli, D., Langer, N., Schootemeijer, A., Marchant, P., Jin, H., et al. (2026). *The Drastic Impact of Eddington-limit Induced Mass Ejections on Massive Star Populations*. *A&A* 707, A11.
- Percy, J. R., and Zsoldos, E. (1992). *Photometry of Yellow Semiregular Variables: HR 8752 (= V 509 Cassiopeiae)*. *A&A* 263, pp. 123–128.
- Percy, J. R., and Kolin, D. L. (2000). *Studies of Yellow Semiregular(SRd) Variables*. *Journal of the American Association of Variable Star Observers* 28, pp. 1–9.
- Petit, P., Louge, T., Théado, S., Paletou, F., Manset, N., et al. (2014). *PolarBase: A Database of High-Resolution Spectropolarimetric Stellar Observations*. *PASP* 126, p. 469.
- Petrov, B., Vink, J. S., and Gräfener, G. (2016). *Two Bi-Stability Jumps in Theoretical Wind Models for Massive Stars and the Implications for Luminous Blue Variable Supernovae*. *MNRAS* 458, pp. 1999–2011.
- Piters, A., de Jager, C., and Nieuwenhuijzen, H. (1988). *The Atmospheric Structure, Stellar Wind and Binary Characteristics Of the Hypergiant HR 8752 (G0-5Ia+)*. *A&A* 196, pp. 115–127.
- Podsiadlowski, P., Joss, P. C., and Hsu, J. J. L. (1992). *Presupernova Evolution in Massive Interacting Binaries*. *ApJ* 391, p. 246.
- Rajchl, R. (1933). *Observations d'étoiles Variables*. *Publications of the Astronomical Institute of the Charles University* 18, pp. 1–20.

- Rate, G., Crowther, P. A., and Parker, R. J. (2020). *Unlocking Galactic Wolf-Rayet Stars with Gaia DR2 - II. Cluster and Association Membership*. MNRAS 495, pp. 1209–1226.
- Reguitti, A., Pastorello, A., Smartt, S. J., Valerin, G., Pignata, G., et al. (2025). *SN 2024abfo: A Partially Stripped Type II Supernova from a Yellow Supergiant*. A&A 698, A129.
- Reimers, D. (1975). *Circumstellar Absorption Lines and Mass Loss from Red Giants*. Memoires of the Societe Royale des Sciences de Liege 8, pp. 369–382.
- Renzo, M., Zapartas, E., Mink, S. E. de, Götberg, Y., Justham, S., et al. (2019). *Massive Runaway and Walkaway Stars - A Study of the Kinematical Imprints of the Physical Processes Governing the Evolution and Explosion of Their Binary Progenitors*. A&A 624, A66.
- Reynolds, T. M., Fraser, M., and Gilmore, G. (2015). *Gone without a Bang: An Archival HST Survey for Disappearing Massive Stars*. MNRAS 453, pp. 2885–2900.
- Rodríguez, Ó. (2022). *Luminosity Distribution of Type II Supernova Progenitors*. MNRAS 515, pp. 897–913.
- Rózański, T., Niemczura, E., Lemiesz, J., Posiłek, N., and Rózański, P. (2022). *SUPNet: Neural Network for Stellar Spectrum Normalisation*. A&A 659, A199.
- Sana, H., de Mink, S. E., de Koter, A., Langer, N., Evans, C. J., et al. (2012). *Binary Interaction Dominates the Evolution of Massive Stars*. Science 337, p. 444.
- Sana, H., Le Bouquin, J.-B., Lacour, S., Berger, J.-P., Duvert, G., et al. (2014). *Southern Massive Stars at High Angular Resolution: Observational Campaign and Companion Detection*. ApJS 215, p. 15.
- Sargent, W. L. W. (1961). *The Circumstellar Envelope of Rho Cassiopeiae*. ApJ 134, p. 142.
- Sblewski, M. (2023). *Observations from the AAVSO International Database*.
- Schuster, M. T., Humphreys, R. M., and Marengo, M. (2006). *The Circumstellar Environments of NML Cygni and the Cool Hypergiants*. AJ 131, pp. 603–611.
- Schuster, M. T., Humphreys, R. M., Smith, N., Davidson, K., and Gehrz, R. D. (2003). *A Gallery of Cool Hypergiants — Imaging Their Circumstellar Environments*. In: *A Massive Star Odyssey: From Main Sequence to Supernova*. Vol. 212, p. 228.
- Schwarzschild, M. (1975). *On the Scale of Photospheric Convection in Red Giants and Supergiants*. The Astrophysical Journal 195, pp. 137–144.
- Sheffer, Y., and Lambert, D. L. (1987). *Spectroscopic Observations of Yellow Supergiants: II. Multiperiodic Variability of HR 8752*. PASP 99, pp. 1277–1287.
- Sheffer, Y., and Lambert, D. L. (1992). *Behavioral Study of Yellow Supergiants: III. [N II] Emission of HR 8752 from 1961-1991*. PASP 104, p. 1054.
- Shenoy, D., Humphreys, R. M., Jones, T. J., Marengo, M., Gehrz, R. D., et al. (2016). *Searching for Cool Dust in the Mid-to-far Infrared: The Mass-loss Histories of the Hypergiants μ Cep, VY CMa, IRC+10420, and ρ Cas*. AJ 151, p. 51.
- Smartt, S. J. (2015). *Observational Constraints on the Progenitors of Core-Collapse Supernovae: The Case for Missing High-Mass Stars*. Publications of the Astronomical Society of Australia 32, e016.
- Smartt, S. J., Eldridge, J. J., Crockett, R. M., and Maund, J. R. (2009). *The Death of Massive Stars - I. Observational Constraints on the Progenitors of Type II-P Supernovae*. MNRAS 395, pp. 1409–1437.
- Smith, N. (2019). *The Isolation of Luminous Blue Variables Resembles Aging B-type Supergiants, Not the Most Massive Unevolved Stars*. MNRAS 489.3, pp. 4378–4388.

- Smith, N., Aghakhanloo, M., Murphy, J. W., Drout, M. R., Stassun, K. G., et al. (2019). *On the Gaia DR2 Distances for Galactic Luminous Blue Variables*. MNRAS 488, pp. 1760–1778.
- Smith, N., Humphreys, R. M., Davidson, K., Gehrz, R. D., Schuster, M. T., et al. (2001). *The Asymmetric Nebula Surrounding the Extreme Red Supergiant Vy Canis Majoris*. AJ 121.2, p. 1111.
- Smith, N., and Tombleson, R. (2015). *Luminous Blue Variables Are Antisocial: Their Isolation Implies That They Are Kicked Mass Gainers in Binary Evolution*. MNRAS 447.1, pp. 598–617.
- Smith, N., Vink, J. S., and Koter, A. de (2004). *The Missing Luminous Blue Variables and the Bistability Jump*. ApJ 615.1, p. 475.
- Smolinski, J., Climenhaga, J. L., and Fletcher, J. M. (1989). *Mass Ejections from the G-Type Hypergiant HR 8752*. In: *IAU Colloquium 113: Physics of Luminous Blue Variables*. Vol. 157, p. 131.
- Söding, L., Edenhofer, G., Enßlin, T., Frank, P., Kissmann, R., et al. (2024). *Spatially Coherent 3D Distributions of HI and CO in the Milky Way - Data Products*. Zenodo: 12578443.
- Söding, L., Edenhofer, G., Enßlin, T. A., Frank, P., Kissmann, R., et al. (2025). *Spatially Coherent 3D Distributions of HI and CO in the Milky Way*. A&A 693, A139.
- Stefanik, R. P., Torres, G., Lovegrove, J., Pera, V. E., Latham, D. W., et al. (2010). *Epsilon Aurigae: An Improved Spectroscopic Orbital Solution*. AJ 139, pp. 1254–1260.
- Stempels, E., and Telting, J. H. (2017). *FIESTool: Automated Data Reduction for Fiber-fed Echelle Spectrograph (FIES)*. Astrophysics Source Code Library: asc1:1708.009.
- Stickland, D. J. (1985). *IRAS Observations of the Cool Galactic Hypergiants*. The Observatory 105, pp. 229–232.
- Stothers, R. B., and Chin, C.-W. (2001). *Yellow Hypergiants as Dynamically Unstable Post-Red Supergiant Stars*. ApJ 560, pp. 934–936.
- Stothers, R. B., and Chin, C.-W. (1996). *Evolution of Massive Stars into Luminous Blue Variables and Wolf-Rayet Stars for a Range of Metallicities: Theory versus Observation*. ApJ 468, p. 842.
- Straizys, V., Kazlauskas, A., Boyle, R. P., Janusz, R., Zdanavičius, J., et al. (2021). *Interstellar Extinction in the Direction of the Open Cluster King 7 and New Parameters of the Cluster*. AJ 162.6, p. 224.
- Takeda, Y., and Takada-Hidai, M. (1994). *On the Abundance of Sodium in A-F Supergiants*. PASJ 46, pp. 395–413.
- Tartaglia, L., Fraser, M., Sand, D. J., Valenti, S., Smartt, S. J., et al. (2017). *The Progenitor and Early Evolution of the Type IIb SN 2016gkg*. ApJ 836, p. L12.
- Telting, J. H., Avila, G., Buchhave, L., Frandsen, S., Gandolfi, D., et al. (2014). *FIES: The High-Resolution Fiber-fed Echelle Spectrograph at the Nordic Optical Telescope*. Astron. Nachr. 335, p. 41.
- Tody, D. (1986). *The IRAF Data Reduction and Analysis System*. In: *Instrumentation in Astronomy VI*. Vol. 627, p. 733.
- van Ballegoij, E. J. (2023). *Observations from the AAVSO International Database*.
- van Belle, G. T., Creech-Eakman, M. J., and Hart, A. (2009). *Supergiant Temperatures and Linear Radii from Near-Infrared Interferometry*. MNRAS 394, pp. 1925–1935.
- van Genderen, A. M., Lobel, A., Nieuwenhuijzen, H., Henry, G. W., de Jager, C., et al. (2019). *Pulsations, Eruptions, and Evolution of Four Yellow Hypergiants*. A&A 631, A48.

- van Genderen, A. M., Lobel, A., Timmerman, R., Deul, E. R., Vos, A., et al. (2025). *Investigation of the Pulsations, Outbursts, and Evolution of the Yellow Hypergiants: Rho Cas, HR 8752, and HR 5171A, with Notes on HD 179821*. A&A 694, A136.
- van Loon, J. T. (2025). *Red Supergiant Mass Loss and Mass-Loss Rates*. Galaxies 13.4.
- Vink, J. S., de Koter, A., and Lamers, H. J. G. L. M. (1999). *On the Nature of the Bi-Stability Jump in the Winds of Early-Type Supergiants*. Astronomy and Astrophysics 350, pp. 181–196.
- Vollmann, W. (2023). *Observations from the AAVSO International Database*.
- Vollmann, W. (2024). *Observations from the AAVSO International Database*.
- Vollmann, W., and Sigismondi, C. (2022). *ATel #15800: RW Cephei Great Dimming*.
- Wallström, S. H. J., Lagadec, E., Müller, S., Black, J. H., Cox, N. L. J., et al. (2017). *ALMA Compact Array Observations of the Fried Egg Nebula - Evidence for Large-Scale Asymmetric Mass-Loss from the Yellow Hypergiant IRAS 17163-3907*. A&A 597, A99.
- Walmswell, J. J., and Eldridge, J. J. (2012). *Circumstellar Dust as a Solution to the Red Supergiant Supernova Progenitor Problem: Circumstellar Dust and the Red Supergiant Problem*. MNRAS 419.3, pp. 2054–2062.
- Wang, S., Jiang, B. W., Zhao, H., Chen, X., and de Grijs, R. (2017). *The Optical–Mid-infrared Extinction Law of the $l = 165^\circ$ Sightline in the Galactic Plane: Diversity of the Extinction Law in the Diffuse Interstellar Medium*. ApJ 848.2, p. 106.
- Warren, P. R. (1973). *A Model Atmosphere Analysis of the Super-Supergiant HR 5171*. MNRAS 161, p. 427.
- Weis, K. (2003). *On the Structure and Kinematics of Nebulae around LBGs and LBV Candidates in the LMC*. A&A 408, pp. 205–229.
- Wittkowski, M., Arroyo-Torres, B., Marcaide, J. M., Abellan, F. J., Chiavassa, A., et al. (2017). *VLT/AMBER Spectro-Interferometry of the Late-Type Supergiants V766 Cen (=HR 5171 A), σ Oph, BM Sco, and HD 206859*. A&A 597, A9.
- Woolley, S. E., Pinto, P. A., Martin, P. G., and Weaver, T. A. (1987). *Supernova 1987A in the Large Magellanic Cloud: The Explosion of a Approximately 20 Msun Star Which Has Experienced Mass Loss?* ApJ 318, p. 664.
- Wright, E. L., Eisenhardt, P. R. M., Mainzer, A. K., Ressler, M. E., Cutri, R. M., et al. (2010). *The Wide-field Infrared Survey Explorer (WISE): Mission Description and Initial On-orbit Performance*. AJ 140, pp. 1868–1881.
- Yamamoto, T., Nishimaki, Y., Motohara, K., Miyata, T., and Tanaka, M. (2007). *Near-Infrared Spectroscopic Monitoring Observations of Three Yellow Hypergiants and Time Variation of 2.3 μ m CO Features of ρ Cassiopeia*. PASJ 59, p. 973.
- Yamanaka, M., Nagayama, T., and Horikiri, T. (2025). *SN 2024iss: Double-peaked Light Curves and Implications for a Yellow Supergiant Progenitor*. PASJ 77, pp. L31–L35.
- Yang, M., Bonanos, A. Z., Jiang, B., Zapartas, E., Gao, J., et al. (2023). *Evolved Massive Stars at Low-Metallicity. V. Mass-loss Rate of Red Supergiant Stars in the Small Magellanic Cloud*. A&A 676, A84.
- Zapartas, E., Wit, S. de, Antoniadis, K., Muñoz-Sánchez, G., Souropanis, D., et al. (2025). *The Effect of Mass Loss in Models of Red Supergiants in the Small Magellanic Cloud*. A&A 697, A167.
- Zsoldos, E. (1986). *Historical Light Curve of HR 8752*. The Observatory 106, pp. 156–160.

SISUKOKKUVÕTE

Kollaste hüperhiidtähtede muutlikkus ja areng

Massiivsete tähtede elu on kosmilises ajaskaalas lühike (kõigest mõned miljonid aastad), kuid sündmusterohke. Nende tähetuul, ioniseeriv kiirgus ja aine väljapursked mõjutavad tugevalt neid ümbritsevat keskkonda.

Massiivsete tähtede elutsükkel jagatakse erinevateks arenguetappideks. Noorte kuumade siniste ülihiidude tuumas põleb kütusena vesinik. Selle ammendumisel tähed paisuvad ja jahtuvad ning muutuvad kõigepealt kollasteks ning seejärel punasteks ülihiidudeks. Enamiku massiivsete tähtede elu lõpeb punase ülihiid arengufaasis – nad plahvatavad supernoovana. Kuid juhul, kui tähe algmass on olnud sobivas vahemikus (20–40 Päikese massi) ja täht on oma elu jooksul läbi tähetuule ja aine väljapursete kaotanud sellest umbes poole, võib täht punasest ülihiidust edasi areneda. Sel juhul tähe temperatuur tõuseb, tema atmosfäär muutub väga ebastabiilseks ja teda nimetatakse kollaseks hüperhiiduks. Käesoleva töö keskmeks on selliste kaugelearenenud tähtede muutlikkuse uurimine. Uurisime kollaste üli- ja hüperhiidude populatsiooni Linnutees ja vaatlesime detailselt kahte hüperhiidtähte: V509 Cas ja RW Cep, mis on väga erinevates arengujärgkudes.

Valisime Linnutees 35 kollast üli- ja hüperhiidu ja uurisime neid ümbritsevat keskkonda – millised tähed kuuluvad hajusparvedesse või OB assotsiatsioonidesse. Tähegruppidesse kuuluvus võimaldab määrata tähtede vanuseid ja annab infot nende dünaamilise mineviku kohta. Tähtede lahkumist parvedest võivad põhjustada kaksiksüsteemi vastastikmõjud, supernoovad ja tähtedevahelised interaktsioonid. Leidsime, et enamik kollaseid ülihiide (20 tähte 25st) kuuluvad hajusparvedesse või OB assotsiatsioonidesse ja seega on nad endiselt seotud oma sünnikohaga. Kümnest hüperhiidust on viis samuti seotud tähegruppidega, üks seotud tähetekke piirkonnaga ja neljal selget grupikuuluvust ei leitud. Need erinevused võivad olla seotud tähe arengu ja mineviku sündmustega. Sellegipoolest ei tuvastanud me ühtegi “ärajoosikut”, ehk tähte, mis oleks minevikus oma grupist välja heidetud.

Linnutees asuvate massiivsete tähtede uurimist muudab keerulisemaks kauguste määramise ebatäpsus. Peaaegu pooleteise miljardi tähe parallaksid on mõõtnud kosmoseteleskoop *Gaia*, kuid muutlike, heledate ja tolmust ümbritsetud tähtede astromeetrilised mõõtmised on ebatäpsed. Tähti ümbritseva keskkonna uurimine võimaldas meil arvutada täpsemad kaugused. Selleks kasutasime nii naabertähtede kauguste kombineerimise meetodit kui ka neutraalse vesinikkaasi 3D jaotust Linnutees. Kahe meetodi põhjal leitud tulemused klapiivad hästi ja nende põhjal täpsustasime ka tähtede koguheledusi.

V509 Cas on olnud ajalooliselt väga muutlik täht, 20. sajandil vaadeldi temas kahte aine väljapurset ja sajandi lõpus tema pinnatemperatuur tõusis 3000 K võrra 20 aasta jooksul. Sellest ajast alates on ta olnud ootamatult stabiilne. Mõõtsime tähe muutlikkust 7 aasta jooksul 2015–2023. a. ja võrdlesime tulemusi 2000. aastate algul tehtud mõõtmistega. V509 Cas pinnatemperatuur on stabiliseerunud

7900 K juures ja temperatuuri muutlikkuse amplituud on võrreldes varasemaga vähenenud, jäädes 200 K juurde. Täht on visuaalselt muutlik umbes 0.05 mag amplituudiga ja pulseerub kvaasiperioodiliselt 100 kuni 200-päevase perioodiga. Tähe pulsatsioonid avalduvad tähe spektraalse muutlikkusena nii spektrijoonte sügavustes kui ka nende radiaalkiirustes. Mõõtes tähe pinna dünaamikat radiaalkiiruste põhjal leidsime, et tähe pinna keskmise paisumise või kokkutõmbumise ja tähe heleduse või temperatuuri muutlikkuse vahel on faasi nihe umbes 1/4 perioodist. Sellist muutlikkust on täheldatud ka teise kollase hüperhiu ρ Cas puhul (Lobel *et al.*, 1998). Emissioonijooned V509 Cas spektris moodustuvad tähte ümbritsevas aines, millel on tõenäoliselt kettalaadne morfoloogia. Sellele viitavad kahetipuline [Ca II] emissioonijooone kuju ja see, et erinevalt neeldumisjoontest, [Ca II] emissioonijooone tugevus ajas ei muutu. Kahekomponendiliste joonte, nt mõlema tiiva emissiooni ja keskse neeldumisega Sc II ja mõned Fe II jooned, muutlikkust põhjustab just tähe pulsatsioonitsükliga varieeruv neeldumiskomponent. Järeldame, et V509 Cas on stabiliseerunud Hertzsprung-Russelli diagrammil vähetäidetud alas, mida nimetatakse “kollaseks evolutsiooniliseks tühimikuks” ja ta võib olla jõudmas kollase hüperhiidtähe arengujärgu lõppfaasi. Tähe edasine evolutsioon on lahtine küsimus, teda ümbritseva aine morfoloogia sarnaneb kuumadele B[e]-tüüpi ülihiidudele ja on võimalik, et pärast mõneajast stabiilsusperioodi (ca tuhandet aastat?) tähe temperatuur jätkab tõusmist ja temast areneb sinine ülihiid.

RW Cep on jahe, umbes 4000 K pinnatemperatuuriga punane hüperhiid. Aastatel 2020–2024 toimus tähes plahvatuslik aine väljapurse, mis sai nimeks “suur tumenemine” tähe heleduse järsu languse tõttu. Vaatlesime tähte tema heledusmiinimumis ja tumenemisest taastumisel. Heledusmiinimumis oli näha $H\alpha$ ja teistes tavapäraselt tugevates neeldumisjoontes sininihkes emissioonikomponenti. See klapib Anugu *et al.* (2023) teooriaga, et heledusmiinimumi põhjustas tähest väljapaisatud kuum gaas, mis kondenseerus tolmuks vaatesihis. Mõõtsime tähe spektris erinevate energianivoodega Fe I neeldumisjoonte radiaalkiirusi, et uurida tähe atmosfääri kihtide kinemaatikat. Kõrgetes atmosfäärikihtides moodustuvad spektrijooned on heledusmiinimumi ajal tugevalt mõjutatud emissioonikomponendist, mis mõjutab radiaalkiiruse mõõtmisi. Kõikide uuritud joonte puhul on radiaalkiiruse maksimum umbes pool aastat pärast heledusmiinimumi, mis viitab aine väljapurske laiaulatuslikule mõjule tähe atmosfääris. Kitsad emissioonikomponendid madala ergastusega joontes ja resonantsjoontes (nt Ba II, Ca I, K I) tugevnesid aine väljapurske ajal. See emissioon moodustub tõenäoliselt jahedamas tähte ümbritsevas aines, mis pärineb varasematest aine väljapursetest. RW Cep spektraalne muutlikkus suure tumenemise ajal sarnaneb kollaste hüperhiidude aine väljapursetele. Spektraalsete omaduste ja ümbritseva keskkonna poolest sarnaneb RW Cep hüperhiiga ρ Cas. RW Cep võib olla varajases kollase hüperhiu arengufaasis.

Massiivsete tähtede evolutsiooniteooria kohaselt võivad RW Cep ja V509 Cas esindada kollaste hüperhiidude alg- ja lõppjärku. Kuid järelduste tegemiseks ei piisa kahest tähest, selleks on vajalikud laiemaulatuslikud kollaste üli- ja hüper-

hiidude populatsioonidele suunatud uuringud. Uurimus Linnutee kollastest üli- ja hüperhiidudest oli esimene osa sellest suuremast projektist. Uued ja peatselt alustavad taeväilevaateprojektid 4MOST, *Nancy Grace Roman Space Telescope* ja *Legacy Survey of Space and Time* võimaldavad teha homogeeniseid statistilisi uuringuid massiivsetest tähtedest, sealhulgas kollastest üli- ja hüperhiidudest, et siduda täheevolutsiooni erinevaid etappe ja luua paremat kooskõla mudelite ja vaatluste vahel.

ACKNOWLEDGEMENTS

During my decade-long journey into astronomy I have had the joy of meeting and getting inspiration from so many wonderful people that I could fill several pages with gratitude. Alas, the thesis is already long, and I cannot mention everyone individually, but I am grateful to all who have encouraged me throughout the years.

A hypergiant-sized thank you to my supervisor Indrek for guiding my path for so many years. Your warmth and enthusiasm always gave me the motivation to keep going. I'm incredibly grateful to Anna for your support and trust in me. An enormous thank you to Andrea for taking me under your wing at ESO.

Thank you to everyone in the stellar physics department! Tõnis, thank you for teaching me all about telescopes and data reduction. Tiina, Laurits, and Heleri, thank you for always being so supportive and kind. Thank you, Sandipan and Veronika, for being great office mates (and for reading my thesis). A huge thank you to all my fellow PhD students with whom I shared my struggles, there's a fun Estonian word for it: *kaaskannatajad*. I am looking forward to seeing your defences soon!

I am deeply grateful to everyone in the Nordic Optical Telescope family! Amanda and John, your mentorship and kindness have meant a lot to me. Thank you to my *Tinabana* flatmates – Emil, Akke, Katja, and Zuri for the good times. And thank you to Nada, Pol, Viki, Jeppe and all the other NOT and ING students for many adventures on *la Isla Verde*.

Thank you to all the wonderful people at ESO Chile! I am immensely grateful to you for making me a part of your warm and friendly community on the faraway continent. Thank you for your encouragement, support, and advice. To Noah, Fred, Sara, Akke, Scarlett, Sara, Jana, Javier, and Ciara – thank you for being there to share ideas, joys, and worries.

And going back to the time when I could not even imagine the adventures I was going to have... Thank you to everyone at Teadusmalev for giving the high-school me a first look into the world of space science. Thank you, Amara and Ilgmārs, for giving me the chance to dip my toes into astronomy at Baldone Observatory – I got my hands on a telescope and never looked back!

Finally, thank you to my family for always being by my side. Thank you to my dear friends Janna, Helen, Eliisa and Ingel for helping me keep my sanity (and a life outside of work), and my fiancé, Stevin, for always taking care of me and reminding me to stay hydrated.

The research included in this thesis has been supported by the Nordic Optical Telescope and the European Southern Observatory.

I would like to thank the observers of Tartu Observatory, Nordic Optical Telescope, AAVSO, Bright Star Monitoring programme, Dominion Astrophysical Observatory, Observatoire de Haute-Provence, and Ondřejov Observatory for the data used in this thesis.

Based on observations made with the Nordic Optical Telescope, owned in collaboration by the University of Turku and Aarhus University, and operated jointly by Aarhus University, the University of Turku and the University of Oslo, representing Denmark, Finland and Norway, the University of Iceland and Stockholm University at the Observatorio del Roque de los Muchachos, La Palma, Spain, of the Instituto de Astrofísica de Canarias. Based on spectral data retrieved from the ELODIE archive at Observatoire de Haute-Provence (OHP). Based on observations obtained at the Dominion Astrophysical Observatory, Herzberg Astronomy and Astrophysics Research Centre, National Research Council of Canada. Based on observations made with the Perek 2 m telescope at Ondřejov Observatory, operated by the Astronomical Institute of the Czech Academy of Sciences. This work includes data collected with the TESS mission, obtained from the MAST data archive at the Space Telescope Science Institute (STScI). Funding for the TESS mission is provided by the NASA Explorer Program. STScI is operated by the Association of Universities for Research in Astronomy, Inc., under NASA contract NAS 5-26555. This work has made use of data from the European Space Agency (ESA) mission *Gaia* (<https://www.cosmos.esa.int/gaia>), processed by the *Gaia* Data Processing and Analysis Consortium (DPAC, <https://www.cosmos.esa.int/web/gaia/dpac/consortium>). Funding for the DPAC has been provided by national institutions, in particular the institutions participating in the *Gaia* Multilateral Agreement. This research has made use of the Jean-Marie Mariotti Center JSDC catalogue, which involves the JMDC catalogue. JSDC available at <http://www.jmmc.fr/jscd>. This work has made use of the ground-based research infrastructure of Tartu Observatory, funded through the projects TT8 (Estonian Research Council), KosEST (EU Regional Development Fund), and TARISTU24-TK3 (Estonian Research Council). This research has received funding from the European Union's Horizon Europe research and innovation programme under grant agreement No. 101079231 (EXOHOST), and from the United Kingdom Research and Innovation (UKRI) Horizon Europe Guarantee Scheme (grant number 10051045). This project has received funding from the European Union's Framework Programme for Research and Innovation Horizon 2020 under the Marie Skłodowska-Curie Grant Agreement No. 823734. This work was supported by the Estonian Research Council grant PRG 2159. Some professional training has been possible thanks to the funding from Republic of Estonia Education and Youth board.

PUBLICATIONS

CURRICULUM VITAE

Personal data

Name: Anni Kasikov
Citizenship: Estonian
Current employment: Tartu Observatory, Junior research fellow
Address: University of Tartu, Tartu Observatory
Observatooriumi 1, Tõravere
61602, Tartu county, Estonia
E-mail: anni.kasikov@ut.ee
Website: annikasikov.github.io/

Research interests

Evolution of massive stars, eruptive mass loss, yellow supergiants and hypergiants, stellar spectroscopy, time series analysis

Employment

2021–2026 Junior Research Fellow, Tartu Observatory, University of Tartu, Estonia
2025 (1 year) Student, European Southern Observatory, Chile
2021–2023 Student Support Astronomer, Nordic Optical Telescope, Spain
2017 (3 months) SpaceTEM Intern, Baldone Observatory, Latvia

Education

2021–2026 PhD studies (physics), University of Tartu
2019–2021 Master’s studies (physics), University of Tartu, *cum laude*
2016–2019 Bachelor’s studies (physics, chemistry, and materials science), University of Tartu
2004-2016 Rakvere Realgymnasium, graduated with honours

Teaching and mentoring

2025 Supervisor for a high-school research project
2023–2024 Supervisor at the Tartu Observatory summer program for high school students
2023 Instructor in summer school “Asteroid Research Training Workshop” in Tõravere, Estonia
2023 Assistant lecturer in General Astronomy: Observations

Language skills

Estonian – Native proficiency
English – Full professional proficiency
German – Limited working proficiency
Spanish – Limited working proficiency

Honours and grants

2025 IAU travel grant to support participation in IAU Symposium 402
2024 Ernst Julius Öpik scholarship, Tartu Observatory, Estonia
2024 Kristjan Jaak Scholarship to participate in the ESO La Silla School, Republic of Estonia Education and Youth board
2023 Kristjan Jaak Scholarship to conduct research at the Nordic Optical Telescope, Republic of Estonia Education and Youth board
2022 Dora+ stipend to attend the Summer School for Astrostatistics in Crete, Republic of Estonia Education and Youth board
2020 Rotalia Foundation (USA) stipend, Estonia
2017 “Outstanding Student Poster Award” at the European Planetary Science Congress, Latvia

Professional training

2024 Machine Learning and Astrostatistics School: Applications to Massive Stars, Valparaíso, Chile.
2024 1-month science visit to National Observatory of Brazil.
2024 Instrumentation and spectral surveys workshop, Uppsala University, Sweden.
2024 La Silla observing school, European Southern Observatory, Chile.
2023 2.5-month science visit to University of La Plata, Argentina.
2023 Stellar spectroscopy workshop, Tartu Observatory, Estonia.
2023 Stellar Winds and Outflows summer school, Czech Academy of Sciences, Czech Republic.
2022 Erasmus+ School on Eclipsing Binaries and Asteroseismology, Canarian Astrophysical Institute, La Palma, Spain.
2022 Summer school for Astrostatistics in Crete, University of Crete, Greece.
2017 3-month SpaceTEM summer internship in Baldone Observatory as part of the European Union Interreg Estonia-Latvia project, Latvia.

Scientific community work

- 2025 Scientific assistant in the Observing Programmes Committee, European Southern Observatory
- 2025 Organiser of Python Coffee and Wine and Cheese, European Southern Observatory, Chile
- 2024 Member of the local organising committee at Ariel consortium meeting in Tartu, Estonia
- 2024 Scientific referee, Serbian Astronomical Journal
- 2022 Member of the local organising committee in conference: “NOT – a telescope for the future” on La Palma, Spain
- 2016 Member of the Physics Students’ Society, University of Tartu

Outreach

- 2025 “An Estonian PhD Student’s Unique Experience at a World-Class Observatory” Tartu Observatory news release about my ESO studentship
- 2025 Guide at ESO/ALMA open doors’ day
- 2024 Public lecture 3-minute science presentation and popular science article on Yellow Hypergiants in the Estonian National Broadcasting Service science portal
- 2024 Presentation at Estonian amateur astronomers’ meeting “Massive Stars in Our Galaxy and Beyond”
- 2024 Public lecture at Tartu Observatory 1.5 m telescope 50-year anniversary event “Current and future science with the 1.5 m telescope”
- 2024 Interviews in the regional newspaper “Tartu Postimees” on: Perseid meteor shower; High school student programme at Tartu Observatory; 50-year anniversary of the Tartu Observatory 1.5 m telescope
- 2023–2024 Presenter and guide at the Tartu Observatory open doors “Starry night” program
- 2021 Presentation at the inspiration day “Women in space” in Tartu Observatory
- 2021 Interview “When stargazing is more than just entertainment” in Estonia-Latvia stories brochure about my internship in Baldone Observatory in Latvia
- 2020 Public lecture “About Betelgeuse” in Tartu Old Observatory
- 2018–2021 Tartu Observatory tour guide for student visits and instructor for active learning programs

Conference and seminar talks

- 2025 Seminar talk, European Southern Observatory, Chile. Title: “Painting a Family Portrait of Yellow Super- and Hypergiants in the Milky Way”
- 2025 Seminar talk, European Southern Observatory, Chile. Title: “Python coffee. Looking for needles in a haystack: querying large astronomical databases with ADQL”
- 2025 Poster contribution, IAU Symposium 402 “Massive Stars Across Redshifts in the Era of JWST and Large-Scale Surveys” in Enseñada, Mexico. Title: “Yellow Hypergiants and Where to Find Them”
- 2024 Seminar talk, Massive Stars Online Lecture series organised by IAU G2 commission. Title: “Hydrodynamics and related problems (I): Convection”
- 2024 Contributed talk, conference “Physics of Extreme Massive Stars” in Rio de Janeiro, Brazil. Title: “The post-outburst evolution of RW Cep”
- 2024 Seminar talk, National Observatory of Brazil. Title: “A tale of two hypergiants”
- 2023 Seminar talk, University of La Plata, Argentina. Title: “Yellow hypergiant V509 Cas – stable in the ‘Yellow Void’”
- 2023 Seminar talk, Tartu Observatory astrophysics seminar. Title: “Journey into the ‘Yellow Void’”
- 2022 Contributed talk, conference “NOT – a telescope for the future” on La Palma, Spain. Title: “Following V509 Cas into the void with FIES”
- 2017 Poster contribution, conference “The European Planetary Science Congress” in Riga, Latvia. Title: “Methods for Finding New Carbon Stars in the Cassiopeia Constellation”

Publications

- Kasikov, A.**, Mehner, A., Kolka, I., and Aret, A. *Painting a family portrait of the yellow super- and hypergiants in the Milky Way I. Constraining the distances and luminosities.* A&A, 708, A78
- Dennefeld, M., Pursimo, T., Carvalho, C., et al. [incl. **Kasikov, A.**] (2026). *AGN in Gaia alerts: from flares to changing look quasars.* Ap&SS, 371(1), 12
- Kasikov, A.**, Mehner, A., Kolka, I., and Aret, A. (2025). *Yellow hypergiants and where to find them.* In proceedings of IAU Symposium 402. *Massive stars across redshifts in the era of JWST and large-scale surveys*, held in 15-19 September in Ensenada, Mexico
- Kasikov, A.**, Kolka, I., Aret, A., et al. (2025). *Atmospheric dynamics of the hypergiant RW Cep during the Great Dimming.* A&A, 694, A153. DOI: 10.1051/0004-6361/202453546
- Kasikov, A.**, Kolka, I., Aret, A., et al. (2024). *Yellow hypergiant V509 Cas: Stable in the ‘yellow void’.* A&A, 686, A270

- Farnocchia, D., Reddy, V., Bauer, J. M., et al. [incl. **Kasikov, A.**] (2023). *The Second International Asteroid Warning Network Timing Campaign: 2005 LW3*. PSJ, 4(11), 203
- Negro, M., Di Lalla, N., Omodei, N., et al. [incl. **Kasikov, A.**] (2023). *The IXPE View of GRB 221009A*. ApJL, 946, L21
- Kasikov, A.**, Kolka, I., and Aret, A. (2022). *Following V509 Cas into the void with FIES*. In proceedings of *NOT - A Telescope For the Future*, held in 7-10 June, 2022 on La Palma, Canary Islands, Spain
- Geem, J., Ishiguro, M., Takahashi, J., et al. [incl. **Kasikov, A.**] (2022). *(3200) Phaethon polarimetry in the negative branch: new evidence for the anhydrous nature of the DESTINY+ target asteroid*. MNRAS, 516, L53
- Farnocchia, D., Reddy, V., Bauer, J. M., et al. [incl. **Kasikov, A.**] (2022). *International Asteroid Warning Network Timing Campaign: 2019 XS*. PSJ, 3(7), 156
- Folsom, C. P., Kama, M., Eenmäe, T., et al. [incl. **Kasikov, A.**] (2022). *A rare phosphorus-rich star in an eclipsing binary from TESS*. A&A, 658, A105

ELULOOKIRJELDUS

Isikuandmed

Nimi: Anni Kasikov
Kodakondsus: Eesti
Praegune töökoht: Tartu observatoorium, nooremteadur
Aadress: Tartu Ülikool, Tartu observatoorium
Observatooriumi 1, Tõravere
61602, Tartumaa, Eesti
E-mail: anni.kasikov@ut.ee
Kodulehekülj: annikasikov.github.io/

Peamised uurimisvaldkonnad

Massiivsete tähtede evolutsioon, massikaotuse väljapursked, kollased ülihiidtähed ja hüperhiidtähed, tähespektroskoopia, aegridade analüüs

Teenistuskäik

2021–2026 nooremteadur, Tartu observatoorium, Tartu Ülikool, Eesti
2025 (1 aasta) doktorant, Euroopa Lõunaobservatoorium, Tšiili
2021–2023 tugiastronoom, Põhjamaade optiline teleskoop, Hispaania
2017 (3 kuud) SpaceTEM praktikant, Baldone observatoorium, Läti

Haridus

2021–2026 doktorantuur (füüsika), Tartu Ülikool
2019–2021 magistriõpingud (füüsika), Tartu Ülikool, *cum laude*
2016–2019 bakalaureuseõpingud (füüsika, keemia ja materjaliteadus), Tartu Ülikool
2004-2016 Rakvere Reaalgümnaasium, kuldmedal

Õpetamiskogemus

2025 gümnaasiumi uurimistöö juhendaja
2023–2024 teadusmalevlaste juhendaja Tartu observatooriumis
2023 juhendaja suvekoolis “Asteroid Research Training Workshop”
Tõraveres
2023 õppejõud aines praktiline astronoomia

Keelteoskus

eesti – emakeel

inglise – väga hea

saksa – madal kesktase

hispaania – madal kesktase

Autasud ja stipendiumid

- 2025 IAU reisigrant sümposiumil nr 402 osalemiseks
- 2024 Ernst Julius Öpiku stipendium, Tartu observatoorium
- 2024 Kristjan Jaagu välislähetuse stipendium ESO La Silla vaatluskoolis osalemiseks, Haridus- ja noorteamet
- 2023 Kristjan Jaagu välislähetuse stipendium teadustöö tegemiseks Põhja-maade optilise teleskoobiga, Haridus- ja noorteamet
- 2022 Dora+ stipendium Kreeta astrostatistika suvekoolis osalemiseks, Haridus- ja noorteamet
- 2020 Rotalia Fondi stipendium
- 2017 “Outstanding Student Poster Award” konverentsil “European Planetary Science Congress”, Läti

Enesetäiendus

- 2024 masinõppe ja astrostatistika kool: rakendused massiivsete tähtede analüüsiks, Valparaíso, Tšiili
- 2024 1 kuu pikkune teaduskülastus Brasiilia riiklikku observatooriumisse
- 2024 astronoomiliste instrumentide ja spektraalsete taevaülevaadete töötuba, Uppsala Ülikool, Rootsi
- 2024 La Silla vaatluskool, Euroopa Lõunaobservatoorium, Tšiili
- 2023 2.5 kuu pikkune teaduskülastus La Plata Ülikooli, Argentiina
- 2023 tähespektroskoopia koolitus, Tartu observatoorium
- 2023 suvekool tähetuulte ja aine väljavoolu kohta, Tšehhi
- 2022 Erasmus+ suvekool varjutusmuutlike kaksiktähtede ja astero-seismoloogia kohta, Kanaari astrofüüsika instituut, La Palma, Hispaania
- 2022 Kreeta astrostatistika suvekool, Kreeta Ülikool, Kreeka
- 2017 3 kuu pikkune SpaceTEM suvepraktika Baldone observatooriumis Euroopa Liidu Interreg projekti raames, Läti

Teadusorganisatoorne tegevus

- 2025 teadusassistent vaatlusprogrammide komitees, Euroopa Lõunaobservatoorium
- 2025 seminariseeria “Python Coffee” ja iganädalase “vein ja juust” organiseerija, Euroopa Lõunaobservatoorium, Tšiili
- 2024 kohaliku organiseerimiskomitee liige Arieli konsortsiumi kohtumisel Tartus
- 2024 retsensent, Serbian Astronomical Journal
- 2022 kohaliku organiseerimiskomitee liige konverentsil “NOT – a telescope for the future” La Palmal, Hispaanias
- 2016 Füüsika üliõpilaste seltsi liige, Tartu Ülikool

Teaduse populariseerimine

- 2025 “Eesti doktorandi ainulaadne kogemus maailma tipp-observatooriumis” Tartu observatooriumi uudislugu
- 2025 giid ESO/ALMA avatus uste päeval
- 2024 teadus kolme minutiga esitlus ja populaarteaduslik artikkel Novatoris
- 2024 esitlus astronoomiafestivalil “Massiivsed tähed meie galaktikas ja kaugemal”
- 2024 esitlus Tartu observatooriumi 1.5-m teleskoobi 50. juubeli üritusel “Teadus suure teleskoobiga nüüd ja tulevikus”
- 2024 intervjuud ajalehes Tartu Postimees: Perseiidide meteorivool; teadusmalev Tartu observatooriumis; 1.5-meetrise teleskoobi 50. juubel
- 2023–2024 esitleja ja giid “Tähtede õhtu” programmis Tartu observatooriumis
- 2021 esitlus inspiratsioonipäeval “Naised teaduses” Tartu observatooriumis
- 2021 intervjuu “When stargazing is more than just entertainment” Eesti-Läti lugude brošüüris
- 2020 esitlus “Betelgeuse elust ja olust” Tartu tähetornis
- 2018–2021 giid Tartu observatooriumi külastuskeskuses

Ettekanded konverentsidel ja seminarides

- 2025 seminar Euroopa Lõunaobservatooriumis Tšiilis. Pealkiri: “Painting a Family Portrait of Yellow Super- and Hypergiants in the Milky Way”
- 2025 seminar Euroopa Lõunaobservatooriumis Tšiilis. Pealkiri: “Python coffee. Looking for needles in a haystack: querying large astronomical databases with ADQL”
- 2025 poster IAU sümpoosionil nr 402 “Massive Stars Across Redshifts in the Era of JWST and Large-Scale Surveys” Enseñadas Mehhikos. Pealkiri: “Yellow Hypergiants and Where to Find Them”
- 2024 seminar, IAU G2 komitee massiivsete tähtede loengukursus veebis. Pealkiri: “Hydrodynamics and related problems (I): Convection”
- 2024 esitlus konverentsil “Physics of Extreme Massive Stars” Rio de Janeiros Brasiilias. Pealkiri: “The post-outburst evolution of RW Cep”
- 2024 seminar Brasiilia riiklikus observatooriumis. Pealkiri: “A tale of two hypergiants”
- 2023 seminar La Plata Ülikoolis Argentiinas. Pealkiri: “Yellow hypergiant V509 Cas – stable in the ‘Yellow Void’”
- 2023 seminar Tartu observatooriumis. Pealkiri: “Journey into the ‘Yellow Void’”
- 2022 esitlus konverentsil “NOT – a telescope for the future” La Palmal Hispaanias. Pealkiri: “Following V509 Cas into the void with FIES”
- 2017 poster konverentsil “The European Planetary Science Congress” Riias Lätis. Pealkiri: “Methods for Finding New Carbon Stars in the Cassiopeia Constellation”

DISSERTATIONES ASTRONOMIAE UNIVERSITATIS TARTUENSIS

1. **Tõnu Viik.** Numerical realizations of analytical methods in theory of radiative transfer. Tartu, 1991.
2. **Enn Saar.** Geometry of the large scale structure of the Universe. Tartu, 1991.
3. **Maret Einasto.** Morphological and luminosity segregation of galaxies. Tartu, 1991.
4. **Urmas Haud.** Dark Matter in galaxies. Tartu, 1991.
5. **Eugene A. Ustinov.** Inverse problems of radiative transfer in sounding of planetary atmospheres. Tartu, 1992.
6. **Peeter Tenjes.** Models of regular galaxies. Tartu, 1993.
7. **Ivar Suisalu.** Simulation of the evolution of large scale structure elements with adaptive multigrid method. Tartu, 1995.
8. **Teimuraz Shvelidze.** Automated quantitative spectral classification of stars by means of objective prism spectra: the method and applications. Tartu, 1999.
9. **Jelena Gerškevič.** Formation and evolution of binary systems with compact objects. Tartu, 2002.
10. **Ivan Suhhonenko.** Large-scale motions in the universe. Tartu, 2003.
11. **Antti Tamm.** Structure of distant disk galaxies. Tartu, 2006.
12. **Vladislav-Veniamin Pustynski.** Modeling the reflection effect in pre-cataclysmic binary systems. Tartu, 2007.
13. **Anna Aret.** Evolutionary separation of mercury isotopes in atmospheres of chemically peculiar stars. Tartu, 2009.
14. **Mari Burmeister.** Characteristics of the hot components of symbiotic stars. Tartu, 2010.
15. **Elmo Tempel.** Tracing galaxy evolution by their present-day luminosity function. Tartu, 2011.
16. **Anti Hirv.** Estimation of time delays from light curves of gravitationally lensed quasars. Tartu, 2011.
17. **Rain Kipper.** Galaxy modelling: dynamical methods and applications. Tartu, 2016, 134 p.
18. **Lauri Juhan Liivamägi.** Properties and spatial distribution of galaxy superclusters. Tartu, 2017, 185 p.
19. **Jaan Laur.** Variability survey of massive stars in Milky Way star clusters. Tartu, 2017, 183 p.
20. **Boris Zhivkov Deshev.** On the coevolution of galaxies and their host clusters. Tartu, 2019, 199 p.
21. **Tiina Liimets.** Nebulosities and jets from outbursting evolved stars. Tartu, 2019, 207 p.
22. **Maarja Bussov.** Clustering Analysis for Astrophysical Structures. Tartu, 2020, 113 p.

23. **Teet Kuutma.** Galaxies and non-galactic baryons in cosmic filaments. Tartu, 2021, 123 p.
24. **Toni Tuominen.** Missing Baryons and the Large-Scale Structure of the Universe. Tartu, 2023, 121 p.
25. **Moorits Mihkel Muru.** Modeling the cosmic web with the Bisous method. Tartu, 2023, 98 p.